TUDelft

Delft University of Technology

Exploring the quality factor limits of room temperature nanomechanical resonators

Cupertino, A.

Important note
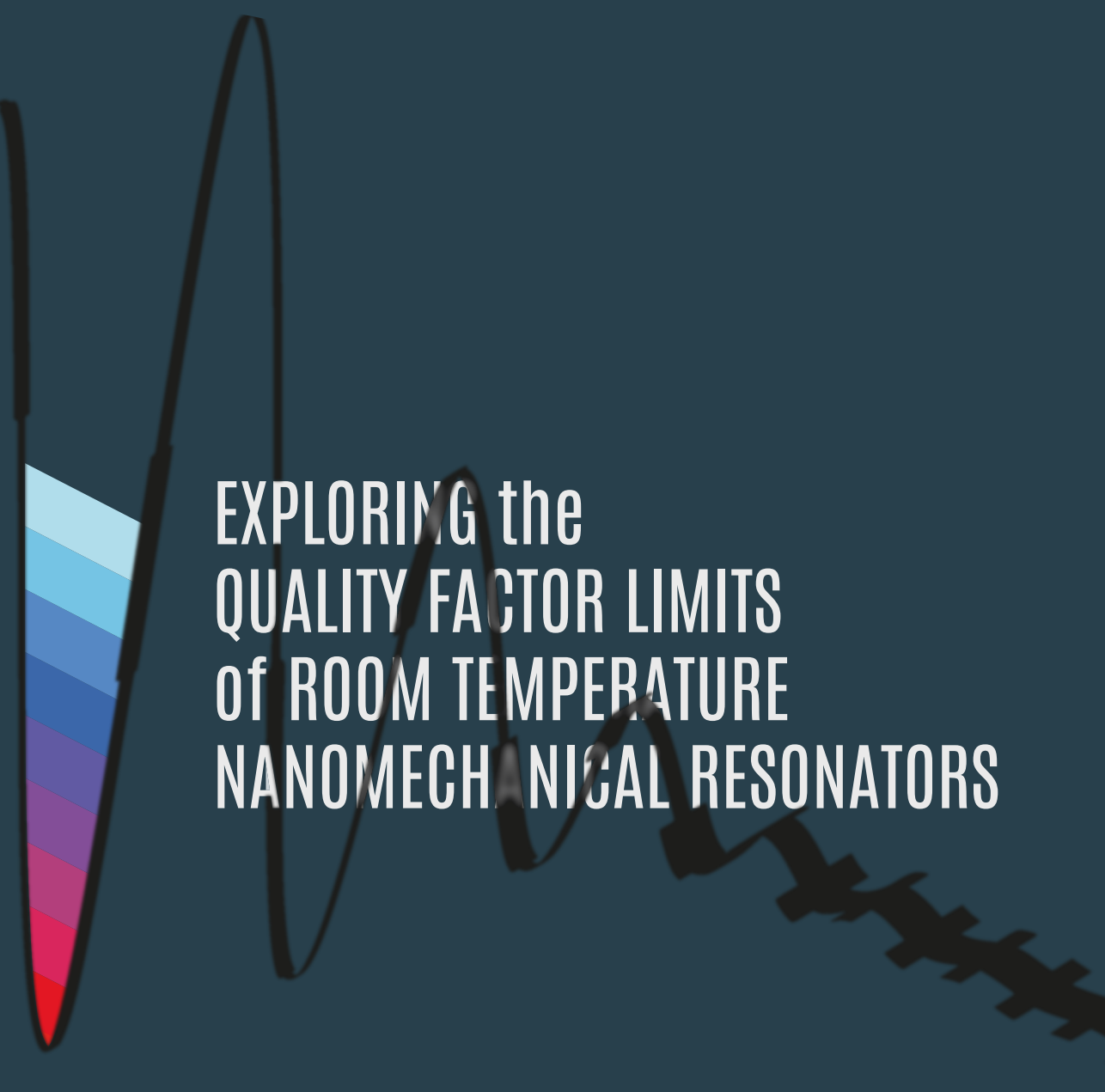To cite this publication, please use the final published version (if applicable).
Please check the document version above.

EXPLORING the QUALITY FACTOR LIMITS of ROOM TEMPERATURE NANOMECHANICAL RESONATORS

ANDREA CUPERTINO

Exploring the quality factor limits of room temperature nanomechanical resonators

Exploring the quality factor limits of room temperature nanomechanical resonators

Dissertation

for the purpose of obtaining the degree of doctor
at Delft University of Technology
by the authority of the Rector Magnificus Prof.dr.ir. T.H.J.J. van der Hagen
Chair of the Board for Doctorates
to be defended publicly on Monday 20 November 2023 at 15:00 o'clock

by

Andrea CUPERTINO

Master of Science in micro et nanotechnologies pour les systemes integres,
Institute Polytechnique de Grenoble, France
born in Putignano, Italy

This dissertation has been approved by the promotors

Composition of the doctoral committee:

Rector Magnificus,	chairperson
Prof. dr. P. G. Steeneken,	Technische Universiteit Delft, promotor
Dr. R. A. Norte,	Technische Universiteit Delft, copromotor

Independent members:

Prof. dr. U. Staufer	Technische Universiteit Delft
Prof. dr. E. Verhagen	Technische Universiteit Eindhoven / AMOLF
Prof. dr. S. Schmid	Technical University of Vienna
Dr. M. A. Bessa	Brown University
Dr. A. Eichler	ETH Zürich

Reserve member:

Prof. dr. G. A. Steele	Technische Universiteit Delft

Contents

Summary

Nanomechanical resonators have become integral to technological advancements and scientific progress in modern society. Not only do they enable exquisite precision in sensing applications, but they also allow for exploring quantum mechanics and the development of quantum technologies. These applications require resonators with high quality factors capable of isolating them from environmental noise, specifically crucial at room temperature.

The focus of this thesis is on investigating the limits of quality factors in nanomechanical resonators operating at room temperature. The study revolves around four main facets, addressing limitations in fabrication techniques, and design strategies, exploring the impact of aspect ratio on quality factor enhancement, and investigating the potential for temperature sensing.

Firstly, we address the limits imposed by current fabrication techniques to realize high aspect ratio resonators, such as stiction and collapse due to interfacial forces like capillary. To overcome these challenges, we develop and characterize an SF_6 plasma etching technique which enables a quick and controllable release of nanomechanical resonators. The high fidelity achieved through this approach allows the use of advanced optimization strategies to design resonators with exceptional quality factors.

In doing so, we tackle the limits of design strategies, which have primarily relied on human intuition until now. By harnessing the power of Bayesian Optimization and in-

spired by nature, we discover a strategy to increase the quality factor at low order mode via a torsional soft-clamping mechanism. The experimental validation of the resulting spiderweb resonators confirms quality factors surpassing 1 billion at room temperature in the kHz frequency range. Notably, these resonators contain no features smaller than 1 μm, ensuring a fast and cost-effective fabrication.

Expanding on these findings, the thesis explores the limits of aspect ratio in quality factor enhancement. By bridging nanomechanics and macromechanics, we create nanomechanical resonators with centimeter-scale lateral sizes. Utilizing multi-fidelity Bayesian Optimization alongside stiction-free fabrication techniques, our strategy allows to reduce the computational cost and to suspend the fragile structures with a fabrication yield approaching 100%, leading to a quality factor above 6 billion.

Finally, the thesis investigates the potential of high quality factor nanomechanical resonators for temperature sensing. We develop a primary noise thermometer to detect temperature across a wide range. The elevated quality factor enables the detection of the effect of the Brownian motion on the resonator's motion. However, it also poses limitations on the measurement scheme due to the narrow linewidth of the resonators.

Combining all these aspects, this thesis explores and pushes the boundaries of quality factors in nanomechanical resonators at room temperature. It presents novel fabrication techniques, advanced design strategies, and sensing capabilities of high quality factor resonators. The findings offer valuable insights and open up new possibilities for applications in precision sensing, quantum mechanics, and beyond.

Samenvatting

Nanomechanische resonatoren zijn een integraal onderdeel geworden van technologische vooruitgang en wetenschappelijke vooruitgang in de moderne maatschappij. Ze maken niet alleen een verfijnde precisie in detectietoepassingen mogelijk, maar ze maken ook de verkenning van kwantummechanica en de ontwikkeling van kwantumtechnologieën mogelijk. Voor de meeste van deze toepassingen is het noodzakelijk dat de resonatoren een kwaliteitsfactor bezitten die hoog genoeg is om ze te isoleren van omgevingsruis, wat vooral cruciaal is bij kamertemperatuur. Dit proefschrift gaat in op de grenzen van de kwaliteitsfactor van nanomechanische resonatoren die bij kamertemperatuur werken. Het onderzoek draait om vier belangrijke facetten: het aanpakken van beperkingen in fabricagetechnieken, het verfijnen van ontwerpstrategieën, het onderzoeken van de invloed van de hoogte-breedteverhouding op de verbetering van de kwaliteitsfactor en het onderzoeken van het potentieel voor temperatuursensoren.

Ten eerste pakken we de beperkingen aan die de huidige fabricagetechnieken opleggen, zoals stiction en collaps als gevolg van interfaciale krachten zoals capillairen, om resonatoren met een hoge aspectratio te realiseren. Om deze uitdagingen te overwinnen, ontwikkelen en karakteriseren we een SF_6 plasma-ets techniek die een snelle en controleerbare vrijgave van nanomechanische resonatoren mogelijk maakt. De hoge getrouwheid die bereikt wordt met deze aanpak maakt het mogelijk om geavanceerde optimalisatiestrategieën te gebruiken om resonatoren met uitzonderlijke kwaliteitsfactoren

te ontwerpen.

Hiermee pakken we de beperkingen van ontwerpstrategieën aan, die tot nu toe voornamelijk op menselijke intuïtie leunden. Door gebruik te maken van de kracht van Bayesiaanse optimalisatie en geïnspireerd door de natuur, ontdekken we een strategie om de kwaliteitsfactor bij een lage orde modus te verhogen via een torsie-mechanisme met zachte klemming. De experimentele validatie van de resulterende spinnenwebresonatoren bevestigt kwaliteitsfactoren van meer dan 1 miljard bij kamertemperatuur in het kHz-frequentiebereik. Met name bevatten deze resonatoren geen elementen kleiner dan 1 μm, waardoor een snelle en kosteneffectieve fabricage mogelijk is.

Voortbordurend op deze bevindingen verkent dit proefschrift de grenzen van de hoogte-breedteverhouding bij het verbeteren van de kwaliteitsfactor. Door een brug te slaan tussen nanomechanica en macromechanica, creëren we nanomechanische resonatoren met zijdelingse afmetingen op centimeterschaal. Door gebruik te maken van multi-fidelity Bayesiaanse optimalisatie naast stictionvrije fabricagetechnieken, maakt onze strategie het mogelijk om de rekenkosten te verlagen en de fragiele structuren op te hangen met een fabricageopbrengst die de 100

Tot slot onderzoekt dit proefschrift het potentieel van nanomechanische resonatoren met een hoge kwaliteitsfactor voor temperatuurdetectie. We ontwikkelen een primaire ruisthermometer om temperatuur over een groot bereik te detecteren. De verhoogde kwaliteitsfactor maakt het mogelijk om het effect van de Brownse beweging op de beweging van de resonator te detecteren. Het levert echter ook beperkingen op voor het meetschema vanwege de smalle lijnbreedte van de resonatoren.

Door al deze aspecten te combineren worden in dit proefschrift de grenzen van kwaliteitsfactoren in nanomechanische resonatoren bij kamertemperatuur verkend en verlegd. Het presenteert nieuwe fabricagetechnieken, geavanceerde ontwerpstrategieën en detectiemogelijkheden van resonatoren met een hoge kwaliteitsfactor. De bevindingen bieden waardevolle inzichten en openen nieuwe mogelijkheden voor toepassingen in precisiedetectie, kwantummechanica en daarbuiten.

1

Introduction

1

1.1. Resonating through history

Mechanical resonators have proven since long ago to be some of the most ubiquitous physical systems known. They represent an intuitive, perhaps the most intuitive, realization of a common phenomenon in nature, namely the harmonic oscillator. They have hence been the object of scientific interest throughout history starting from the seminal studies conducted by Galileo, Hooke, and Newton in the 1600s. Their applications in science date back to the 17th century when Huygens built the first pendulum clock[1]. Soon after Coulomb's torsion balance enabled to quantify the amount of force between two electric charges, discovering what is known today as Coulomb's law[2], and the famous Cavendish experiment allowed to define the gravitational constant[3]. Another notable example is the Foucault pendulum used in 1851 to determine the Earth's rotation, ending a quest that lasted two centuries[4,5].

If all those examples are the size of a human being, today's technological advancement has enabled the extension of modern mechanical resonators over kilometers or reduced their size to the dimension of a few atoms. At the large scale, they are at the forefront of a wide range of applications, ranging from detecting gravitational waves[6] to probing quantum mechanics phenomena[7] and its interplay with gravity[8]. The most prominent example is the kilogram-scale mirrors in gravitational wave detection[9], which allowed in 2015 the first observation of gravitational waves, predicted by Albert Einstein a hundred years ago.

At the other end of the length scale, William McLellan's tiny motor[10], 3.81 mm wide, invented in the late 1950s, following the visionary talk by Richard Feynman "There's Plenty of Room at the Bottom", is regarded by many as the first example at the small scale. Remarkably, the device was created entirely by hand with a microscope and tweezers. The rise of the semiconductor industry in the following decades soon enabled the fabrication of those devices with conventional microfabrication techniques[11], bringing mechanical resonators into the nano-world. This opened new horizons given the high degrees of control over the shape combined with the high level of modularity, scalability, and integration. Since the breakthrough of scanning tunneling microscopy (STM) in the '80s and atomic force microscopy (AFM) a few years later, mechanical resonators with micrometers or nanometers sizes have been used to sense different physical quantities such as force[12], mass[13], acceleration[14] and temperature[15] with unprecedented resolution. Such small resonators are nowadays conventionally employed to process high-frequency signals in consumer electronics (mobile phones, laptops, and television)[16], to deploy airbags in the automotive sector and to modulate light beams in projection displays[17]. The current field has matured to the point where mass production of mechanical resonators that are hundreds of times smaller than McLellan's original is routinely achieved.

It is thus difficult to overstate the importance of nanomechanical resonators[†]. in the modern world. Their working principle consists of a mechanical element that moves in response to an applied force. They are therefore ideal candidates to develop highly sensitive sensors and detectors, as long as the desired quantity to sense can generate a mechanical force. As such, they have enabled dramatic progress like measuring the mass of

---

[†]Note that for simplicity the term nanomechanical resonators in this thesis is used to indicate devices with both micrometers and nanometers feature sizes, including devices conventionally termed micromechanical resonators.

single-protein[18], the motion of bacteria[19] and the magnetic force of single spins[20]. Moreover, if the desired quantity to sense can be directly extracted by a known physical law or equation of state, the sensor does not need any external calibration with respect to a reference. The class of sensors thus created are called "primary sensors" and provide absolute accuracy, with critical applications ranging from measuring physical constants to defining measurement scales and obtaining measurements in harsh environments where other sensors cannot be employed. Specifically relevant for nanomechanical resonators are temperature and pressure primary sensors. As heat and pressure are transmitted by quantized phonons and gas particles, counting the individual collisions gives access to temperature and pressure sensing at its fundamental limit[21]. Lastly, if nanomechanical resonators are shielded by the ambient noise, their quantum nature can be probed and hence lead to the development of quantum sensors. New and exciting applications are then emerging in both classical and quantum sensing to develop sensors with ultra-high sensitivity or to measure new physical quantities yet unexplored with mechanical resonators.

1.2. Higher performance under stress

Mechanical resonators owe their widespread use to their ability to dissipate very little energy, in other words, their low mechanical dissipation quantified by the quality factor (Q), combined with their capacity to couple to the surrounding environment. Among the available platforms to create mechanical resonators with high Q, strained materials with high aspect ratios are the most commonly used. Specifically silicon nitride (Si_3N_4) under high tensile stress stands as the material with the lowest level of dissipation at room temperature. It has hence been extensively used to develop on-chip mechanical resonators operating at room temperature in the form of suspended membranes[22] and suspended strings[23]. By now it is understood that the observed low level of energy dissipated per cycle originates from the high tensile stress, which "dilutes" the elastic energy representing the intrinsic energy dissipated in the material. It is important to note that the increase in the Q factor caused by the high tensile stress comes at the expense of operating at a higher resonance frequency (f). Depending on the dominant loss mechanics, the resulting damping rate $\propto f/Q$ might decrease proportional to the tensile stress or stay constant.

The feature was originally discovered in the macroscopic mechanical resonators used for gravitational wave observatories[24,25] and soon after applied at the nanoscale[26]. The exceptionally low dissipation results in a quality factor exceeding 1 million at room temperature, a remarkable value for mechanical resonators especially at the nanoscale. This allowed landmark demonstrations of quantum effects at moderate cryogenic temperatures[27,28] as well as development of sensors with ultra-high sensitivity[14,29]. However the quest for quantum technology operating at room temperature and the need to achieve higher sensitivity motivated studies to further improve the quality factor.

To understand how to do so, it is important to take a step back and analyze the different sources of mechanical losses in mechanical resonators. The quality factor is defined as the ratio of the energy stored in the system over the energy dissipated for each cycle ($Q = 2\pi \frac{E}{\Delta E}$). The energy can be dissipated by intrinsic and extrinsic means. The resulting quality factor, inversely proportional to the mechanical dissipation, is then given by the following equation[30]:

$$\frac{1}{Q_{tot}} = \frac{1}{Q_{extr}} + \frac{1}{Q_{intr}}$$
(1.1)

Extrinsic contributions arise from the interaction between the mechanical resonators and the surrounding environment, while intrinsic contributions refer to the energy lost inside the material due to microscopic phenomena. In the next section, we will analyze the main mechanism causing both terms and how to mitigate them.

1.3. Extrinsic loss

Extrinsic contributions (Q_{extr}) are caused by the interaction of mechanical resonators with the surrounding environment. Gas damping and radiation losses are the most relevant for the nanomechanical resonators considered in this thesis. The first originates from the interaction between the moving surface of the resonators with the gas molecules around them and it is often the dominant factor at ambient conditions, whereas the second refers to the radiation of vibrational energy leaking through the anchors to the substrates.

Gas damping usually dominates because mechanical resonators – specifically nanomechanical resonators – possess a large surface area compared to their volume which increases the area interacting with the gas molecules. Assuming that the shape and size of the resonators are fixed, an effective way to reduce gas damping is to lower the amount of gas molecules, or in other words the pressure of the gas around it. For large levels of pressure, the gas can be considered a continuum and the energy is dissipated by the viscous flow of the gas, the loss mechanism is then called viscous damping[31]. For low levels of pressure, the gas enters the ballistic regime where the sparse molecules do not interact among themselves, and the dissipation is caused by the impact between the resonators with single molecules[32]. Once the pressure decreases below a critical value, the amount of gas molecules surrounding the resonators becomes so little that the energy lost due to the impact between the spare molecules and resonators can be considered negligible[33]. The pressure level at which this happens depends on the gas composition, specifically the mean free path length, and the resonators dimension via a parameter called Knudsen number (K_n)[34] and it usually in the range between 10^{-3} and 10^{-9} mbar for resonators operating at kHz or MHz. For this reason, mechanical resonators usually need to operate at low pressure inside either a sealed box or vacuum chamber to avoid any contribution from gas damping.

The next most relevant damping mechanism contributing to extrinsic loss is radiation loss, referring to the radiation of vibrational energy leaking to the anchors[35]. The magnitude of it can be highly dependent on the geometries of the resonators and the supporting structures and it is therefore difficult to address it in general terms. Nevertheless, radiation losses have been the object of many investigations[35–37] and it is instructive to review some of the main approaches to mitigate them. Chip mounting conditions have – perhaps unsurprisingly – a large effect on this type of loss. In this context, the term 'chip' refers to the combination of silicon nitride resonators and the underlying substrate, typically made from silicon. The chip is mounted on a holder, whose purpose is to provide support during measurements.

Minimizing the coupling between the chip and the holder directly affects the quality factor. These two parts need in fact to be in contact, and various methods can be employed

such as gluing or mechanical clamping. However, both techniques can introduce a channel for vibrational energy to leak into the environment, thereby reducing the quality factor. On the contrary, clamping the chip to the holder solely via gravity has been proven as an effective way for isolating the chip and reducing radiation losses[38]. Furthermore, the coupling within the chip itself, specifically between the resonator and the substrate, has been found to significantly impact the quality factor. In particular, substrate thickness has a sizeable effect due to the mechanical mismatch between the substrate and the resonators, with thick substrates exceeding 1 mm reported to significantly reduce radiation losses[29]. Lastly, the position of the resonators with respect to the substrate together with the shape of both have been reported to influence the quality factor due to the overlap in frequency between substrate modes and resonator modes[39]. The effect can be mitigated by a careful design of the substrate aimed at avoiding any overlap.

All those methods intend to mitigate radiation losses by changing the shape, the thickness, and the clamping mechanics of the substrate. Despite their effectiveness, they are not always applicable or pose some limitations from the application point of view. An alternative and complementary way to tackle this issue, recently proposed, consists of focusing on the design of the resonators itself rather than the substrate[40]. Suppressing the vibration of the resonators at the anchors strongly diminishes the amount of energy that can radiate to the substrate. This reduces radiation losses without the need to engineer the substrate or its clamping mechanics. Once this is achieved, extrinsic contribution stops being the dominant factor and intrinsic contribution starts to dominate the mechanical dissipation of the resonators.

1.4. Intrinsic loss

Intrinsic contribution Q_{intr} refers to the energy lost inside the material due to microscopic phenomena. The mechanisms behind it can be clustered into two categories: fundamental loss and friction loss[30]. The former represents the ultimate limit of the material and originates from not-reversible heat in the resonators during vibration[41–43] as such they will always be present unless a different material is considered. The latter is caused by the friction on the bulk of the material or the surface due to material imperfections[44,45]. Thin silicon nitride resonators have a large surface-to-volume ratio and as such most of the friction happens on the surface[46], which dominates over bulk losses.

Systematic investigations of silicon nitride resonators allowed understanding the origin of friction losses contributions[22,26,47,48]. It was discovered that in the high-stress limit, most of the energy gets dissipated at the clamping points, where the resonator is attached to the supporting substrate[47,49,50]. Those resonators are supported by a substrate, typically silicon, which keeps a high level of tensile stress. The resonators are generally in the form of thin membranes or strings, though more complex geometries are possible. During vibration, the curvature at those clamping points becomes particularly sharp such that most of the elastic energy is dissipated. Contrarily, the curvature towards the center of the resonator follows a gentler slope and most of the elastic energy remains in the system. Then, a lot of attention went into developing strategies to overcome those limitations to reduce intrinsic losses.

A first approach envisaged to reduce the size of the clamping area to increase the value of tensile stress at the clamping points due to stress redistribution[29,51]. Following dissi-

pation dilution, higher stress translates into more intrinsic dissipation being "diluted" and hence locally increasing the quality factor of the material at the clamping point, exactly where most of the energy is dissipated. This idea has been experimentally tested for both 1D structures[51] by tapering the width of a string near the clamping points and for 2D structures[29,52] in trampoline configurations where a central pad is anchored to the substrate by four thin highly tensioned strings. The resulting quality factor was then improved by two orders of magnitude compared to a simple membrane or a string, reaching values up to 100 million. However, this approach does not suppress the vibration of the resonator at the anchors, which is a critical feature in limiting radiation losses. As such, the expected quality factor enhancement occurs only if thick substrates are employed and the chip is clamped by gravity alone, limiting their applications. Moreover the obtained quality factors, despite being extremely high, are still far away from the ultimate limit analytically predicted[50] because the sharp curvature at the clamping points is still present.

In what might appear in hindsight a natural following step, the next proposed approach consisted of suppressing the curvature of the resonator at the clamping points rather than increasing the level of tensile stress in there. This has a twofold advantage: on the one hand, it localizes the vibration far away from the anchors reducing the probability that the resonator interacts with the substrate, basically suppressing radiation losses and hence extrinsic losses. On the other hand, it drastically increases dissipation dilution by reducing the sharp curvature at the clamping points, highly reducing the intrinsic losses. This can be achieved by techniques commonly known as "soft clamping"[40], able to tackle both intrinsic and extrinsic contributions. The name originates from the idea of anchoring the resonator to the substrate via a "soft" anchoring region instead of the usual rigid clamp. This soft clamping region allows the resonator modes to evanescently penetrate, reducing the mode's curvature. The first implementation of this approach was experimentally demonstrated in 2017 via a phononic crystal[40].

A phononic crystal is a period variation of the material's acoustic properties (elasticity or density). As a period variation of atoms in real crystals creates an electronic bandgap, or a period variation of refractive index in a photonic crystal creates an optical bandgap, the period variation of material's acoustic properties opens a phononic bandgap where no acoustic waves can exist. In practice, this is realized by patterning the resonator's surface, either by removing specific areas with holes or by adding structures on top of the resonators with pillars. The periodicity is then interrupted by a defect placed in the center of the phononic crystal, whose vibrational mode sits inside the bandgap of the surrounding phononic crystal. This allows the spatial localization of this vibrational mode inside the defect area since it cannot travel into the surrounding phononic crystal. At the same time, the confinement does not happen abruptly because the comparable stiffness between the phononic crystal and the defect region enables a gradual decay of the vibrational mode into the "soft" anchoring region (i.e. the phononic crystal). It follows that once the vibrational mode reaches the clamping point (where the phononic crystal is anchored to the substrate) its amplitude has become negligible, hence drastically enhancing the degree of dilution.

In additional steps, this strategy was combined with stress engineering to reach the material dissipation limit[53], resulting in nanomechanical resonators with a quality factor approaching one billion at room temperature. Despite its effectiveness, these techniques apply only to high-order modes, imposing limitations on the operational frequency. Fur-

thermore, the devices require an extreme aspect ratio (length/thickness $> 10^5$) to take full advantage of dissipation dilution, which makes them challenging to fabricate reliably with the current processes.

1.5. Challenges

Therefore, although the extraordinary quality factor currently achievable, there still exist fundamental and technological challenges for utilizing nanomechanical resonators at their full potential and more importantly for being able to exploit their sensing capabilities. On the one hand, current fabrication processes, and specifically the wet release steps, are prone to cause stiction due to interfacial forces as capillary[54], highly limiting the designs that can be fabricated in a homogeneous and controllable way. This is particularly relevant if one wants to investigate the ultimate limit of dissipation dilution with devices with extreme high aspect ratio and centime-scale length. To overcome those limitations, dry release can be employed, where the silicon substrate is isotropically removed by plasma etching[55]. However, those processes suffer from poor selectivity between the silicon substrate and the thin silicon nitride layer. This issue is a core aspect of this thesis and it is addressed in detail in **chapter 2**. Based on those findings, all the devices presented in this thesis in the following chapters are fabricated by the developed stiction-free dry release. Building on it, **chapter 4** discusses the required variations to apply it to devices with extreme high aspect ratio and centime-scale length and its advantages.

On the other hand, we lack design strategies to discover soft clamped resonators operating at low-order modes and low frequency while maintaining a high enough Q factor, advantageous for both high-precision sensing and fundamental physics applications. More in general, the discovery of new resonators has been driven thus far by trial-and-error following human intuition. Despite the impressive progress achieved in maximizing the Q factor, this approach is limited by the long fabrication and testing time of each design, which restricts the number of iterations achievable within a reasonable time and it doesn't consider unexplored and counterintuitive designs, which might result in better performances. Advanced techniques such as optimization guided by machine learning offer a promising alternative to reduce the design time and discover new paradigms. However, their practical utility is constrained by the high computation cost of each simulation resulting in a scarcity of data with high accuracy. The latter is a central aspect of this thesis, with **chapter 3** and **chapter 4** addressing it.

Lastly, the limitations and the advantages of the developed resonators for specific sensing applications need to be investigated. To this end we target primary temperature sensing, critical for a wide range of processes, from consumer electronics to space instrumentation. The range of currently available thermometers cannot meet the growing need to make temperature measurements at mesoscopic scales. At the same time, the redefinition of the kelvin in 2018 (i.e. the primary unit of temperature) now based on a fixed value of the Boltzmann constant requires a new thermodynamic temperature measurements scheme. Nanomechanical resonators with low mechanical dissipation can address this challenge as their motion is directly influenced by the temperature of the surrounding gas due to its Brownian motion. The power spectral density experienced by the resonator scales linearly with the temperature and gives direct access to the Boltzmann constant and the temperature of the gas without any calibration, as discussed in the last chapter.

1.6. Thesis outline

This thesis aims to address those challenges by developing novel design and fabrication strategies to create nanomechanical resonators with the lowest level of mechanical dissipation (i.e. high quality factor) at room temperature. The acquired knowledge is then used to develop self-calibrated temperature sensors. By doing this, this thesis seeks to advance the state-of-the-art for high aspect ratio nanomechanical resonators with low dissipation.

It consists of four parts. **Chapter 2** is dedicated to an in-depth description of the fabrication process used for all the mechanical resonators discussed in this thesis. Most of the modern suspended structures rely on wet release, known to cause stiction in large surface-area-to-volume ratios due to interfacial forces like capillary, highly limiting the designs which can be fabricated in a homogeneous and controllable way. On the contrary, the method here proposed is based on a stiction-free dry release, which results in a quick and controllable way to suspend high aspect ratio nanomechanical resonators. Moreover, it is not constrained to the crystal orientation of the substrate underneath, and it allows fabricating design of any geometry. The method has been employed to fabricate devices beyond this thesis due to its versatility. The chapter ends by highlighting the main advantages and future recommendations.

Chapter 3 introduces a novel approach to designing nanomechanical resonators operating at low order modes and compact size. The approach aims to overcome limitations faced by current strategies, mostly driven by human intuition and trial-and-error. Inspired by nature and guided by machine learning, a spiderweb nanomechanical resonator is developed. The resulting vibrational modes are isolated from ambient thermal environments via a novel "torsional soft-clamping" mechanism discovered by the data-driven optimization algorithm. The resonators are then fabricated, experimentally confirming quality factors above 1 billion at room temperature with a compact design, making it significantly easier and cheaper to manufacture at large scales.

Chapter 4 outlines the vision and realization of the first nanomechanical resonators with extreme aspect ratio. The resulting devices extend for centimeters in length, maintaining tens of tens of nanometers, which results in the high computational cost of the design process and fabrication limitations. The proposed approach takes advantage of machine learning to reduce the computational cost. A more robust striction-free dry release allows the fabrication of the optimized design with high accuracy, experimentally showing a quality factor approaching 10 billion at room temperature.

Chapter 5 focuses on applications, specifically the development of a self-calibrated mechanical thermometer to meet the challenges posed by measuring temperature at mesoscopic scales. The measurement protocol results in a primary measurements technique, based on detecting the motion of the resonator by the Brownian motion. The chapter centers around the main advantages of high quality factor nanomechanical resonators for the envisioned applications as well as some technological limitations posed by the current detection scheme.

Finally, the last chapter includes an outlook for future direction and a summary of the findings in this thesis.

References

1. Huygens, C. & Blackwell, R. J. *Christiaan Huygens' the Pendulum Clock, or, Geometrical Demonstrations Concerning the Motion of Pendula as Applied to Clocks* (Iowa State University Press, Ames, 1986) (cit. on p. 2).

2. Coulomb, C. A. *Memoires sur l'electricite et la magnetisme* (Societe francaise de physique, 1785) (cit. on p. 2).

3. Cavendish, H. XXI. Experiments to Determine the Density of the Earth. *Philosophical Transactions of the Royal Society of London* **88,** 469–526 (1789) (cit. on p. 2).

4. Foucault, L. Démonstration physique du mouvement de rotation de la terre au moyen du pendule. *Comptes rendus hebdomadaires des séances de l'Académie des sciences* **32,** 135–138 (1851) (cit. on p. 2).

5. Sommeria, J. Foucault and the Rotation of the Earth. *Comptes Rendus Physique* **18,** 520–525 (2017) (cit. on p. 2).

6. Abramovici, A., Althouse, W. E., Drever, R. W. P., Gürsel, Y., Kawamura, S., Raab, F. J., Shoemaker, D., Sievers, L., Spero, R. E., Thorne, K. S., Vogt, R. E., Weiss, R., Whitcomb, S. E. & Zucker, M. E. LIGO: The Laser Interferometer Gravitational-Wave Observatory. *Science* **256,** 325–333 (1992) (cit. on p. 2).

7. Whittle, C. *et al.* Approaching the Motional Ground State of a 10-Kg Object. *Science* **372,** 1333–1336 (2021) (cit. on p. 2).

8. Matsumoto, N., Cataño-Lopez, S. B., Sugawara, M., Suzuki, S., Abe, N., Komori, K., Michimura, Y., Aso, Y. & Edamatsu, K. Demonstration of Displacement Sensing of a mg-Scale Pendulum for mm- and mg-Scale Gravity Measurements. *Physical Review Letters* **122,** 071101 (2019) (cit. on p. 2).

9. Cumming, A. V., Bell, A. S., Barsotti, L., Barton, M. A., Cagnoli, G., Cook, D., Cunningham, L., Evans, M., Hammond, G. D., Harry, G. M., Heptonstall, A., Hough, J., Jones, R., Kumar, R., Mittleman, R., Robertson, N. A., Rowan, S., Shapiro, B., Strain, K. A., Tokmakov, K., Torrie, C. & van Veggel, A. A. Design and Development of the Advanced LIGO Monolithic Fused Silica Suspension. *Classical and Quantum Gravity* **29,** 035003 (2012) (cit. on p. 2).

10. Roukes, M. Nanoelectromechanical Systems Face the Future. *Physics World* **14,** 25–32 (2001) (cit. on p. 2).

11. Ikumapayi, O., Akinlabi, E., Adeoye, A. & Fatoba, S. Microfabrication and Nanotechnology in Manufacturing System – An Overview. *Materials Today: Proceedings* **44,** 1154–1162 (2021) (cit. on p. 2).

12. Eichler, A. Ultra-High-Q Nanomechanical Resonators for Force Sensing. *Materials for Quantum Technology* **2,** 043001 (2022) (cit. on p. 2).

13. Chaste, J., Eichler, A., Moser, J., Ceballos, G., Rurali, R. & Bachtold, A. A Nanomechanical Mass Sensor with Yoctogram Resolution. *Nature Nanotechnology* **7,** 301–304 (2012) (cit. on p. 2).

14. Krause, A. G., Winger, M., Blasius, T. D., Lin, Q. & Painter, O. A High-Resolution Microchip Optomechanical Accelerometer. *Nature Photonics* **6,** 768–772 (2012) (cit. on pp. 2, 3).

15. Purdy, T. P., Grutter, K. E., Srinivasan, K. & Taylor, J. M. Quantum Correlations from a Room-Temperature Optomechanical Cavity. *Science* **356,** 1265–1268 (2017) (cit. on p. 2).

16. Safavi-Naeini, A. H. *Quantum Optomechanics with Silicon Nanostructures.* PhD thesis (California Institute of Technology, 2013) (cit. on p. 2).

17. Craighead, H. G. Nanoelectromechanical Systems. *Science* **290,** 1532–1535 (2000) (cit. on p. 2).

18. Hanay, M. S., Kelber, S., Naik, A. K., Chi, D., Hentz, S., Bullard, E. C., Colinet, E., Duraffourg, L. & Roukes, M. L. Single-Protein Nanomechanical Mass Spectrometry in Real Time. *Nature Nanotechnology* **7,** 602–608 (2012) (cit. on p. 3).

19. Rosón, I. E., Japaridze, A., Steeneken, P. G., Dekker, C. & Alijani, F. Probing Nanomotion of Single Bacteria with Graphene Drums. *Nature Nanotechnology* **17,** 637–642 (2022) (cit. on p. 3).

20. Rugar, D., Budakian, R., Mamin, H. J. & Chui, B. W. Single Spin Detection by Magnetic Resonance Force Microscopy. *Nature* **430,** 329–332 (2004) (cit. on p. 3).

21. Barker, D. S., Carney, D., LeBrun, T. W., Moore, D. C. & Taylor, J. M. *Collision-Resolved Pressure Sensing.* 2023 (cit. on p. 3).

22. Yu, P.-L., Purdy, T. P. & Regal, C. A. Control of Material Damping in High- Q Membrane Microresonators. *Physical Review Letters* **108,** 083603 (2012) (cit. on pp. 3, 5).

23. Verbridge, S. S., Parpia, J. M., Reichenbach, R. B., Bellan, L. M. & Craighead, H. G. High Quality Factor Resonance at Room Temperature with Nanostrings under High Tensile Stress. *Journal of Applied Physics* **99,** 124304 (2006) (cit. on p. 3).

24. González, G. I. & Saulson, P. R. Brownian Motion of a Mass Suspended by an Anelastic Wire. *The Journal of the Acoustical Society of America* **96,** 207–212 (1994) (cit. on p. 3).

25. Cagnoli, G., Hough, J., DeBra, D., Fejer, M., Gustafson, E., Rowan, S. & Mitrofanov, V. Damping Dilution Factor for a Pendulum in an Interferometric Gravitational Waves Detector. *Physics Letters A* **272,** 39–45 (2000) (cit. on p. 3).

26. Unterreithmeier, Q. P., Faust, T. & Kotthaus, J. P. Damping of Nanomechanical Resonators. *Physical Review Letters* **105,** 027205 (2010) (cit. on pp. 3, 5).

27. Purdy, T. P., Peterson, R. W. & Regal, C. A. Observation of Radiation Pressure Shot Noise on a Macroscopic Object. *Science* **339,** 801–804 (2013) (cit. on p. 3).

28. Wilson, D. J., Sudhir, V., Piro, N., Schilling, R., Ghadimi, A. & Kippenberg, T. J. Measurement-Based Control of a Mechanical Oscillator at Its Thermal Decoherence Rate. *Nature* **524,** 325–329 (2015) (cit. on p. 3).

29. Norte, R. A., Moura, J. P. & Gröblacher, S. Mechanical Resonators for Quantum Optomechanics Experiments at Room Temperature. *Phys. Rev. Lett.* **116,** 147202 (2016) (cit. on pp. 3, 5, 6).

30. Schmid, S., Villanueva, L. G. & Roukes, M. L. *Fundamentals of Nanomechanical Resonators* (Springer International Publishing, Cham, 2016) (cit. on pp. 3, 5).

31. Bianco, S., Cocuzza, M., Ferrero, S., Giuri, E., Piacenza, G., Pirri, C. F., Ricci, A., Scaltrito, L., Bich, D., Merialdo, A., Schina, P. & Correale, R. Silicon resonant microcantilevers for absolute pressure measurement. *Journal of Vacuum Science & Technology B* **24,** 1803–1809 (2006) (cit. on p. 4).

32. Bao, M., Yang, H., Yin, H. & Sun, Y. Energy Transfer Model for Squeeze-Film Air Damping in Low Vacuum. *Journal of Micromechanics and Microengineering* **12,** 341–346 (2002) (cit. on p. 4).

33. Verbridge, S. S., Ilic, R., Craighead, H. G. & Parpia, J. M. Size and Frequency Dependent Gas Damping of Nanomechanical Resonators. *Applied Physics Letters* **93,** 013101 (2008) (cit. on p. 4).

34. Bhiladvala, R. B. & Wang, Z. J. Effect of Fluids on the Q Factor and Resonance Frequency of Oscillating Micrometer and Nanometer Scale Beams. *Physical Review E* **69,** 036307 (2004) (cit. on p. 4).

35. Wilson-Rae, I. Intrinsic Dissipation in Nanomechanical Resonators Due to Phonon Tunneling. *Physical Review B* **77,** 245418 (2008) (cit. on p. 4).

36. Wilson-Rae, I., Barton, R. A., Verbridge, S. S., Southworth, D. R., Ilic, B., Craighead, H. G. & Parpia, J. M. High- Q Nanomechanics via Destructive Interference of Elastic Waves. *Physical Review Letters* **106,** 047205 (2011) (cit. on p. 4).

37. Photiadis, D. M. & Judge, J. A. Attachment Losses of High Q Oscillators. *Applied Physics Letters* **85,** 482–484 (2004) (cit. on p. 4).

38. Wilson, D. J. *Cavity Optomechanics with High-Stress Silicon Nitride Films.* PhD thesis (California Institute of Technology, 2012) (cit. on p. 5).

39. de Jong, M. H. J., ten Wolde, M. A., Cupertino, A., Gröblacher, S., Steeneken, P. G. & Norte, R. A. Mechanical Dissipation by Substrate-Mode Coupling in SiN Resonators. *Applied Physics Letters* **121,** 032201 (2022) (cit. on p. 5).

40. Tsaturyan, Y., Barg, A., Polzik, E. S. & Schliesser, A. Ultracoherent Nanomechanical Resonators via Soft Clamping and Dissipation Dilution. *Nature Nanotechnology* **12,** 776–783 (2017) (cit. on pp. 5, 6).

41. Lifshitz, R. & Roukes, M. L. Thermoelastic Damping in Micro- and Nanomechanical Systems. *Physical Review B* **61,** 5600–5609 (2000) (cit. on p. 5).

42. Zwickl, B. M., Shanks, W. E., Jayich, A. M., Yang, C., Bleszynski Jayich, A. C., Thompson, J. D. & Harris, J. G. E. High Quality Mechanical and Optical Properties of Commercial Silicon Nitride Membranes. *Applied Physics Letters* **92,** 103125 (2008) (cit. on p. 5).

43. Rodriguez, J., Chandorkar, S. A., Watson, C. A., Glaze, G. M., Ahn, C. H., Ng, E. J., Yang, Y. & Kenny, T. W. Direct Detection of Akhiezer Damping in a Silicon MEMS Resonator. *Scientific Reports* **9,** 1–10 (2019) (cit. on p. 5).

44. Zener, C. Internal Friction in Solids. I. Theory of Internal Friction in Reeds. *Physical Review* **52,** 230–235 (1937) (cit. on p. 5).

45. Zener, C. Internal Friction in Solids II. General Theory of Thermoelastic Internal Friction. *Physical Review* **53,** 90–99 (1938) (cit. on p. 5).

46. Villanueva, L. G. & Schmid, S. Evidence of Surface Loss as Ubiquitous Limiting Damping Mechanism in SiN Micro- and Nanomechanical Resonators. *Physical Review Letters* **113,** 227201 (2014) (cit. on p. 5).

47. Schmid, S., Jensen, K., Nielsen, K. & Boisen, A. Damping Mechanisms in High-Q Micro and Nanomechanical String Resonators. *Physical Review B* **84,** 1–6 (2011) (cit. on p. 5).

48. Chakram, S., Patil, Y. S., Chang, L. & Vengalattore, M. Dissipation in Ultrahigh Quality Factor SiN Membrane Resonators. *Physical Review Letters* **112,** 127201 (2014) (cit. on p. 5).

49. Fedorov, S. A., Engelsen, N. J., Ghadimi, A. H., Bereyhi, M. J., Schilling, R., Wilson, D. J. & Kippenberg, T. J. Generalized Dissipation Dilution in Strained Mechanical Resonators. *Physical Review B* **99,** 054107 (2019) (cit. on p. 5).

50. Sementilli, L., Romero, E. & Bowen, W. P. Nanomechanical Dissipation and Strain Engineering. *Advanced Functional Materials* **32,** 2105247 (2022) (cit. on pp. 5, 6).

51. Bereyhi, M. J., Beccari, A., Fedorov, S. A., Ghadimi, A. H., Schilling, R., Wilson, D. J., Engelsen, N. J. & Kippenberg, T. J. Clamp-Tapering Increases the Quality Factor of Stressed Nanobeams. *Nano Letters* **19,** 2329–2333 (2019) (cit. on pp. 5, 6).

52. Reinhardt, C., Müller, T., Bourassa, A. & Sankey, J. C. Ultralow-Noise SiN Trampoline Resonators for Sensing and Optomechanics. *Physical Review X* **6,** 021001 (2016) (cit. on p. 6).

53. Ghadimi, A. H., Fedorov, S. A., Engelsen, N. J., Bereyhi, M. J., Schilling, R., Wilson, D. J. & Kippenberg, T. J. Elastic Strain Engineering for Ultralow Mechanical Dissipation. *Science* **360,** 764–768 (2018) (cit. on p. 6).

54. Norte, R. A. *Nanofabrication for On-Chip Optical Levitation, Atom-Trapping, and Superconducting Quantum Circuits.* PhD thesis (California Institute of Technology, 2015) (cit. on p. 7).

55. Panduranga, P., Abdou, A., Ren, Z., Pedersen, R. H. & Nezhad, M. P. Isotropic Silicon Etch Characteristics in a Purely Inductively Coupled SF_6 Plasma. *Journal of Vacuum Science & Technology B* **37,** 061206 (2019) (cit. on p. 7).

2

Fabrication of high aspect ratio silicon nitride resonators by stiction-free dry etching

Demand for strained, high aspect ratio nanomechanical resonators is surging driven by their ability to be highly isolated from environmental noise. However, the resulting large areas combined with the high tensile stress pose restrictions on their fabrication. Most of the current fabrication processes rely in fact on a wet etch release, known to cause stiction due to interfacial forces and limited control over the structure's cleanliness.

Here we demonstrate a release technique based on dry etching to address this challenge and investigate its etching characteristics. The process relies on the isotropic etching of the supporting silicon substrate by inductively coupled sulfur hexafluoride plasma at cryogenic temperature. It exhibits a silicon etch rate over $10\,\mu\mathrm{m/min}$ in the in-plane direction, higher than values previously reported for comparable methods. The high etch rate is combined with high selectivity over the silicon nitride resonators, which enables a quick and homogeneous release of the nanomechanical resonators. This allows for fabricating high aspect ratio resonators with high fidelity.

2.1. Introduction

Nanomechanical resonators are powerful instruments for fundamental studies of quantum physics and precision sensing[1,2]. Most modern resonators operating at room temperature are fabricated from stoichiometric silicon nitride (Si_3N_4) given its exceptionally low mechanical dissipation[3−11]. As a result, extremely high quality factors are nowadays routinely obtained. By now it has been demonstrated that the high quality factor arises from the combination of high tensile stress over 1 GPa and high aspect ratios[12−14]. State-of-the-art nanoresonators consist in fact of suspended structures extending for millimeters or longer while maintaining a thickness of nanometers. The resulting large areas and the high tensile stress pose however fundamental limitations on their fabrication. Specifically, the most critical challenge consists of releasing the structures without causing any fractures and hence successfully suspending the nanomechanical resonators.

Current fabrications typically rely on wet etching processes based on potassium hydroxide (KOH) or tetramethylammonium hydroxide (TMAH) to etch the silicon substrate. The high selectivity with respect to Si_3N_4 ensures that the latter stays unaffected, allowing the suspension of the nanomechanical resonators. Liquid etchants are however known to cause stiction in structures with large surface-area-to-volume ratio due to interfacial forces as capillary[15,16]. The structures are then pulled toward the substrate leading to the collapse of the delicate resonators. Stiction can be mitigated by a drying process as critical point dryer (CPD)[17,18], which significantly reduces the occurring forces by drying the structures in a controllable way. Nonetheless, this comes at the cost of increasing the complexity of the entire fabrication flow and reducing the achievable fabrication yield. Once the resonators are dried, additional cleanings are then needed to remove any organic contaminants on the surface, which further impact the fabrication yield[19].

2.1.1. Dry etching release

Dry etching processes, on the contrary, offer a promising alternative to reduce the fabrication steps and circumvent the issues inherent to wet processes[20,21]. The etching is carried out by ions and free radicals generated in a plasma and accelerated toward the structure. Dry etching provides high control over the degree of isotropy by adjusting the plasma settings, and thereby the ratio between physical etching due to ion bombardment and chemical etching due to reactive gas. A combination of high isotropy and high etch rate results in a fast undercut of the supporting substrate, leading to a quick and controllable way to suspend Si_3N_4 (figure 2.1). Among the available plasma etchings, fluorine-based gases are the ideal candidates to develop stiction-free dry release processes[22,23].

Fluorine-based gases offer an established way to etch Si[24]. By now it is understood that an ICP source allows dissociation of those gases generating reactive fluorine neutrals (F)[25,26]. The latter then react with the silicon surface to form compound as SiF_2, SiF_3, SiF_4, chemically etching Si[27]. Among the possible fluorine-based gases, sulfur hexafluoride (SF_6) is particularly suited for fast etching in view of its high etch rate[28]. The isotropy of the process can be controlled by the etching parameters, specifically the pressure and the excitation power in an ICP-RIE reactor. In an ICP-RIE the plasma density and the applied voltage to the chip are decoupled and controlled by two generators, the ICP power, and the capacitive RF power. The first allows an increase in the density of radicals in the plasma, thereby chemically etching Si, while the second accelerates the ions in the plasma toward
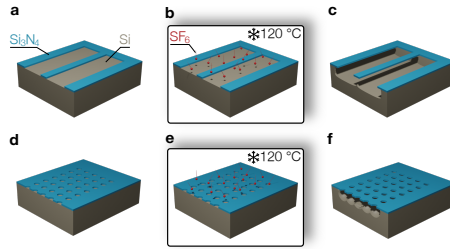
Fig. 2.1 Stiction-free dry release. Schematic of the fabrication steps to suspend high aspect ratio Si_3N_4 strings (**a, b, c**) and membranes (**d, e, f**) by dry etching. **a,** Si_3N_4 string patterned on top of a Si substrate. **b, e,** Isotropic Si etching by fluorine-base dry etching performed at cryogenic temperature in an ICP-RIE reactor. **c,** Suspended Si_3N_4 string. **d,** Si_3N_4 membrane patterned on top of a Si substrate and covered with release holes. **f,** Suspended Si_3N_4 membrane.

the substrate, resulting in the physical etching of Si due to ion bombardment. Removing the capacitive RF excitation enables thus to avoid ion bombardment and hence leads to pure chemical isotropic etching of Si. The pressure in the reactor plays also a crucial role. It has been found that increasing it enhances the concentration of fluorine radicals and reduces the ion bombardment[29].

SF_6 Si etching is routinely used in various microfabrication processes. The most common example is the Bosch Etching, a technique to achieve deep and directional Si etching. It consists of a loop of two short steps, an isotropic etching using SF_6 plasma etching followed by a passivation step with Teflon-like substances to protect the sidewall. The process relies on the high etch rate of SF_6 plasma etching to achieve the desired deep etching, while the passivation step enables the improvement of the directionality and obtain vertical sidewalls[30]. Another notable example is cryogenic deep reactive ion etching (DRIE)[31] where SF_6 gas is combined with oxygen (O_2) gas to directionally etch Si. Similarly to the Bosch Etching, DRIE exploits the high etch rate of Si in SF_6 plasma to obtain deep etching, while O_2 supplies ions used for passivating the sidewall[32]. Crucially, the procedure is carried out at cryogenic temperature (typically -100 to -140 °C) as the passivation layer would not condense at higher temperatures.

Both processes aim to achieve deep and anisotropic etching by harnessing the ability of SF_6 plasma to fast etch Si. On the contrary, suspending high aspect ratio nanomechanical resonators requires a high degree of isotropy. Few data are readily available on how to achieve it[20−23] with no prior studies investigating the effect of the process temperature. More importantly, the effect of SF_6 etching on Si_3N_4 layer has not been addressed thus far.

To this end, we investigate the etch characteristics of SF_6 plasma for suspending high aspect ratio structures. We first investigate the degree of directionality and the etch rate for silicon for different etching conditions. We then analyze the effects of feature sizes on the etch, critical to fabricating 2D structures. Lastly, we focus our attention on the Si_3N_4 layer and the effect of the etching in terms of surface roughness and etch rate.

2.2. Fabrication methodology

Our fabrication starts with an in-house deposition of stoichiometric Si_3N_4 on 4-inch silicon (Si) wafers by low-pressure chemical vapor deposition (LPCVD). Films deposited by LPCVD generally exhibit superior quality compared to other deposition techniques in terms of uniformity and imperfections, a desirable feature to reduce surface losses in nanomechanical resonators[33]. Moreover, LPCVD can deposit Si_3N_4 with a residual tensile stress over 1 GPa, critical to reach the dissipation limit and hence decrease the mechanical dissipation[12]. The high tensile stress arises from the crystal mismatch between Si_3N_4 and the Si substrate created during cool down because of the difference in thermal expansion. It can thereby be controlled by the deposition temperature and the stoichiometric of the film (e.g. the ratio between silicon and nitride). Our deposition is performed at 800 °C, resulting in an intrinsic tensile stress of 1.08 GPa. The resulting Si_3N_4 film shows a variation in thickness of 1 nm over the entire wafer size, confirming a good uniformity. The film is equally characterized by surface roughness below 1 nm.

To ensure a high quality of the Si_3N_4 film, we clean the 4-inch Si wafers with RCA1 and RCA2 prior to the LPCVD deposition. The steps are standard cleaning procedures for organic and metal contaminants, performed at 80 °C. They consist of a solution of $NH_4OH:H_2O_2:H_2O$ (1:1:5) for RCA1 and $HCl:H_2O_2:H_2O$ (1:1:5) for RCA2. The Si wafers are subsequently dipped into diluted hydrofluoric acid solution (0.4%) to remove surface oxides. The LPCVD is performed immediately after this last step to prevent the growth of oxide on the Si surface.

Next, we dice the wafers in small chips with a disco dicer. During the process, the Si_3N_4 surface is covered with photoresist to avoid any damage. The resist is then removed with a two-stage cleaning process with acetone and isopropyl alcohol (IPA). The first removes the resist, whereas the second cleans the chip from the residues of the acetone avoiding striations. After that, the desired pattern is transferred to the individual chips by electron beam lithography. To do so, we first spin coat a positive tone resist (AR-P 6200) on top of the Si_3N_4 and bake it at 155 °C for 3 min. The resist is exposed and subsequently developed in pentylacetate for 1 min, followed by two consecutive cleaning steps with Methyl isobutyl ketone (MIBK): isopropyl alcohol (IPA) (1:1) and IPA for 1 min each and blow-dried with a nitrogen gun. This enables to create the masking layer, whose shape can be readily transferred into the Si_3N_4.

The pattern is transferred using a plasma etching in an inductively coupled plasma reactive ion etcher (ICP-RIE) at room temperature. The combination of CHF_3 and O_2 gases allow the directional and fast removal of Si_3N_4. After the pattern transfer, the residual resist is removed with dimethylformamide (DMF) followed by a two-stage cleaning process with acetone and IPA. The resist stripping in DMF is performed at 80 °C while using ultrasonication for 15 min. We then employ a piranha solution at 80 °C to remove any organic residues, consisting of a solution of sulfuric acid:hydrogen peroxide (3:1). This is followed by a cleaning step with a diluted hydrofluoric acid solution (1%) to remove surface oxides from the Si_3N_4. The most critical part of the process is then suspending the fragile structures over the substrate without causing any fractures, stiction, or collapse, carried out by a fluorine-based dry etching step.

The Si_3N_4 release is performed in an ICP-RIE Adixen AMS 100 machine at cryogenic temperature (figure 2.1). To investigate its etch characteristics, we fabricated multiple
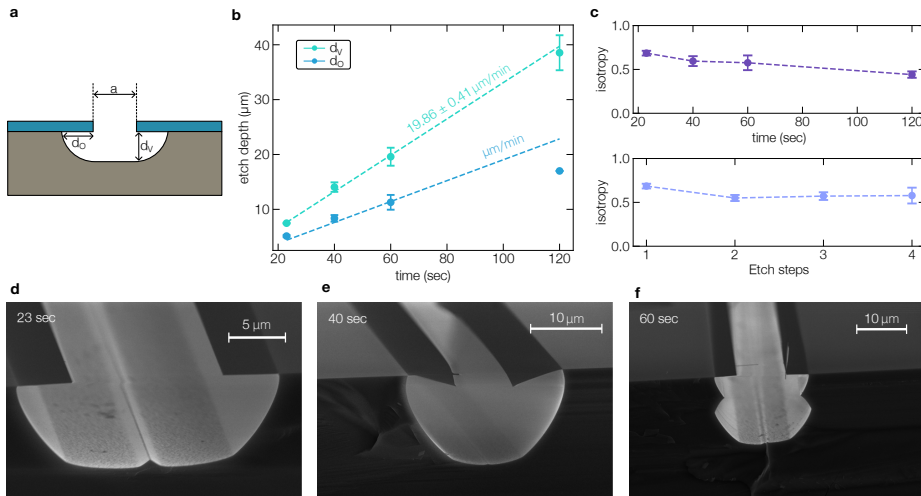
Fig. 2.2 Etch rate and isotropy of SF$_6$ Si etching. **a,** Side view of the Si substrate isotropically etched under the Si$_3$N$_4$ layer. The schematic shows the main parameters used to characterize the etching, the etch depth along the vertical direction (d_V) and the horizontal direction (d_O) and the aperture a. **b,** Etch depth extracted vertical and horizontal direction for different etch time. The error bar for each point indicates the standard deviation. The values written along the dotted line show the mean value of the etch rate calculated for each etch time together with the standard error. **c,** Isotropy calculated as the ratio between d_O and d_V for the different etch time. **d,** Scanning electron microscope pictures of the etch profile after a 23 sec isotropic etch, **e,** a 40 sec isotropic etch, and **f,** a 60 sec isotropic etch.

Si$_3$N$_4$ chips patterned with a series of lines and holes. The chips are then mounted on a carrier wafer with a heat conducting oil. The carrier wafer is coated with a thick oxide layer which prevents the silicon from being etched, while the heat conducting oil allows to both clamp the chips on the wafer and to assure a good thermalization along the entire etching. A stable temperature is crucial to obtain the desired etching profile and to ensure reproducible results. He-backside cooling is applied to the wafer once loaded in the ICP-RIE chamber and the substrate is kept at $-120\,°C$. The chamber pressure during the etching is maintained at 6.9×10^{-2} mbar. The ICP power is set at 2000 W while the capacitive RF power is at 0W, resulting in an applied DC voltage between 12 and 16 V.

The isotropic silicon etching is performed solely by SF$_6$ gas introduced with a flow rate of 500 sscm. After the etching, the carrier wafer is unloaded in the loadlock and stored for 5 minutes under vacuum ($P < 1 \times 10^{-1}$ mbar). This allows a slow thermalization of the fragile suspended structures when passing from the chamber at cryogenic temperature to the loadlock at room temperature. The loadlock is then vented with nitrogen for 5 minutes before unloading the carrier wafer. The chips are removed by gently pushing and lifting them off the surface of the carrier wafer. Finally, the residual oil from their back side is removed by an Ethanol-soaked wipe. Since the etching is performed without any masking layer protecting Si$_3$N$_4$, no additional cleaning steps are needed, which would otherwise affect the fabrication yield.

The etch rate and degree of isotropy for Si are extracted by measuring the width and depth of all the features before and after the etching by scanning electron microscope (SEM) and optical microscope. The etch rate for Si$_3$N$_4$ is calculated by measuring the layer thickness by ellipsometry. The surface roughness measurements are obtained by an Atomic Force Microscope (AFM).

2.3. Results and Discussion
2.3.1. Silicon etch rate and isotropy

Given their high aspect ratio, nanomechanical resonators require an etching step with a high degree of isotropy to fully release the structure from the supporting substrate. The isotropy (I) can be defined as the ratio of the etch depth along the horizontal direction (d$_O$) over the etch depth on the vertical direction (d$_V$) as depicted in Fig. 2.2a:

$$I = \frac{d_O}{d_V} \tag{2.1}$$

where I varies from zero for ideal anisotropic etches to one for ideal isotropic etches. To quantify it, we fabricated multiple chips with a series of lines patterned on the silicon nitride layer, before etching the silicon substrate with different processes time. The chips are then cleaved along the crystal plane to image the resulting etch profile by scanning electron microscopy (SEM). As the images in Fig. 2.2d, e, f show, the etch profile displays an isotropic behavior, without any noticeable preferred direction along the crystal planes. Moreover the etch depth along the vertical and the horizontal directions scales linearly with the etching time, resulting in a constant etch rate over the considered etching time of 120 seconds. The computed etch rate (Fig. 2.2b) is as high as 19.86 μm/min along the vertical direction and 11.43 μm/min along the horizontal direction. The obtained value is

higher than typical etch rates reported for SF_6 silicon etching (1 to 8 μm/min)[28] and for other gases conventional employed as XeF_2[34]. Crucially, the obtained high etch rate is not detrimental to the isotropy of the process.

We believe the difference in the etch rate between the vertical and the horizontal direction is caused by the lower flux in the horizontal direction compared to the vertical direction, the observed residual bias larger than 0 V and marginally to the process temperature[35]. The etch rate in a dry etching process consists of three mechanisms[36]:

$$ER_{tot} = ER_{the} + ER_{phy} + ER_{ion} \tag{2.2}$$

where ER_{the} denotes the thermal etching due to fluorine atoms chemically reacting with the silicon surface, ER_{phy} is the physical etching due to sputtering caused by the high acceleration voltage and ER_{ion} accounts for the ion aided etching. The etching hereby described is a chemical process without any capacitive RF power applied, dominated by spontaneous thermal etching ER_{the}. In this case, it has been demonstrated that the etch rate is directly proportional to the flux of the fluorine atoms[20]. At the surface of the substrate immediately beneath the Si_3N_4 opening, the radicals follow an isotropic trajectory being exposed to open field flux. On the contrary, their access to the substrate in the horizontal direction is restricted by the Si_3N_4 layer. This results in a shadowing effect which reduces the number of radicals and hence the etch rate in the horizontal direction compared to the vertical direction.

At the same time the etching exhibits a DC voltage ranging from 12 and 16 V. This is expected to vertically accelerate SF_6 gas with a twofold effect. On the one hand, the density of fluorine radicals reaching the bottom of the Si substrate increases leading to a lower gas supply to the sidewall given the constant gas flow. Chemical etching of the bottom of the substrate is then enhanced contrary to the sidewall. On the other hand, the accelerated ions result in ion bombardment of the Si substrate along the vertical direction.

The isotropy of the process is also found to decrease with the etch time (Fig. 2.2c). Figure 2.2b shows that this is mainly caused by a reduction of the etch rate along the horizontal direction while the etch rate along the vertical direction remains unaffected. As previously reported[20], this can be explained by the increase in the aspect ratio of the suspended Si_3N_4 during the etching, resulting in a lower flux of fluorine radicals below it. The same behavior is observed when etching the chips for a constant time of 20 seconds multiple times (Fig. 2.2c). This further confirms the hypothesis that the lower flux in the horizontal direction is the main source for the observed isotropic profile.

2.3.2. Features size effect on silicon etch rate

Next, we study the effect of the feature sizes on etch depth and etch rate. To do so, we varied the opening area of the Si_3N_4 layer, denoted with the letter a in Fig. 2.2a. This is achieved by patterning the Si_3N_4 layer with holes with different diameters from 600 nm to 200 um before etching the Si substrate for 120 seconds. The width of the ring-shaped overhang allows the extraction of the etch depth along the horizontal direction and thus the etch rate (Fig. 2.3b, c). The extracted rate increases with the feature size due to a phenomenon known as RIE lag[37] caused by the depletion of radicals. For features size smaller than 50 um, the flux of fluorine atoms entering the trench is limited by the area of the Si_3N_4 aperture. The etch depth and the etch rate are then directly proportional
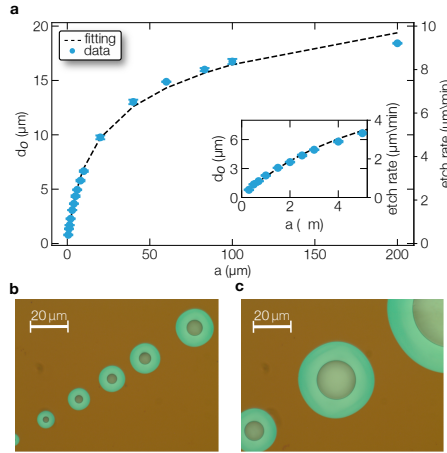
2

Fig. 2.3 Lateral etch rate as a function of the aperture. **a,** Etch depth along the horizontal direction for different aperture sizes of the Si_3N_4 aperture and an equal etch time of 120 seconds. The secondary y-axis on the right side indicates the resulting Si etch rate. The inset shows a zoom for small aperture sizes. The error bar for each point shows the standard deviation. **b-c,** Optical microscope images of the test structures with different apertures (a) used to extract the data in **a**. The dark yellow area is Si_3N_4 not suspended. The light green rings are the overhang consisting of Si_3N_4 suspended over the Si substrate.

to the value of a. The effect becomes less pronounced for larger feature sizes, at which the amount of fluorine atoms in the trench is no longer determined by the area of Si_3N_4 aperture but rather by the gas concentration.

This is particularly relevant for suspending membranes with a high aspect ratio. As shown in the schematic in Fig. 2.1d, e, f, a membrane needs in fact to be patterned with release holes to allow the fluorine atoms to react with the Si substrate. Importantly, the size of the release holes is comparable with the size of photonic crystal operating at telecom wavelength. Photonic crystals increase the reflectivity of membranes and enhance the coupling between their mechanical motion and the incoming light. They are therefore a desirable feature in nanomechanical resonators, specifically for optomechanics applications.

2.3.3. Silicon nitride film quality and suspended resonators

Until now we have studied the effects of SF_6 etching on the Si substrate, however, it is equally important to investigate its influence on the Si_3N_4 layer. The SF_6 dry etching release does not require any masking for the thin Si_3N_4 layer. As such, the latter needs to display high selectivity against fluorine etching. We then performed consecutive etching steps on different chips consisting of a Si substrate with a not patterned Si_3N_4 layer on top. We then measured the thickness of the Si_3N_4 layer at the beginning and the end of each etching by ellipsometry.

Figure 2.4a shows the extracted etch rate as a function of temperature. The data shows a high selectivity of SF_6 gases against Si_3N_4 with an etch rate almost a thousand times

2
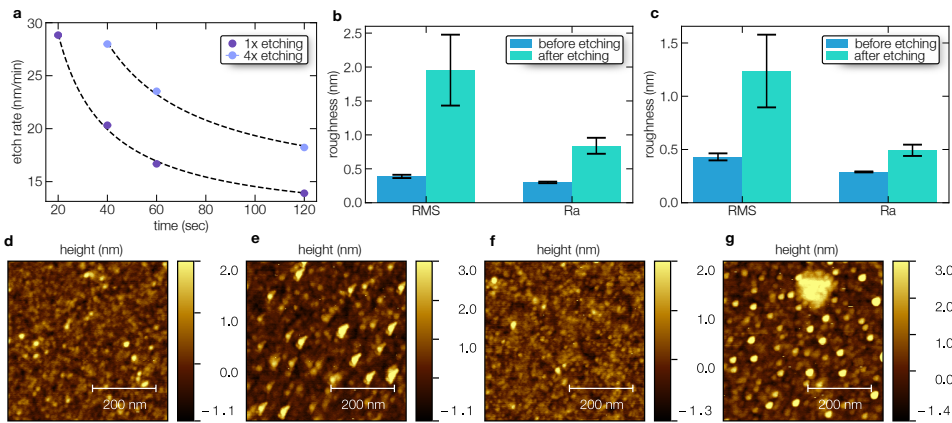
Fig. 2.4 Effect of etching on Si$_3$N$_4$ layer. **a,** Silicon nitride etch rate for a continuous process (1x) and four multiple steps of the same duration (4x) as function of time. **b,** Surface roughness of a 100 nm-thick Si$_3$N$_4$ sample before and after a 10-second etching. The measurement is conducted by AFM employing different scan sizes, 500 nm, 2 µm, and 5 µm. The bar in the graph represents the average value calculated from the three measurements, while the error bar depicts the standard error. **c,** Similar data displayed in **b** but on a sample with a different Si$_3$N$_4$ thickness equal to 50 nm. **d and e**, AFM height from the measurement with the smallest scan size (500 nm) on the 50 nm-thick Si$_3$N$_4$ sample, for the conditions before and after the 10-second etching, respectively. **f and g,** AFM height from the measurement with the smallest scan size (500 nm) on the 100 nm-thick Si$_3$N$_4$ sample for the conditions before and after the 10-second etching, respectively.

smaller than the etch rate measured for Si (Fig. 2.2), crucial to suspend high aspect ratio nanomechanical resonators. The etch rate is however characterized by a continuously declining behavior that can arise from diverse sources, variation of temperature during the etching, alterations of plasma conditions, or changes in surface conditions.

The local temperature on the surface of the device can increase due to the plasma energy and the low thermal conductivity of the substrate, consequently affecting the etch rate. The latter has however been reported to increase proportionally with the process temperature for Si_3N_4, rather than decrease. We therefore believe is not the cause of the observed etch rate behavior.

Plasma conditions are affected by variations in the plasma power and the resulting DC voltage applied to the substrate crated by the physics of the plasma. In our process, the etching is preceded by a millisecond step where a high RF power is applied to ignite the plasma, before turning the capacitive RF power off and maintaining only the ICP power. This results in a high DC power applied to the substrate which can increase the etch rate at the beginning of the process. To investigate this hypothesis we performed four consecutive etchings of the same duration, with a waiting time of one minute in between. The devices are kept inside the etching chamber during the waiting time. The results in Fig. 2.4a show a similar decaying trend for single and multiple etchings but with a different etch rate value. If the etch rate was limited by high RF power applied at the beginning of the process, the etch rate for the multiple etchings should equal the etch rate of the single steps. It follows that the etch rate for a total etching of 40 seconds should be the same as a single process of 10 seconds. The plot in 2.4a demonstrates the opposite and hence process conditions are not expected to be the limiting factor for the observed declining behavior. The plasma is equally affected by gas concentration, however, the reacting gases reaching the device remain constant over time during the process. We therefore can expect gas composition to remain constant without noticeable effects on the etch rate.

Lastly, changing of surface conditions has been reported to affect the etch rate in fluorine-based plasma etching[31,38]. The two main sources for Si_3N_4 are a build-up of charges or the formation of a surface film that inhibits etching. The first is a known phenomenon observed in insulating substrates which cannot conduct the positive charges generated during plasma. Accumulation of positive charges on the surface can then repel incoming ions leading to a reduction of the measured etch rate. The effect is referred to as differential insulating charging. Charged ions can be trapped in Si_3N_4 because of the insulating nature. Moreover, the devices are mounted on top of a carrier wafer coated with a thick silicon oxide layer. We therefore expect differential insulating charging effects in our resonators. Even though our process is a chemical etching predominantly driven by neutrals instead of charged particles, ions are still required in the transport of neutrals and for interactions with them in the plasma.

The formation of the surface film has also been reported to slow down the etch rate of polycrystalline silicon and Si_3N_4 under different plasma gases[38]. SF_6 can create sulfur-containing species on the surfaces, which inhibits etching. The created film is highly volatile and dissipates after the etching. The thickness of the film grows proportionally with the etching, resulting in a continuous decay of the etch rate.

The change of surface conditions, either due to the build-up of charges or the formation of a surface film, is furthermore expected to vary between a single etching and multiple
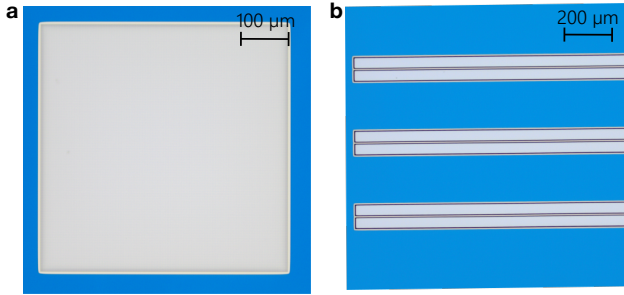
Fig. 2.5 Suspended nanomechanical resonators. **a,** Optical microscope picture of a suspended membrane. **b,** Optical microscope picture of a suspended beam.

etchings. The waiting time between every step of multiple etchings allows in fact to release trapped charges and to reduce the thickness of the highly volatile surface film. The data in Fig. 2.4a provides conclusive evidence of the expected variation of etch rate between single and multiple steps. We thus believe surface conditions are the main source for the temporal decaying behavior of the etch rate.

Next, we investigate the surface quality and specifically the surface roughness of Si_3N_4 after the plasma etching. Surface quality plays a critical role in the resonator's performance, specifically their ability to reach high quality factor. It is thus important that the release technique preserves the film quality. Figure 2.4d,e shows the obtained height signal from atomic force microscope (AFM) of a 50 nm-thick Si_3N_4 before and after SF_6 plasma etching. The pictures show that the latter has a minimal effect on the surface roughness, concentrated in specific areas. The roughness average value (Ra) becomes twice the value measured before the etching while the root mean square value (RMS) increases almost four times (2.4b. The behavior does not exhibit any dependence on the Si_3N_4 thickness, as shows by the AFM pictures (2.4f,g) acquired for 100 nm-thick Si_3N_4. Fig. 2.4c displays the resulting roughness values in terms of Ra and RMS.

Finally, we employ the developed SF_6 plasma etching for suspending two nanomechanical resonators with a high aspect ratio. Figure 2.5a shows a suspended membrane with a lateral size of 500 μm. The membrane is patterned with release holes to allow the SF_6 particles to interact with the Si substrate and quickly suspend the resonator. Figure2.5b shows a suspended beam with a total length of 3 mm and a width of 5 μm. The beam is surrounded by a large opening which enables its release. The initial thickness of both nanoresonators is equal to 100 nm.

It is important to notice that, given its high isotropy, the developed SF_6 etching allows the fabrication of structures of arbitrary shapes with high fidelity. We exploit this characteristic to successfully fabricate membranes patterned with a phononic crystal for MHz frequencies and a later size of 3 mm by an undercut step of only 60 sec. The results are presented in the appendix A of this thesis.

2.4. Conclusion

To conclude, we investigated the etching characteristic of dry isotropic silicon etching by sulfur hexafluoride plasma at cryogenic temperature. The low temperature reduces the Si_3N_4 etching, highly enhancing the selectivity over silicon. The Si_3N_4 surface is negligibly affected by the etching step as confirmed by AFM data, maintaining the low surface roughness measured before the etching. The measured high selectivity makes it possible to avoid any protecting mask during the etching process, which removes the need for additional cleaning steps after the dry etching, with a significant impact on the fabrication yield.

The etching is characterized by a high etch rate of the Si substrate above $10\,\mu m/min$ and a high degree of isotropy, critical for high aspect ratio structure. For large membranes, the structure can be covered with release holes to allow the gas to interact with the Si substrate and avoid overetching of the Si_3N_4 film.

Not only does the process lead to a quick and controllable way to suspend nanomechanical structures, but it also enables the fabrication of designs with arbitrary shapes not constrained to the crystal planes of the substrate, as in wet etching with KOH. This demonstrates the ability of SF_6 plasma etching to suspend high aspect ratio strained nanomechanical resonators with high fidelity, offering a robust alternative to conventional wet etching release processes. The process is intrinsically striction-free and particularly suited for nanomechanical resonators with extreme aspect ratio.

References

1. Steeneken, P. G., Dolleman, R. J., Davidovikj, D., Alijani, F. & van der Zant, H. S. J. Dynamics of 2D Material Membranes. *2D Materials* **8,** 042001 (2021) (cit. on p. 14).

2. Midolo, L., Schliesser, A. & Fiore, A. Nano-Opto-Electro-Mechanical Systems. *Nature Nanotechnology* **13,** 11–18 (2018) (cit. on p. 14).

3. Shin, D., Cupertino, A., de Jong, M. H. J., Steeneken, P. G., Bessa, M. A. & Norte, R. A. Spiderweb Nanomechanical Resonators via Bayesian Optimization: Inspired by Nature and Guided by Machine Learning. *Advanced Materials* **34,** 2106248 (2022) (cit. on p. 14).

4. Gisler, T., Helal, M., Sabonis, D., Grob, U., Héritier, M., Degen, C. L., Ghadimi, A. H. & Eichler, A. Soft-Clamped Silicon Nitride String Resonators at Millikelvin Temperatures. *Physical Review Letters* **129,** 104301 (2022) (cit. on p. 14).

5. Norte, R. A., Moura, J. P. & Gröblacher, S. Mechanical Resonators for Quantum Optomechanics Experiments at Room Temperature. *Phys. Rev. Lett.* **116,** 147202 (2016) (cit. on p. 14).

6. Tsaturyan, Y., Barg, A., Polzik, E. S. & Schliesser, A. Ultracoherent Nanomechanical Resonators via Soft Clamping and Dissipation Dilution. *Nature Nanotechnology* **12,** 776–783 (2017) (cit. on p. 14).

7. Ghadimi, A. H., Fedorov, S. A., Engelsen, N. J., Bereyhi, M. J., Schilling, R., Wilson, D. J. & Kippenberg, T. J. Elastic Strain Engineering for Ultralow Mechanical Dissipation. *Science* **360,** 764–768 (2018) (cit. on p. 14).

8. Pratt, J. R., Agrawal, A. R., Condos, C. A., Pluchar, C. M., Schlamminger, S. & Wilson, D. J. Nanoscale Torsional Dissipation Dilution for Quantum Experiments and Precision Measurement. *Physical Review X* **13,** 011018 (2023) (cit. on p. 14).

9. Hoch, D., Yao, X. & Poot, M. Geometric Tuning of Stress in Predisplaced Silicon Nitride Resonators. *Nano Letters* **22,** 4013–4019 (2022) (cit. on p. 14).

10. Høj, D., Wang, F., Gao, W., Hoff, U. B., Sigmund, O. & Andersen, U. L. Ultra-Coherent Nanomechanical Resonators Based on Inverse Design. *Nature Communications* **12,** 5766 (2021) (cit. on p. 14).

11. de Jong, M. H. J., Ganesan, A., Cupertino, A., Gröblacher, S. & Norte, R. A. Mechanical Overtone Frequency Combs. *Nature Communications* **14,** 1458 (2023) (cit. on p. 14).

12. Sementilli, L., Romero, E. & Bowen, W. P. Nanomechanical dissipation and strain engineering. *Advanced Functional Materials* **32,** 2105247 (2022) (cit. on pp. 14, 16).

13. Schmid, S., Jensen, K., Nielsen, K. & Boisen, A. Damping Mechanisms in High-Q Micro and Nanomechanical String Resonators. *Physical Review B* **84,** 1–6 (2011) (cit. on p. 14).

14. Yu, P.-L., Purdy, T. P. & Regal, C. A. Control of Material Damping in High- Q Membrane Microresonators. *Physical Review Letters* **108,** 083603 (2012) (cit. on p. 14).

15. Tas, N., Sonnenberg, T., Jansen, H., Legtenberg, R. & Elwenspoek, M. Stiction in Surface Micromachining. *Journal of Micromechanics and Microengineering* **6,** 385–397 (1996) (cit. on p. 14).

2

16. Abe, T. & Reed, M. L. Control of Liquid Bridging Induced Stiction of Micromechanical Structures. *Journal of Micromechanics and Microengineering* **6,** 213 (1996) (cit. on p. 14).

17. Jafri, I. H., Busta, H. & Walsh, S. T. Critical point drying and cleaning for MEMS technology. *MEMS Reliability for Critical and Space Applications* **3880,** 51–58 (1999) (cit. on p. 14).

18. Bhushan, B. Adhesion and Stiction: Mechanisms, Measurement Techniques, and Methods for Reduction. *Journal of Vacuum Science & Technology B: Microelectronics and Nanometer Structures Processing, Measurement, and Phenomena* **21,** 2262–2296 (2003) (cit. on p. 14).

19. Norte, R. A. *Nanofabrication for On-Chip Optical Levitation, Atom-Trapping, and Superconducting Quantum Circuits.* PhD thesis (California Institute of Technology, 2015) (cit. on p. 14).

20. Panduranga, P., Abdou, A., Ren, Z., Pedersen, R. H. & Nezhad, M. P. Isotropic Silicon Etch Characteristics in a Purely Inductively Coupled SF_6 Plasma. *Journal of Vacuum Science & Technology B* **37,** 061206 (2019) (cit. on pp. 14, 15, 19).

21. Wang, L., Liu, M., Zhao, J., Zhao, J., Zhu, Y., Yang, J. & Yang, F. Batch Fabrication of Silicon Nanometer Tip Using Isotropic Inductively Coupled Plasma Etching. *Micromachines* **11,** 638 (2020) (cit. on pp. 14, 15).

22. Subhani, K. N., Khandare, S., Biradar, R. C. & Bhat, K. N. Novel Fabrication of Fixed Suspended Silicon Nitride Structure for MEMS Devices with Dry Etching. *IOP Conference Series: Materials Science and Engineering* **872,** 012157 (2020) (cit. on pp. 14, 15).

23. Norte, R. A., Forsch, M., Wallucks, A., Marinkovic, I. & Gröblacher, S. Platform for Measurements of the Casimir Force between Two Superconductors. *Physical Review Letters* **121,** 030405 (2018) (cit. on pp. 14, 15).

24. Dussart, R., Tillocher, T., Lefaucheux, P. & Boufnichel, M. Plasma Cryogenic Etching of Silicon: From the Early Days to Today's Advanced Technologies. *Journal of Physics D: Applied Physics* **47,** 123001 (2014) (cit. on p. 14).

25. de Boer, M., Gardeniers, J., Jansen, H., Smulders, E., Gilde, M.-J., Roelofs, G., Sasserath, J. & Elwenspoek, M. Guidelines for Etching Silicon MEMS Structures Using Fluorine High-Density Plasmas at Cryogenic Temperatures. *Journal of Microelectromechanical Systems* **11,** 385–401 (2002) (cit. on p. 14).

26. Jansen, H., Gardeniers, H., de Boer, M., Elwenspoek, M. & Fluitman, J. A Survey on the Reactive Ion Etching of Silicon in Microtechnology. *Journal of Micromechanics and Microengineering* **6,** 14–28 (1996) (cit. on p. 14).

27. Donnelly, V. M. Review Article: Reactions of Fluorine Atoms with Silicon, Revisited, Again. *Journal of Vacuum Science & Technology A* **35,** 05C202 (2017) (cit. on p. 14).

28. Hays, D. C., Jung, K. B., Hahn, Y. B., Lambers, E. S., Pearton, S. J., Donahue, J., Johnson, D. & Shul, R. J. Comparison of F 2-Based Gases for High-Rate Dry Etching of Si. *Journal of The Electrochemical Society* **146,** 3812 (1999) (cit. on pp. 14, 19).

29. Legtenberg, R., Jansen, H., de Boer, M. & Elwenspoek, M. Anisotropic Reactive Ion Etching of Silicon Using SF 6 / O 2 / CHF 3 Gas Mixtures. *Journal of The Electrochemical Society* **142,** 2020–2028 (1995) (cit. on p. 15).

30. Tilli, M., Paulasto-Krockel, M., Petzold, M., Theuss, H., Motooka, T. & Lindroos, V. *Handbook of silicon based MEMS materials and technologies* (Elsevier, 2020) (cit. on p. 15).

31. Henry, M. D., Welch, C. & Scherer, A. Techniques of Cryogenic Reactive Ion Etching in Silicon for Fabrication of Sensors. *Journal of Vacuum Science & Technology A* **27,** 1211–1216 (2009) (cit. on pp. 15, 22).

32. Mellhaoui, X., Dussart, R., Tillocher, T., Lefaucheux, P., Ranson, P., Boufnichel, M. & Overzet, L. J. SiOxFy Passivation Layer in Silicon Cryoetching. *Journal of Applied Physics* **98,** 104901 (2005) (cit. on p. 15).

33. Yang, C. & Pham, J. Characteristic Study of Silicon Nitride Films Deposited by LPCVD and PECVD. *Silicon* **10,** 2561–2567 (2018) (cit. on p. 16).

34. Xu, D., Xiong, B., Wu, G., Wang, Y., Sun, X. & Wang, Y. Isotropic Silicon Etching With \hboxXeF_2 Gas for Wafer-Level Micromachining Applications. *Journal of Microelectromechanical Systems* **21,** 1436–1444 (2012) (cit. on p. 19).

35. Bartha, J. W., Greschner, J., Puech, M. & Maquin, P. Low Temperature Etching of Si in High Density Plasma Using SF6/O2. *Microelectronic Engineering* **27,** 453–456 (1995) (cit. on p. 19).

36. Arnold, J. C., Gray, D. C. & Sawin, H. H. Influence of Reactant Transport on Fluorine Reactive Ion Etching of Deep Trenches in Silicon. *Journal of Vacuum Science & Technology B: Microelectronics and Nanometer Structures Processing, Measurement, and Phenomena* **11,** 2071–2080 (1993) (cit. on p. 19).

37. Jansen, H., de Boer, M., Wiegerink, R., Tas, N., Smulders, E., Neagu, C. & Elwenspoek, M. BSM 7: RIE Lag in High Aspect Ratio Trench Etching of Silicon. *Microelectronic Engineering. Micro- and Nano- Engineering 96* **35,** 45–50 (1997) (cit. on p. 19).

38. Loewenstein, L. M. Selective Etching of Silicon Nitride Using Remote Plasmas of CF4 and SF6. *Journal of Vacuum Science & Technology A* **7,** 686–690 (1989) (cit. on p. 22).

2

3

Spiderweb nanomechanical resonators via Bayesian optimization: inspired by nature and guided by machine learning

From ultrasensitive detectors of fundamental forces to quantum networks and sensors, mechanical resonators are enabling next-generation technologies to operate in room-temperature environments. Currently, silicon nitride nanoresonators stand as a leading microchip platform in these advances by allowing for mechanical resonators whose motion is remarkably isolated from ambient thermal noise. However, to date, human intuition has remained the driving force behind design processes. Here, inspired by nature and guided by machine learning, a spiderweb nanomechanical resonator is developed that exhibits vibration modes, which are isolated from ambient thermal environments via a novel "torsional soft-clamping" mechanism discovered by the data-driven optimization algorithm. This bioinspired resonator is then fabricated, experimentally confirming a new paradigm in mechanics with quality factors above 1 billion in room temperature environments. In contrast to other state-of-the-art resonators, this milestone is achieved with a compact design that does not require submicrometer lithographic features or complex phononic bandgaps, making it significantly easier and cheaper to manufacture at large scales. These results demonstrate the ability of machine learning to work in tandem with human intuition to augment creative possibilities and uncover new strategies in computing and nanotechnology.

3

3.1. Introduction

$\mathbf{M}$ ajor advances in nanotechnology have allowed mechanical resonators to improve dramatically over the last decades. One of the most sought after characteristics for a mechanical resonator is noise isolation from thermal environments, namely at room-temperature conditions where thermomechanical noise can dominate. The degree of mechanical isolation is characterized by a resonator's mechanical quality factor, Q_m. Typically, Q_m is defined as the ratio of energy stored in a resonator over the energy dissipated over one cycle of oscillation. Inversely, mechanical quality factors can indicate the dissipation of mechanical noise into a resonator from ambient environments. For mechanical sensors, a resonator's isolation from ambient thermal noise can greatly enhance its ability to detect ultrasmall forces, pressures, positions, masses, velocities, and accelerations. For quantum technologies, the mechanical quality factor dictates the average number of coherent oscillations a nanomechanical resonator (in the quantum regime) can undergo before one phonon of thermal noise enters the resonator and causes decoherence of its quantum properties[1]. From microchip sensing to quantum networks, cryogenics are conventionally required to counteract thermal noise but enabling these burgeoning technologies to operate in ambient temperatures would have a significant impact on their widespread use.

In room-temperature environments, on-chip mechanical resonators with state-of-the-art quality factors have mostly consisted of high-aspect-ratio suspended nanostructures fabricated from tensile thin films. Silicon nitride (Si_3N_4) films have been the material of choice for their high intrinsic stress, yield strength, temperature stability, chemical inertness, and prevalence in nanotechnology. Over the years, researchers have developed improved design principles that manipulate the strain, bending, and mode shape in nanomechanical resonators to improve quality factors, which are ultimately limited by bending losses as the resonator oscillates in vacuum. Another important characteristic is the mechanical frequency of a nanomechanical resonator's vibrational mode, f_m. For high-precision detectors of fundamental forces like gravity[2] and dark matter[3] and quantum-limited commercial sensors,[4,5] resonators with high Q_m and low f_m are a long-standing goal. Minimizing f_m/Q_m is a key figure-of-merit towards quantum-limited force[6] or acceleration[7] sensitivities (S_f, $S_a \propto (f_m/Q_m)^{0.5}$) and for enabling quantum sensing of forces like dark matter[8,9] and gravity[10,11] where low frequency and higher quality factor are advantageous. For phonon-based quantum technologies, a mechanical resonator's vibrational modes are initialized into the quantum regime, where their motion harbors less than one quanta of vibration (phonon)[12,13]. Mechanical resonators in these quantum regimes must have sufficiently high $Q_m \times f_m > k_B T_{room}/h$ to suppress the effects of room temperature, T_{room}, thermal noise on their fragile quantum properties. While there are only a handful of platforms[14–21] to overcome these stringent requirements on $Q_m \times f_m$ at room temperature, a general goal has been to achieve the highest Q_m and lowest f_m possible while still maintaining $Q_m \times f_m$ above 6×10^{12} Hz.

Previously proposed nanomechanical resonators follow strategies largely motivated by 1D analytical models of resonators[23] because they provide easy-to-interpret design rules. It is important to note that while silicon nitride has been conventionally used for high-Q resonators, these design principles are valid for nearly any strained thin-film material. These analytical models show that higher strain (i.e., higher stress σ and low Young's
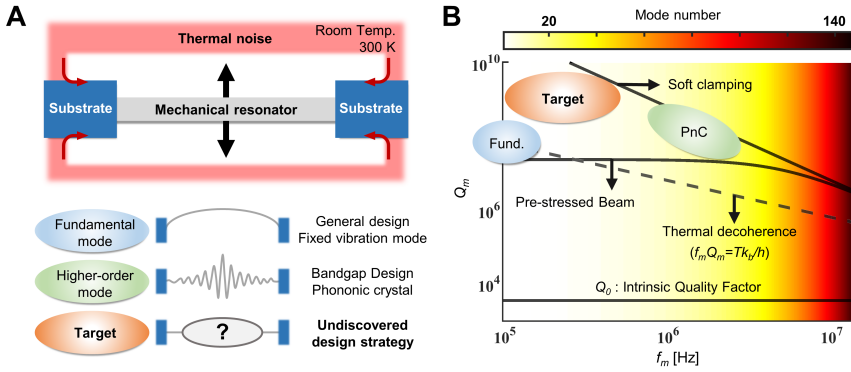
Fig. 3.1 A Illustration of the mechanical resonator and target vibration modes for a high quality factor resonator. Unlike fundamental modes[20,22], or higher-order modes[15], the target mode shape for lower-order mode hadn't been discovered. **B** Quality factor (Q_m) versus frequency (f_m) for a double clamped 50 nm thick 3 mm long silicon nitride beam. The bottom solid line corresponds to the intrinsic quality factor of Si_3N_4 on the string resonator caused by friction on the surface and the bulk of the resonator due to material imperfections. The intermediate solid line shows the effect of an applied high pre-stress of 1 GPa, and the upper solid line the effect of complete elimination of clamp losses (perfect soft-clamping). The dashed line corresponds to the mechanical decoherence constraint, indicating that the resonator having the quality factor above can complete one full coherent oscillation without a thermal phonon entering the resonator. The figure highlights the target unexplored region of designs with high quality factors and lower-order modes.

modulus E), longer (L) and thinner (t) geometries generally lead to higher quality factors in both nanomechanical membranes and strings. For example, f_m/Q_m of the double clamped beam's fundamental mode is proportional to $\sqrt{E}/L^3$ ($L + 1.4t\sqrt{E/\sigma}$), when assuming a thin long pre-stressed beam (explicit formulation can be found in the Supporting Information). While increasing the aspect-ratio of resonators usually leads to smaller f_m/Q_m, it also makes them much more challenging to fabricate reliably. **Figure 3.1A** illustrates conventional design strategies. When considering the fundamental mode of resonators, mechanical quality factors are typically improved by pre-stressing – a form of strain engineering called dissipation dilution[24−27] which increases stored energies and lowers dissipation compared to unstressed resonators. It overcomes the fundamental limit of the material's intrinsic damping from its bulk and surface, enabling a higher quality factor by orders of magnitude. Simultaneously, resonator models[23] also explain that for high-aspect-ratio[†] pre-stressed resonators ($t \ll L$) the dominating loss that decreases Q_m is due to the mode's sharp curvature at the clamped boundary between the oscillating element and the substrate (on which the resonators are fabricated). This observation motivated the use of phononic crystals (i.e., phononic bandgap) which confine a higher-order mode from the clamping regions using a periodic pattern around the mode. Now rather than having large curvature near the edges, the phononic crystals enable a soft-clamping[15,19,21] to re-

---

[†]The term high-aspect-ratio in this context refers to thin-film resonators characterized by lateral length significantly larger than their thickness.

duce the mode's curvature close to the rigid clamp, and thereby eliminating this dissipation mechanism when operating at high-order vibration modes as depicted in the schematic in **Figure 3.1A**. Phononic crystals enable higher quality factors that approach hundreds of millions, at the cost of operating at higher frequencies and typically requiring higher-aspect-ratio resonators which are more difficult to manufacture reliably.

To illustrate the design space, **Figure 3.1B** shows the mechanical quality factor Q_m versus vibration frequency f_m for a 50 nm thick and 3 mm-long Si_3N_4 beam. The color scale indicates the various out-of-plane vibration modes, from fundamental to higher-order modes with shorter wavelengths. The Supporting Information ("Lessons from string resonators") provides additional information about the bounds shown in the figure. The considered pre-stressed double clamped beam shows the improvement of Q_m caused by enhancement of stored energy (intermediate solid line) when compared to the unstressed beam (horizontal solid line at the bottom, Q_0) and the improvement caused if perfect soft-clamping is achieved around the region shown in **Figure 3.1A** (top solid line). These lines help illustrate the design region in the graph's top left corner that remains largely un-explored in current resonators that aim mainly for high quality factors. Previous works have focused on increasing Q_m of the fundamental mode with strain engineering[6,20], in-cluding design strategies as topology optimization[17,28] or hierarchical designs[16,22]. Here we pursue high quality factors at lower frequencies by following a new approach inspired by nature and guided by machine learning.

3.2. Bio-inspired design

Spiderweb designs have unique geometries that make them one of the most well-known and fascinating classes of micromechanical structures found in nature. Despite their ubi-quitous presence, experts from physics, materials science, and biology are still uncovering the elusive mechanics of spiderwebs that enable them to be remarkably robust vibra-tion sensors[29,30]. Spider silk threads have high toughness and stiffness, reaching yield strengths of the order of a gigapascal – about five times higher than steel[31] and about the same as Si_3N_4. They are used to create lightweight fibrous web structures which harbor an extraordinary strength-to-weight ratio rarely observed among other structures found in nature or science[32−35]. Furthermore, in the case of spiders that sense their prey via webs, these structures are designed to be most sensitive to vibrations emanating from the web and not from surrounding environmental vibrational disturbances[36−39]. Since their unique sensing capabilities have been relentlessly optimized over millions of years of complex evolutionary competition,[40−42] spiderwebs stand as a promising starting point for machine-learning algorithms to design nanomechanical sensors[43−45].

Without making any assumptions about how a spiderweb functions as a vibrational sensor in nature, we propose a web-like structure composed of radial beams, lateral beams, and junctions between them, as shown in **Figure 3.2**. Instead of spiderweb threads which are micrometers thick, we consider highly stressed Si_3N_4 that can be as thin as 20 nm while being suspended over several millimeters. The properties of Si_3N_4 were considered to be E=250 GPa, ν=0.23, ρ=3100 kg/m^3 with an initial released stress of 1.07 GPa based on measurements. The parameterized model shown in **Figure 3.2** includes six design pa-rameters, d, w_1, w_2, l_1, l_2, and N_r. The two inner rings (i.e., the rings formed by the lateral beams) were constrained to have at least a distance of 8 μm between them. We also con-
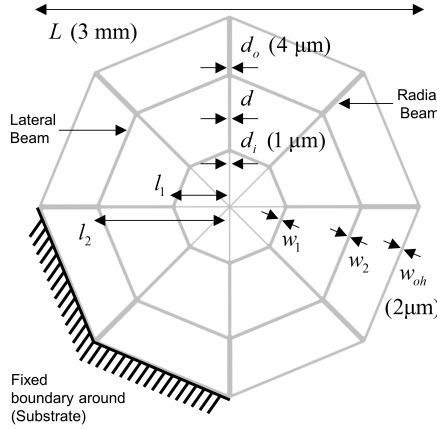
Fig. 3.2 Spiderweb nanomechanical resonator model with $N_r = 8$. d, w_1, w_2, l_1, and l_2 are the design parameters, d_i, d_o, w_{oh}, and L are set as 1 μm, 4 μm, 2 μm, and 3 mm, respectively.

sidered even numbers between 4 to 16 for the number of lateral beams per ring, N_r. Note that the even number of N_r was considered to include not only the symmetric but also the antisymmetric periodic boundary condition. The beam width at the outer and inner parts of the radial beams (d_o and d_i) were taken to be 4 μm and 1 μm, respectively. The width of the structure at the resonator-substrate interface, w_{oh}, was set to 2 μm (half the maximum beam width) in the finite element model to reflect the inevitable overhang originating from the fabrication process. The fixed boundary condition around the resonator is modeled to reflect the overhang attached to a fixed substrate. Additionally, we gave a 1 μm radius fillet for every corner at the junction of lateral and radial beams. By limiting the model's features such as tether widths and fillets to micrometer scales (rather than sub-micrometers), it ensures that these structures can ultimately be defined using photolithography which allows for significantly easier, large-scale fabrication. Finally, the simulation model in the paper considers L, t as 3 mm and 50 nm, respectively. From the simulation, we estimated the mechanical quality factor of the resonator by calculating the dissipation dilution[27,46] of the out-of-plane vibration modes. The quality factors are calculated as,

$$\frac{Q_m}{Q_0} = \frac{12(1-v^2)}{Et^2} \frac{\int \alpha dS}{\int \beta dS} \tag{3.1}$$

with α and β being defined as,

$$\alpha = \sigma_{xx} u_{z,x}^2 + \sigma_{yy} u_{z,y}^2 + 2\sigma_{xy} u_{z,x} u_{z,y} \tag{3.2}$$

$$\beta = u_{z,xx}^2 + u_{z,yy}^2 + 2v u_{z,xx} u_{z,yy} + 2(1-v) u_{z,xy}^2 \tag{3.3}$$

with u_z being the out-of-plane displacement during vibration, and σ the stress distribution resulting from static analysis for the initial stress. The comma denotes a partial derivative with respect to that coordinate. Q_0 is the intrinsic quality factor defined as

$Q_0^{-1} = Q_{\text{volume}}^{-1} + Q_{\text{surface}}^{-1}$, where Q_{volume} is the bulk material loss of Si_3N_4 independent of the resonator's geometry, and Q_{surface} is the surface loss that varies linearly with the resonator's thickness[47]. For thin resonators at room temperature, we assume $Q_0 \approx 6900\, t/100$ nm[48]. Note that α is proportional to the elastic energy in tension, which corresponds to the energy stored in the resonator, and β is proportional to the bending loss. The detailed derivation is provided in the Supporting Information ("Derivation of the quality factor for two-dimensional structures"). With the parameterized model, we aimed to find the highest quality factor considering general types of mode shape below 1 MHz, which is the tenth mode frequency of the same size of the pre-stressed string in **Figure 3.1B**. Given that the length L of our spiderweb nanomechanical resonators is limited to 3 mm, this ensures a target frequency in the hundreds of kHz regime.

3.3. Bayesian optimization

The choice of optimization algorithm to guide the data-driven design process represents the most crucial part for solving real application problems and depends on the characteristics of the problem and data availability. For example, recently machine-learning algorithms have proved their success in material design problems with abundant data[49–51]. On the contrary in this case, a new resonator is designed based on a new spiderweb model shown in **Figure 3.2** and therefore, no prior data is available. Trial-and-error experimentation is difficult because conducting a single experiment of a particular design takes several days of fabrication and testing. In addition, fast analytical predictions of the quality factors and vibrational mode frequencies of designs are also not possible due to the complexity of the 2D geometry, which also requires to consider of various vibration mode shapes. In fact, finite element analyses of these structures are computationally expensive; taking between 10 and 30 minutes using 20 CPU cores of our high performance computing cluster. Despite only considering periodic boundary conditions and simulating only a fraction of the total structure, these long simulation times arise from the fine mesh of elements required by the high aspect-ratio structure such that the subtle shape curvatures are captured in small but crucial regions, such as joints. The geometry is meshed with 4 to 6 elements in the beam's width direction using shell elements, and the mesh resolution near the joints is about double that (details of the finite element model information can be found in the Supporting Information). Therefore, a week of computation can only generate data corresponding to less than 1000 design iterations. This is then classified as a data-scarce optimization problem where each new design iteration should be as informative to the design goal as possible. Under these conditions, using datascarce machine learning to guide the optimization process is particularly effective, as achieved by the Bayesian Optimization method[52–54].

Bayesian optimization[55] constructs a machine learning regression model usually from Gaussian processes[56], by predicting model uncertainty and seeking the optimum solution in fewer iterations than competing algorithms[57,58]. Applying the algorithm to new problem domains, which requires new kinds of surrogate models without pre-domain knowledge as in our problem, is especially beneficial[58]. For readers unfamiliar with the topic, the Supporting Information includes a short introduction to the method. In the context of designing the spiderweb nanomechanical resonator, Bayesian optimization is expected to not only explore the design space to find new vibrational modes that induce soft-clamping

with a compact design, but also use them to reach high quality factors in the low frequency regime for a given resonator size. In this work, we used the GPyOpt python implementation of the method[59], and MATLAB for the pre- and post-processing of our spider-web design. The finite element analysis was performed by COMSOL[60].
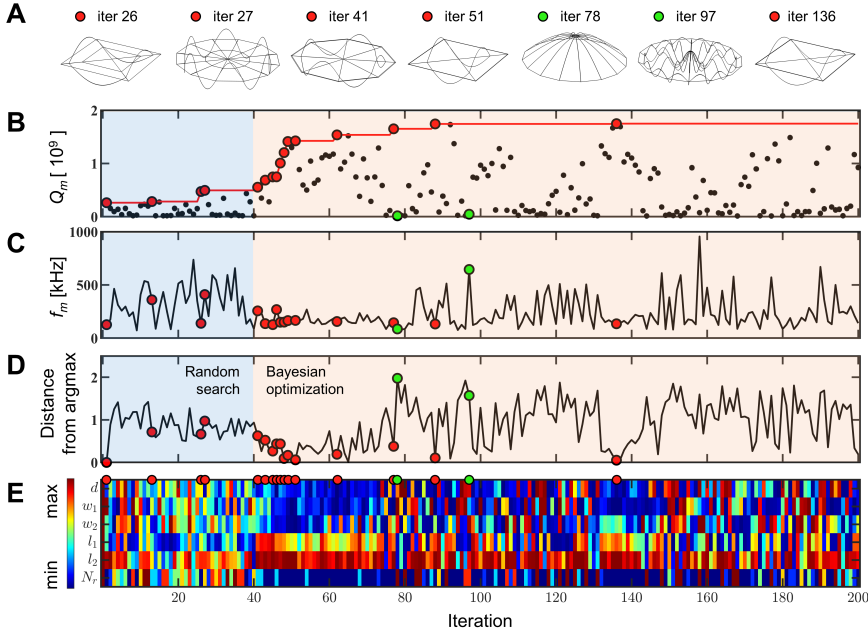

Fig. 3.3 Overview of the Bayesian optimization process for designing the spiderweb nanomechanical resonator: **A** designs and simulated mode shapes at the corresponding iterations highlighted by circular markers in the remaining figures (the enlarged figures are in the Supporting Information); **B** evolution of the quality factor Q_m (the red markers and red line indicate the highest quality factor until that iteration); **C** the frequency f_m; **D** the distance from a previous optimized point to the point considered in that iteration; and **E** values of the 6 design parameters at every iteration, providing an idea of how the designs change in the optimization process ($4 \leq N_r \leq 16$, $1\ \mu m \leq (d, w_1, w_2) \leq 4\ \mu m$, $0\ mm < l_1 < l_2 < 1.5\ mm$). The abscissa for **B**–**E** is the same and corresponds to the design iterations as the optimization process evolves. The blue region in **B**–**D** corresponds to the 40 initial designs that were randomly selected, i.e. before starting the Bayesian optimization process; while the red region corresponds to the Bayesian optimization iterations.

Figure 3.3 refers to the optimization history wherein the spiderweb nanomechanical resonator's quality factor is maximized. The process starts with a random search of 40 iterations to train the model (shown in light blue), followed by the Bayesian optimization phase (shown in light red). **Figure 3.3B** shows the evolution of the quality factor Q_m, while **Figure 3.3D** plots the distance from a previous optimized point to the point considered in that iteration (the distance between the normalized input vectors). As seen in **Figure 3.3A**, the random search from iterations 1-40 find vibrational modes with the highest quality factors in iteration 26 and 27 which vibrate in the outer lateral ring. When the Bayesian

optimization starts at iteration 41 (red markers), it begins to follow the vibrational modes concentrated on the inner lateral beams. Even though iteration 41 starts with a quality factor similar to the one found in the random search (light blue region), the algorithm continues *exploiting* the optimal design region without going too far from this successful iteration, as can be seen in **Figure 3.3D** between iterations 41 and 51, mostly by finely tuning design parameters as can be seen in **Figure 3.3E**. In these iterations, the design improves the quality factor by more than 180% compared to the best value obtained from the first 40 random searches and the machine-learning model promotes local optimization.

Note that the optimal modes found during the Bayesian optimization process correspond to vibrational modes (iterations 41, 51, 136 in **Figure 3.3A**) which harbor only a slight deformation near the clamping points because the major bending elements are in the intermediate ring. Surprisingly, these lateral vibrational modes mimic actual vibrations utilized in spider webs for prey detection[61]. Without encoding any prior knowledge about how spiderwebs function, the machine-learning algorithm was able to find how actual spiderwebs work in nature and adapt it to silicon nitride nanostructures. After iteration 51, the algorithm starts *exploring* the design space more to search for a better design far from the previous optimal, which can be seen from the high values in **Figure 3.3D**. This trade-off between exploration and exploitation is often responsible for the competitive advantage of Bayesian optimization when compared to other algorithms. The green markers in **Figure 3.3** are clear examples of the Bayesian optimization *exploring* far from previous optima. Note that the lateral beam's vibrational mode did not always have the highest quality factor, as optimum performance arises from the discovery of this new mode in combination with geometric parameters that promote bending and torsion in a particular way, as discussed later. By *exploring* and *exploiting* simultaneously to optimize the quality factor of the mechanical resonator, the algorithm reaches a maximum quality factor in iteration 136. Bayesian optimization consistently balances *exploitation* and *exploration*, so the solution for a large number of iterations could lead to continuous improvement. The result here considers up to 200 iterations for the optimization, considering a few days for optimization. In the case of having thousands of data sets regardless of the computational cost, the consideration of additional design parameters could be interesting for future work. As seen in **Figure 3.3C**, we also found that the highest quality factors Q_m occur at lower frequencies, which agrees with the simplified 1D model of the beam resonator. Note that the convergence speed and the optimum result could depend on the initial search points. The comparison study can be found in the Supporting Information ("Optimization convergence dependency on the initial random points"). Moreover, the optimization process also shows that thinner structures are not necessarily better when using micro-wide tethers – a counter-intuitive finding given that every previous design of nanomechanical resonators had out-of-plane mechanical modes with Q_m that benefited from thinner geometries. The detailed discussion can be found in the Supporting Information ("Conversion of energy loss regarding the thickness of the spiderweb nanomechanical resonator").

The optimum spiderweb nanomechanical resonator is predicted to have a quality factor Q_m above 1.75 billion at 134.9kHz for a design considering a diagonal size of 3 mm and a thickness of 50 nm. **Table 3.1** shows the design parameters corresponding to this design. Comparatively, what is striking about this design is that it is able to achieve a
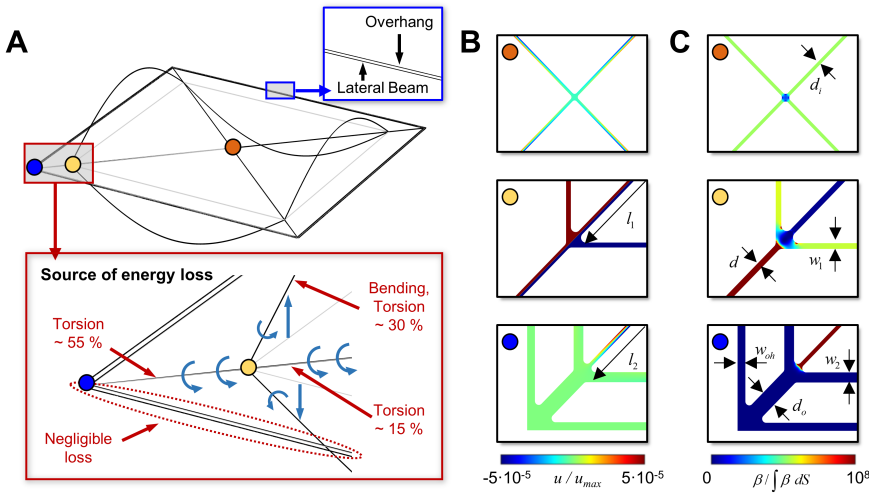
Fig. 3.4 Optimized spiderweb design exhibiting a soft-clamping mode. **A** The full motion of the optimized vibration mode shape with a zoom around the overhang and an illustration of the portion of energy loss. The gray part in this figure shows the structure at rest (no vibration). **B** Shows the local deformations and **C** the normalized bending loss density for the three regions in **A**. From top to bottom: center (orange marker), joint of the inner lateral beam (yellow marker), and the edge (blue marker).

quality factor Q_m above a billion without requiring any tether widths under a micrometer. This allows it to be readily defined using large-scale photolithography which further makes manufacturing faster and cheaper. This is extremely beneficial for real applications in that it decreases the resonators' microchip footprint. For thermal management, a lower aspect-ratio is very beneficial as typically Si_3N_4 nanoresonators are interfaced with optics for high-precision sensing and quantum application. Although Si_3N_4 is preferred for its low optical absorption[26,62], even small amounts of optical heating can have deleterious consequences for high-precision experiments, and having a smaller aspect-ratio allows for enhanced thermal conduction (to the substrate) which scales as t/L. What is important to note is that previous nanomechanical resonators followed a common design paradigm wherein the maximal amplitude of the mode is in the center of the resonator and where the aim is to reduce bending losses from that center to the substrate. Here the algorithm takes an entirely different route by looking at modes that oscillate laterally like a mechanical whispering gallery mode, allowing for tiny distances between amplitude maxima and substrate, providing new insight into the nanomechanical resonator design.

Table 3.1 Optimal design parameters for the spiderweb resonator, when d_i, d_o, w_{oh}, and L are set as 1 μm, 4 μm, 2 μm, and 3 mm, respectively.

N_r	d	w_1	w_2	l_1	l_2
4	1.05 μm	1 μm	2.46 μm	1.21 mm	1.48 mm

Figure 3.4 provides additional details about the optimum design, where **Figure 3.4A** highlights the novel "torsional soft-clamping" mechanism found by the data-driven strategy. This design yields an unprecedentedly high quality factor because the resonator vibrates with an out-of-plane deformation that is localized in the inner ring of lateral beams while undergoing torsional deformation of the radial beams. **Figure 3.4B** and **C** also support this observation, where the displacement magnitude (**B**) and normalized bending loss (**C**) clearly demonstrate the low displacement and bending losses at the boundary (blue marker) while the joint of the inner lateral ring (yellow marker) undergoes significant deformation. As a consequence of the radial beams' torsional motion, the curvature between the bending lateral beam with the radial beam at the clamping point is not highly concentrated, thus significantly diminishing the clamping losses at these points. Although the torsional motion of the radial beams leads to 70 % of the energy dissipation, it is comparable to the bending losses in the deforming lateral beams. Note that the normalized bending loss in **Figure 3.4C** indicates that the bending energy near the joint of the inner lateral beam (yellow marker region) is spread out in the region near the joint, which avoids sharp curvatures that can ultimately limit Q_m. Additionally, the blue marker region of **Figure 3.4A** shows that the outer lateral beams near the boundary prevent deformation and bending loss from propagating toward the boundary in a subtle way by preventing torsional deformation in the radial beams from propagating to the boundary. Unlike the bending loss density of the string's bending modes[23] (where it is highly concentrated on the clamping region), the torsional bending loss density in the spiderweb resonator does not highly concentrate where the vibration stops. For this reason, simulations without the outer lateral beams also gave a similar quality factor. Nonetheless, the optimized position of the outer ring was used to block the torsion propagation from the inner ring to the chip, enhancing the resonator's isolation from the substrate.

The optimized N_r is 4, which maximizes the side beam length when all other parameters are the same. This trend shows that the optimized mode aimed to make the vibrating lateral beams as long as possible, as the quality factor of a string resonator[27] increases for a longer beam. Compared with the 1D approach[14,15], which is a subset of our structure by considering N_r = 2, the web-like structure in the 2D domain has the potential to achieve higher Q_m by exploring novel soft-clamping motions compared to the limited number of vibration modes[16] of the 1D structure. The optimized l_2, which defines the distance between the centre and the inner radial beam, was close to the maximum limit, while the number of radial beams N_r was minimized. This trend shows that the optimized mode aimed to make the vibrating lateral beams as long as possible, as the quality factor of a string resonator[27] increases for a longer beam. Also, the w_2 was optimized at 1 μm which represents the minimum limit allowed. Allowing for widths thinner than 1 μm would likely increase the quality factor. While the lateral size, L, was limited to 3 mm, a study of increasing L (discussed in the Supporting Information) also shows that the optimized Q_m scales quadratically with the size of the resonator while f_m/Q_m is significantly reduced. All of these mechanisms work together to achieve a compact design with an ultrahigh quality factor at a lower order vibration mode via a novel soft-clamping approach that does not require the use of phononic crystals or sub-micrometer lithographic features. Notwithstanding, up to now this finding remains a computational prediction.
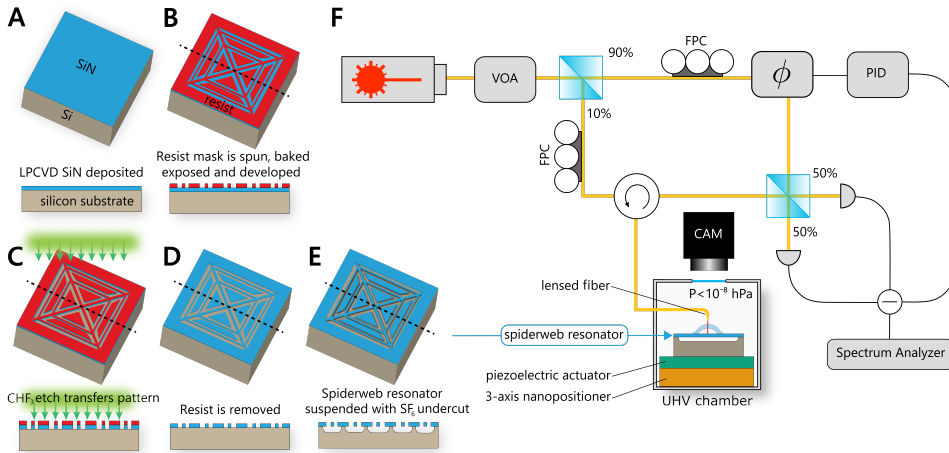
Fig. 3.5 Schematic representation of the fabrication process flow and the mechanical characterization setup. Process steps consist of **A** deposition of Si_3N_4 onto a silicon substrate **B** mask patterning **C** Si_3N_4 patterning via dry etching **D** mask removing and **E** Si_3N_4 undercut and release. **F** The spiderweb nanomechanical resonator is resonantly driven by a piezoelectric actuator and its motion is optical measured with a balanced homodyne interferometer. The resonator is placed inside a UHV chamber to reach a pressure lower than 10^{-8} mbar. VOA: Variable Optical Attenuator. PID: Proportional Integral Derivative Controller. FPC: Fiber Polarization Controller. Φ: fiber stretcher.

3.4. Fabrication and experimental validation

While we have so far described the computational design process that occurred without experimental trial-and-error, the performance of the novel resonator needs to be experimentally validated. To do this we fabricate the optimal resonator and experimentally determine the quality factor of the system from a ringdown measurement in the ultrahigh-vacuum (UHV) setup shown in **Figure 3.5F** to avoid air damping. Ringdown measurements involve using piezoelectric stages to resonantly excite the motion of nanomechanical resonators, stopping the drive, and observing the decay of the resonators' motion via interferometric optical readout. The rate of decay of the resonator's amplitude gives its rate of energy dissipation and thus its mechanical quality factor. The spiderweb nanomechanical resonator is fabricated on high-stress Si_3N_4 grown by low-pressure chemical vapor deposition (LPCVD) on a silicon wafer (**Figure 3.5A**). The pattern is first written on a resist mask (**Figure 3.5B**), then transferred on the Si_3N_4 layer with a directional CHF_3 plasma etching (**Figure 3.5C**). After that, the resist mask is removed (**Figure 3.5D**), and the spiderweb nanomechanical resonator is suspended by a fluorine-based (SF_6) dry etching step (**Figure 3.5E**), which does not require any mask or additional cleaning steps, making the fabrication considerably easier, higher yield and higher quality. Crucially, this fabrication process allows for remarkable agreement between experimental results and idealized simulations that allow us to reliably use the latter as data points for the machine learning algorithm. A detailed explanation of the fabrication process and the mechanical characterization setup is summarized in the Experimental Section. **Figure 3.6A**

shows a scanning electron microscope image of the fabricated device, where the suspended Si_3N_4 spiderweb nanomechanical resonator is highlighted in blue, surrounded by dummy Si_3N_4 islands disconnected from the suspended structure, used to prevent overetching and overexposure (in light gray). The thermomechanical noise spectra as obtained by interferometric optical readout at the center of the spiderweb nanomechanical resonator (orange marker) and the inner lateral beam (pink marker) are plotted in **Figure 3.6C**. As shown in the figure, the optimal vibration mode occurring around 133.6 kHz is visible in the spectrum of the inner ring but has no amplitude in the center of the resonator and therefore well confined, contrary to the fundamental mode at 81.8 kHz. This corroborates the presence of the novel soft-clamping mode shown in **Figure 3.4**. Furthermore, the simulated out-of-plane vibration mode frequencies agree with experiments to around 1% as shown in **Figure 3.6B**. The presence of the torsional soft-clamping mode is further proved by the ringdown measurement shown in **Figure 3.6D**, where the quality factor of the optimized mode at 133.6 kHz is measured to be 1.8 billion, which is in excellent agreement with the computational predictions (1.75 billion) and the highest mechanical quality factor yet measured in this frequency range at room temperature. Compared to the fundamental mode's Q_m, it has more than 60 times higher value. In this research, we simulated the Q_m considering the dissipation dilution but the acoustic radiation (Q_{rad})[16,20] and the loss from gas damping (Q_{gas})[25] can also affect the ringdown in the experiment. The excellent match between bending loss simulations and experimental results supports our hypothesis that bending loss is the dominant source of mechanical loss for the spiderweb nanomechanical resonator. While acoustic radiation loss (through the substrate) affects mechanical resonators with motion near the resonator-substrate boundary[16,17,20], it is expected to be negligible in our optimal design because the resonator motion is isolated from the substrate, with the support of the outer lateral beams, as described in **Figure 3.4**. At the same time, the gas damping effect can be ignored by performing the measurement under a sufficiently high vacuum of $4.0 \cdot 10^{-9}$ hPa. The high Q_m result is especially striking when considering the short length and larger thickness of the resonator than existing solutions in the literature, making it more practical to fabricate and operate. **Figure 3.6E** compares our result with the state-of-the-art nanomechanical resonator's experiment values at room temperature by plotting their Q_m, f_m, and their aspect-ratio t/L via marker area when t and L represent the thickness and the size of each reported resonator, respectively. It supports that our spiderweb resonator has obtained a high Q_m not using more challenging fabrication but considering novel vibration mode.

3.5. Conclusion

A simulation-based data-driven optimization approach was used to design a spiderweb nanomechanical resonator with ultralow dissipation in room-temperature environments. Our approach relies on the observation that spiderwebs have evolved over millions of years through evolutionary competition to be remarkable vibration sensors[29,30]. Using silicon nitride as a base material, our machine-learning algorithm hitchhikes on this natural optimization, and discovers nanomechanical designs tailored for high-precision sensors. While silicon nitride is one of the most widely used thin films for nanomechanical res-

onators, the design approach in this work could be extended to other materials such as diamond[69], gallium arsenide[65,70], silicon carbide[71,72], indium gallium phosphide[66,73], fused silica glass[74], silicon[75], phosphorus carbide[76,77], and even superconducting films[78,79]. The enhancement of the mechanical quality factor results from the discovery of a soft-clamping mechanism that uses a torsional motion to isolate a nanomechanical mode from ambient thermal noise. This enables high-Q_m nanomechanical resonators that have smaller aspect ratios than previous state-of-the-art designs, making them significantly easier, cheaper, and faster to manufacture. Our experimental validation demonstrates a new class of mechanical resonators that exhibit mechanical quality factors exceeding a billion in room temperature environments. This is achieved via a torsional soft-clamping mechanism that avoids radiation losses without using phononic crystals or submicrometer lithographic features. While other state-of-the-art resonators require tethers that are hundreds of nanometers in width, our resonators (with micrometer-sized features) can be reliably fabricated at large scales with photolithography. While high-Q_m resonators typically require $\sim 20 - 30$nm thicknesses, we design ours with 50 nm thickness to simplify the fabrication. Undoubtedly, by designing our resonators tethers with sub-micrometer tethers and thinner geometries, we could further improve Q_m at the cost of making the fabrication less accessible for general use. The low dissipation rate of the resonator, with $f_m/Q_m \approx 75$ μHz, also represents an important step toward high-precision sensing applications and room temperature quantum technologies. This includes quantum-limited force microscopy[5], "cavity-free" cooling scheme[80] and quantum control of motion at room temperature[81]. What is fascinating is that the machine-learning algorithm independently hones in on torsional vibration mechanisms, which are actually used by spiderwebs in nature when detecting prey, although the algorithm does not have any prior knowledge of how a spiderweb functions. Notwithstanding, we recognize that this data-driven exploration guided by machine learning is just a first step toward rational design of the next-generation of nanomechanical resonators. The demonstrated approach for realizing high-Q_m resonance modes is not restricted to the specific spiderweb-like design studied in this work. The design strategy might be applied to a wide range of geometries and design problems involving low-throughput simulations or experiments (the most common scenario in engineering and science). We expect future developments in machine learning and optimization together with novel fabrication techniques to lead to unprecedented nanotechnology within the next decade.

3.6. Experimental Section

Fabrication process: The nanomechanical resonators were fabricated from 58 nm-thick high-stress (1.07 GPa) Si_3N_4 deposited by LPCVD on a silicon substrate (**Figure 3.5A**). The disposition was carried out in-house, which allowed to obtain Si_3N_4 films of arbitrary thickness in stoichiometric form (3/4 ratio of silicon to nitrogen) leading to the uniform high tensile stress in the film. The pattern in the resonator was first written in a positive tone resist (AR-P 6200) by electron beam lithography (**Figure 3.5B**) to create a mask. To do so, the resist was spin coated on top of the Si_3N_4, baked at 155° C, exposed and developed in pentylacetate. Note that e-beam lithography was used instead of optical lithography

due to the high level of control and flexibility for the device geometry which was highly beneficial during the development of a new design. However, the minimum features of the resonators were designed to be 1 μm to ensure an easier, large-scale fabrication with optical lithography. The pattern was then transferred into the silicon nitride thin-film layer using an inductively coupled plasma (ICP) etching based on a CHF3 plasma etch (**Figure 3.5C**). Next, the resist was removed with dimethylformamide followed by two cleaning steps with hot piranha solution to remove organic residues and diluted hydrofluoric acid solution to remove surface oxides (**Figure 3.5D**). Last, the Si_3N_4 layer was released from the silicon substrate with an ICP etching with SF6 at -120° (**Figure 3.5E**)[82], performed at high pressure and low DC bias to etch isotropically the silicon substrate. This last step did not require any mask given the high selectivity of the chosen chemical against silicon nitride, avoiding any additional cleaning steps and removing any limitation posed by capillary force or stiction usually encountered in isotropic wet etchings (such as potassium hydroxide, KOH, or tetramethylammonium hydroxide, TMAH). Moreover, it was not constrained by the crystal planes of the silicon substrate, enabling the fabrication of arbitrary shapes and avoiding multiple exposures. The final thickness of the Si_3N_4 films was expected to be 50 nm.

Mechanical characterization setup: All the measurements presented were performed using a custom balanced homodyne detection interferometer (**Figure 3.5F**). The mechanical displacement was probed with a fiber coupled infrared laser (1550 nm). The power was divided into two arms: the local oscillator (90 %) used as interference reference and the signal arm (10 %) terminated with a lensed fiber. The signal arm and the device were mounted on two separate 3-axis nanopositioners placed perpendicular to each other, to align the device to the focal plane of the lensed fiber. In this way the signal which came out from the lensed fiber was focused on the device and its reflection was collected back inside the fiber. A piezoelectric plate was connected to the sample holder to actuate the devices mechanically. To reduce the effect of gas damping on the measurements, the lensed fiber and sample stage were placed inside a vacuum chamber. With the aid of a turbomolecular and a diaphragm pump, the system can reach a pressure of $4.0 \cdot 10^{-9}$ hPa. The sensitivity of the measured signal to phase oscillations was maximal in the linear region of the interference signal. To this end, the phase of the local oscillator signal was controlled with a fiber stretcher driven by a proportional integral derivative (PID) controller implemented with an FPGA board (RedPitaya 125-14) in order to stabilize the interferometer's low frequency fluctuations using the signal measured from the balanced photodetector as an error signal for a feedback loop. Thermomechanical noise spectra were acquired with an electronic spectrum analyzer without mechanical excitation applied to the piezoelectric plate. On the contrary, for the ringdown measurements, the device was first actuated close to the mechanical resonance frequency of interest with the piezoelectric plate until it reached an excited steady-state. Second, the mechanical actuation was turned off and the decay in time of the measured displacement signal was measured with an electronic spectrum analyzer by setting a resolution bandwidth larger than 5 Hz. The bandwidth needed to be larger than the expected linewidth of the resonator, but small enough to increase the signal-to-noise ratio.
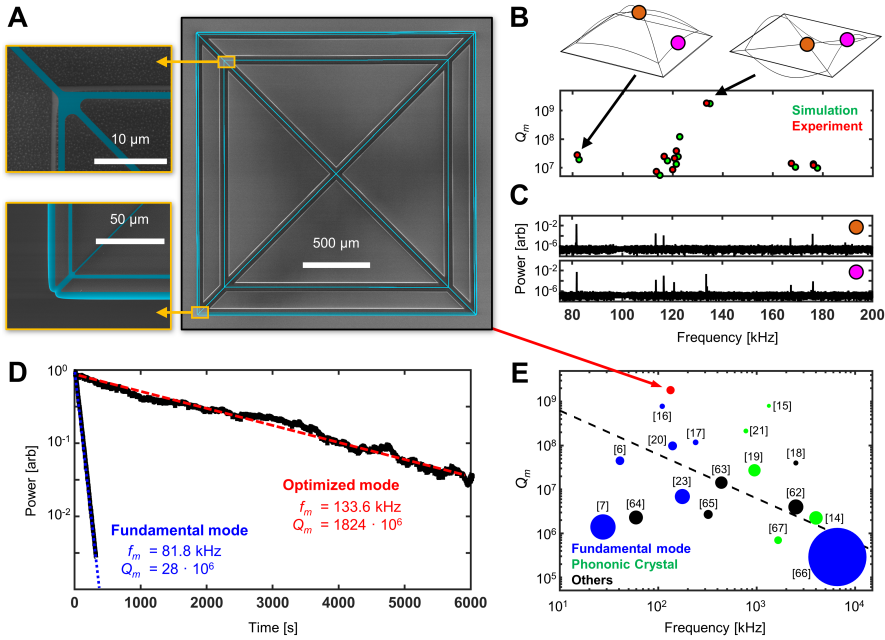
Fig. 3.6 Experimental characterization of the optimal spiderweb nanomechanical resonator. **A** False-colored scanning electron microscope images of the optimal design. **B** Q_m from the simulation and experimental results of the out-of-plane vibration modes with the figure of the fundamental and optimized mode shapes. **C** The thermomechanical noise spectra measured at the center of the resonator (orange marker) and the center of the inner lateral beam (pink marker). The y-axis is the normalized power with respect to the maximum power. **D** Ringdown measurement of the optimized 3 mm spiderweb resonator excited in its 133.6 kHz mode with an extracted quality factor higher than 1.8 billion, compared with the quality factor measured for the fundamental mode at 81.8 kHz. The y-axis is the normalized power with respect to the power at time=0 for each curve. **E** Comparison of the presented experiment result with state-of-the-art experiment reports[6,7,14−21,23,63−68]. Marker area corresponds to their aspect ratio t/L. The dashed line corresponds to the mechanical decoherence constraint in **Figure 3.1**

.

3

Supporting information
Lessons from string resonators

Generally, room temperature resonators with state-of-the-art quality factors have converged towards shared similarities in their geometry, material properties, and mechanical modes of interest. To date, they all exhibit some of the highest aspect ratios in microchip technology with free-standing structures nanometers thick but laterally suspended over several millimeters. As discussed in the main text, increasing the lateral size (L) of the resonator with respect to its thickness in the direction of motion (t) improves Q_m for beam and membrane nanomechanical resonators since generally $Q_m \propto L/t$. Another common attribute of all high Q_m resonators is the use of highly stretched silicon nitride (Si_3N_4) to fabricate these high-aspect-ratio nanostructures. A resonators' Q_m is defined as $2\pi W/\Delta W$ where W is the total stored energy of the resonator, and ΔW corresponds to the energy dissipated for each vibration cycle. Fabricating resonators from tensile materials enables extremely low mechanical dissipation (ΔW) while increasing the resonator's stored mechanical energy W as a consequence of geometric strain engineering[27]. The large initial stress before the vibration increases the potential energy dominantly, whereas the energy loss for each cycle is determined by the bending of the resonator's vibration mode. It means that the critical design parameters for the nanomechanical resonator's Q_m are the strain (stress) distribution after releasing the initial pre-stress and the vibration mode shape. The analytical formulation for a one-dimensional beam's bending f_m and the corresponding Q_m follows the equations below[23].

$$f_m = \frac{n}{2L}\sqrt{\frac{\sigma}{\rho}}\sqrt{1 + n^2\pi^2\lambda^2} \tag{3.S1}$$

$$Q_m \approx (2\lambda + \pi^2 n^2 \lambda^2)^{-1} Q_0 \tag{3.S2}$$

Q_0 is the intrinsic quality factor defined as $Q_0^{-1} = Q_{volume}^{-1} + Q_{surface}^{-1}$, where Q_{volume} is the bulk material loss of Si_3N_4 and $Q_{surface}$ is the surface loss, linear to the resonator's thickness. For thin resonators operating at room temperature, we assume $Q_0 \approx 6900\, t/100$ nm[48]. n, σ, ρ are bending mode number, initial stress, and density, respectively. λ is $\sqrt{E/12\sigma}t/L$ where E is the Young's modulus. Note that the dominant factor 2λ in eq. 3.S2 happens because of the sharp curvature change near the boundaries around a narrow length $L_c = \sqrt{2}L\lambda$[23], which reduces the quality factor dominantly. A similar formulation for the membrane structure could be found in[46]. **Figure 1** in the main text shows the Q_m versus vibration frequency (f_m) graph for a 50 nm thick 3 mm Si_3N_4 beam considering 1.07 GPa initial stress, when we vary the mode number. As it can be seen in it, the pre-stressed double clamped beam shows a significant improvement of Q_m compared to the unstressed beam's intrinsic quality factor Q_0. Also, the perfect soft-clamping assumption, which excludes the clamping loss part in eq. 3.S2, emphasizes the major loss of the quality factor from the sharp curvature change in the boundary, especially at lower order modes. Finally, all of these Si_3N_4 resonators have relied on mechanical modes which have the

highest amplitude of oscillation in the resonator center and where most of the induced losses come from how the mechanical mode connects to the microchip substrate where bending is highest. Given that the dominant channel of mechanical resonator loss comes from bending losses, until now most of the design strategies have typically consisted of engineering the decay of the resonator's mechanical mode to reduce bending in the Si_3N_4 resonators near the clamping points via hierarchical[16,22] structures or phononic crystal designs[14,15].

Derivation of the quality factor for two dimensional structures

The formulation here is the generalized form of the uniform membrane equations from Yu and co-workers[46]. Considering the out-of-plane deformation as the displacement field corresponding to the vibration mode shape, the strain can be derived from the generalized Euler-Bernoulli equation. Note that we calculate the strain assuming plane stress, constant deformation at the center of the plate u_z, as well as constant thickness. The oscillation of the plate $u_z(x, y)e^{i2\pi f_m t}$ induces strain in the plate due to bending and elongation during the vibration.

$$\begin{Bmatrix} \tilde{\epsilon}_{xx} \\ \tilde{\epsilon}_{yy} \\ 2\tilde{\epsilon}_{xy} \end{Bmatrix} = -ze^{2i\pi f_m t}\underbrace{\begin{Bmatrix} u_{z,xx} \\ u_{z,yy} \\ 2u_{z,xy} \end{Bmatrix}}_{bending} + \frac{e^{4i\pi f_m t}}{2}\underbrace{\begin{Bmatrix} u_{z,x}^2 \\ u_{z,y}^2 \\ 2u_{z,x}u_{z,y} \end{Bmatrix}}_{elongation} \tag{3.S3}$$

Then, the corresponding variation of stress is derived from generalized Hooke's law with the complex Young's modulus $\tilde{E}=E_1+iE_2$.

$$\begin{Bmatrix} \tilde{\sigma}_{xx} \\ \tilde{\sigma}_{yy} \\ \tilde{\sigma}_{xy} \end{Bmatrix} = \frac{\tilde{E}}{1-v^2}\begin{bmatrix} 1 & v & 0 \\ v & 1 & 0 \\ 0 & 0 & (1-v)/2 \end{bmatrix}\begin{Bmatrix} \tilde{\epsilon}_{xx} \\ \tilde{\epsilon}_{yy} \\ 2\tilde{\epsilon}_{xy} \end{Bmatrix} \tag{3.S4}$$

The mechanical work done per oscillation, which corresponds to the energy loss, can be derived as

$$\Delta U = \int_{Volume}\int_0^{1/f_m} \Re(\tilde{\sigma}_{xx})\Re(\tilde{\epsilon}_{xx,t}) + \Re(\tilde{\sigma}_{yy})\Re(\tilde{\epsilon}_{yy,t}) + 2\Re(\tilde{\sigma}_{xy})\Re(\tilde{\epsilon}_{xy,t})dtdV \tag{3.S5}$$

Inserting eq. 3.S3 and eq. 3.S4 into eq. 3.S5 and by ignoring the elongation term which is a few orders of magnitude lower than the other terms for the small deformation regime, eq. 3.S5 can be summarized as

$$\Delta U = \iiint \frac{\pi E_2}{1-v^2}((u_{z,xx} + u_{z,yy})^2 z^2 - 2(1-v)(u_{z,xx}u_{z,yy} - u_{z,xy}^2)z^2)dV$$

$$= \frac{\pi E_2 t^3}{12(1-v^2)}\iint (u_{z,xx}^2 + u_{z,yy}^2 + 2vu_{z,xx}u_{z,yy} + 2(1-v)u_{z,xy}^2)dS \tag{3.S6}$$

The system's stored energy can be obtained by calculating the maximum kinetic energy or the maximum elastic energy. Between the two, in this research, we considered the maximum elastic energy of the stretched structure due to bending and elongation. The

work done due to elongation happens to be a few orders of magnitude higher than the bending energy, so we ignore the bending energy here. Therefore,

$$
\begin{aligned}
U &= \iiint (\frac{1}{2}u_{z,x}^2\sigma_{xx} + \frac{1}{2}u_{z,y}^2\sigma_{yy} + u_{z,x}u_{z,y}\sigma_{xy})dV \\
&= \frac{t}{2}\iint (\sigma_{xx}u_{z,x}^2 + \sigma_{yy}u_{z,y}^2 + 2\sigma_{xy}u_{z,x}u_{z,y})dS
\end{aligned}
\tag{3.S7}
$$

From this result, we obtain $2\pi U/\Delta U$:

$$
Q_{\mathrm{m}} = \frac{12(1-v^2)}{E_2 t^2}\frac{\iint(\sigma_{xx}u_{z,x}^2 + \sigma_{yy}u_{z,y}^2 + 2\sigma_{xy}u_{z,x}u_{z,y})dS}{\iint(u_{z,xx}^2 + u_{z,yy}^2 + 2vu_{z,xx}u_{z,yy} + 2(1-v)u_{z,xy}^2)dS}
\tag{3.S8}
$$

Leading to eqs. (1)-(3) in the main text, when $Q_0=E/E_2$ considering $E_1 \gg E_2$.
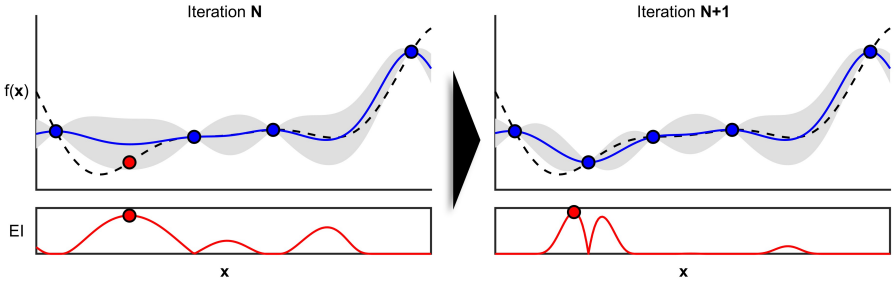
Bayesian optimization

Fig. 3.S1 An overview of Bayesian optimization with a one-dimensional minimization example. A Gaussian process regression model is fitted to the observed data (blue markers) and its acquisition function is maximized to select the design parameter (red markers) for the next iteration. The dotted black line corresponds to the unknown black-box function and the solid blue line corresponds to the regression result based on Gaussian process regression. The regression model is plotted as a posterior mean with shaded areas representing a 95 percent confidence interval.

Handling simulation-based optimization of spider web resonators requires the optimizer to use simulations with high computational cost. Bayesian optimization[55,58] is a global optimizer that is expected to avoid many local solutions associated with different modes of vibration. Using an online machine learning approach, this method performs optimization while updating limited information in the design space. If the response surface of Q_{m} is unknown, we can train the model with scarce information, starting with a few initial observations and adding additional feature evaluations sequentially. The goal is to optimize and track optimal design parameters using several evaluations of the finite element model of the spider web resonator. As shown in **Figure 3.S1**, Bayesian optimization uses Gaussian process regression (solid blue line) to approximate the unknown response of the function (dashed line) at each iteration. With the obtained data and the probability distribution taking into account the variance of the unmeasured region, the optimizer uses an acquisition function that determines the design variables for the next iteration. Here

we used Expected Improvement (EI) as the most commonly used acquisition function. It estimates where the most considerable improvement over the current best results will be so that both exploitation for local area search as well as the exploration for global optimization could be performed simultaneously. Compared to other optimization algorithms, additional computational resources are required to determine the next optimization point. However, when considering expensive function calls and small or medium design dimensions as in our study, they are negligible compared to the finite element simulation time. In this study, the Python library GPyOpt[59] was used. More detailed information about the method can be found at[58].

3

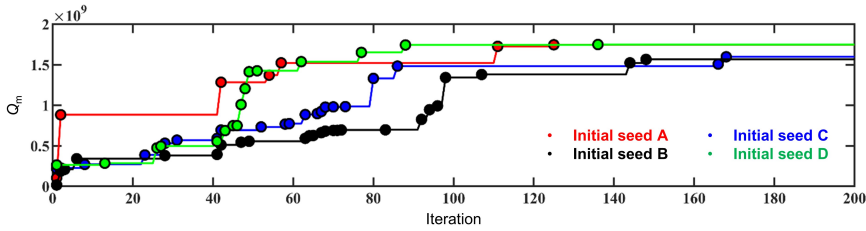## Optimization convergence dependency on the initial random points

Fig. 3.S2 Iteration history of the web-like nanomechanical resonator for optimizing Q_m with four different randomly selected initial points. The initial seed D is the result discussed in the main text.

The initial design of experiments affects the convergence to the optimum solution. Since our problem is dealing with global optimization, the curse of dimensionality is a crucial issue to be addressed. Even though we use Bayesian optimization to reduce the total number of design evaluations, the number of initial points (=40) is small compared to the design space (six design parameters). The result in **Figure 3.S2** shows the optimization history considering four different sets of randomly selected initial points. The figure shows that changing the initial points affects the convergence speed, as expected. However, the optimized design obtained for all four cases exhibits the same vibration mechanism described in the main text with a similar range of quality factors.

Table 3.S1 Optimal design parameters and the corresponding f_m, Q_m, and S_F for different initial random points.

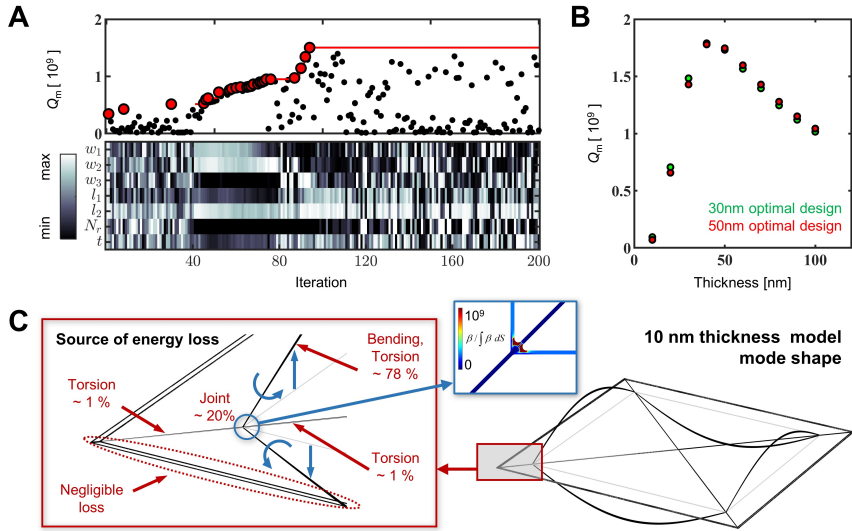| Design	N_r	d	w_1	w_2	l_1	l_2	f_m	Q_m	S_F)
		(μm)	(μm)	(μm)	(mm)	(mm)	(kHz)	$\cdot 10^9$	(aN/$\sqrt{\text{Hz}}$)
Initial seed A	4	1.01	1.00	2.00	1.14	1.48	141	1.75	2.1
Initial seed B	4	1.20	1.03	3.59	1.15	1.45	142	1.60	2.2
Initial seed C	4	1.16	1.11	3.30	1.09	1.46	145	1.56	2.3
Initial seed D	4	1.05	1.00	2.46	1.21	1.48	135	1.75	2.1

Fig. 3.S3 Overview of the thickness study for designing the spiderweb nanomechanical resonator. **A** Evolution of the quality factor Q_m and values of the seven design parameters at every iteration, including the thickness of the resonator. **B** Sweep of the thickness for two spiderweb nanomechanical resonators which are optimized for 30 nm and 50 nm, respectively. 50 nm design corresponds to the optimal result in **Figure 4** in the main text. **C** The full motion of the vibration mode shape and an illustration of the portion of energy loss of a 10 nm thickness spiderweb nanomechanical resonator. Other design parameters refer to **Table 1** in the main text.

Conversion of energy loss regarding the thickness of the web-like resonator

The optimization considering thickness as a design parameter has shown that minimizing the thickness was not giving the best quality factor, contrary to what is generally observed for straight strings (eq. 3.S2), or phononic crystal resonators[15]. **Figure 3.S3A** shows the optimization iteration history with the same conditions as the main text except considering the thickness as an additional design parameter. The optimized result converged at around 60 nm (local optimum), which differs from the general trend of minimizing the resonator thickness. To study more in details this effect, we performed two optimizations constraining the resonator thickness to 30 nm and 50 nm, respectively. Afterward, we swept the thickness of the two obtained designs from 10 nm to 100 nm. **Figure 3.S3B** shows the trend. As usual, the quality factor increases for thinner resonators when the thickness is larger than 50 nm. However, below 40 nm, it starts to decrease sharply. The reason of this effect can be understood from **Figure 3.S3C**, which shows the same design in the main text **Figure 4**, but modifying the thickness to 10 nm for comparison. As shown in the figure, most of the energy loss starts to focus on the lateral vibration beam, especially because the torsional motion of the lateral beam becomes significant. Furthermore, unlike the thicker designs, the joint region of the inner lateral beams starts to have a concentration of bending energy which starts to keep a large portion of energy loss because the sharp curvature change occurs, even though the soft-clamping mechanism isolates the resonator. Considering this motion, it is expected to improve the quality factor for thinner

resonators when considering more challenging fabrication with a width below 1 μm. Note that the research in the main text designed a 50 nm thickness spiderweb nanomechanical resonator considering our fabrication process.

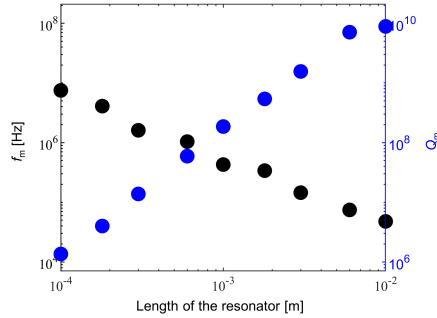## Mechanical quality factor of the web-like resonator regarding the resonator size

Fig. 3.S4 The mechanical quality factor and the vibration frequency for various sizes of optimized nanomechanical resonators.

The length of the mechanical resonator has been discussed as an essential factor for the f_m and Q_m. Following the trend of straight beams (eqs. 3.S1 and 3.S2), Q_m and $1/f_m$ is linear to L when $L \gg t$, and Q_m becomes quadratic to L if we assume perfect soft-clamping. To measure the length effects on the mechanical quality factor and the frequency of the spiderweb nanomechanical resonator, we optimized the quality factor of each design starting from 100 μm to 10 mm length of the resonator. Other design parameters and constraints were considered the same as in the main text. As shown in **Figure 3.S4**, increasing the resonator's length increased the quality factor quadratically, while the frequency was proportional to the inverse of the length. This result also supports that our new resonator follows the expected trend of the effect of soft-clamping. Since soft-clamping becomes more crucial for longer resonators, we expect to achieve a Q_m around 10 billion with a 1 cm web-like resonator.

Fundamental and center defect mode shape

To analyze the effect of the target mode shapes on the resulting Q_m, we performed two additional optimizations. The first (Design A) focuses on optimizing the Q_m of the fundamental vibration mode, while the second (Design B) aims to optimize the Q_m when the out-of-plane deformation at the center of the web is maximized. The optimal Design A, shown in **Figure 3.S5A**, exhibits a small d while pushing the outer lateral beam near the boundary with a large w_2. At the same time, the w_1 is nearly maximized with the inner lateral beam around the center of the resonator (see **Table 3.S2**). The result shows a similar strategy to the trampoline design presented in[20], using strain engineering. It maximizes the stress of the radial directional beam, which primarily vibrates in the fundamental mode by adding the mass around the center and the boundary. This suggests that the machine learning optimizer is capable of finding similar solutions to physics-based
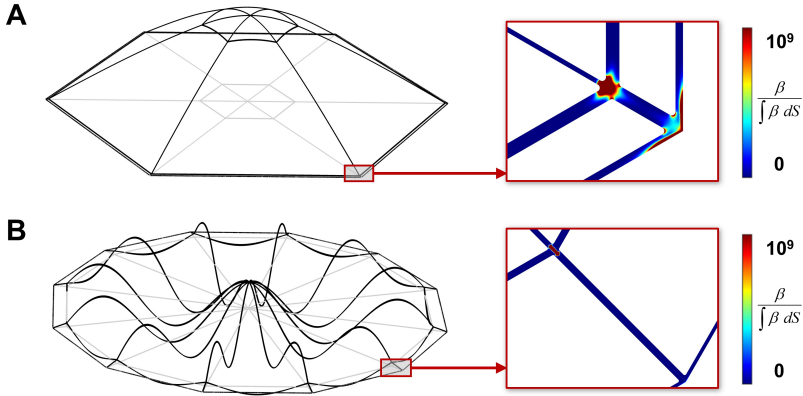
3

Fig. 3.S5 The optimal web-like soft-clamping mode for **A** Design A and **B** Design B obtained from simulation. The normalized bending loss density around the edge of Design A and Design B shows that the bending loss is concentrated on the boundary and the joints between the lateral and radial beams.

design approaches.

The optimal Design B increases the number of radial beams (see **Table 3.S2**), showing that we could achieve a higher Q_m at higher order modes, unlike uniform string[23] or membrane[46] resonators. The optimized result adds the lateral beams near the wave propagation node and couples the wave propagation in the radial direction to the lateral direction by the lateral beams' bending motion, as it can be seen in **Figure 3.S5B**. This demonstrates that the optimizer finds soft-clamping modes without any pre-information, by alternating the sharp curvature change near the boundary and distributing it to several joint deformations. Note that for both of the designs, the outer lateral beams distribute the bending loss concentrated at the boundaries, similarly to what was recently proposed by fractal[22] and hierarchical[16] soft-clamping.

Table 3.S2 Optimal design parameters and the corresponding f_m, Q_m, and S_F for Design A and Design B.

Design	N_r	d (μm)	w_1 (μm)	w_2 (μm)	l_1 (mm)	l_2 (mm)	f_m (kHz)	Q_m ($\cdot 10^6$)	S_F (aN/$\sqrt{\text{Hz}}$)
A	6	1.23	3.95	3.68	0.35	1.48	63.3	45.3	15.9
B	12	3.18	2.89	3.96	0.01	1.40	451.5	55.4	60.8

Evolution of the spiderweb nanomechanical resonators designs during the Bayesian optimization process

Figure 3.S6 shows an enlarged view of the design (black) and the vibrational modes (red) obtained at different iterations. The first two designs at iterations 26 and 27 are obtained

during the random search phase and the mode is localized in the outer later beam. The following designs at iterations 41 and 51 result from the Bayesian optimization phase and show a localized mode in the inner lateral beam. The last two designs at iterations 78 and 97 show a clear example of the Bayesian optimization *exploring*, resulting in vibration modes different from the previous iterations.

iter 26

iter 27

iter 41

iter 51

iter 78

iter 97
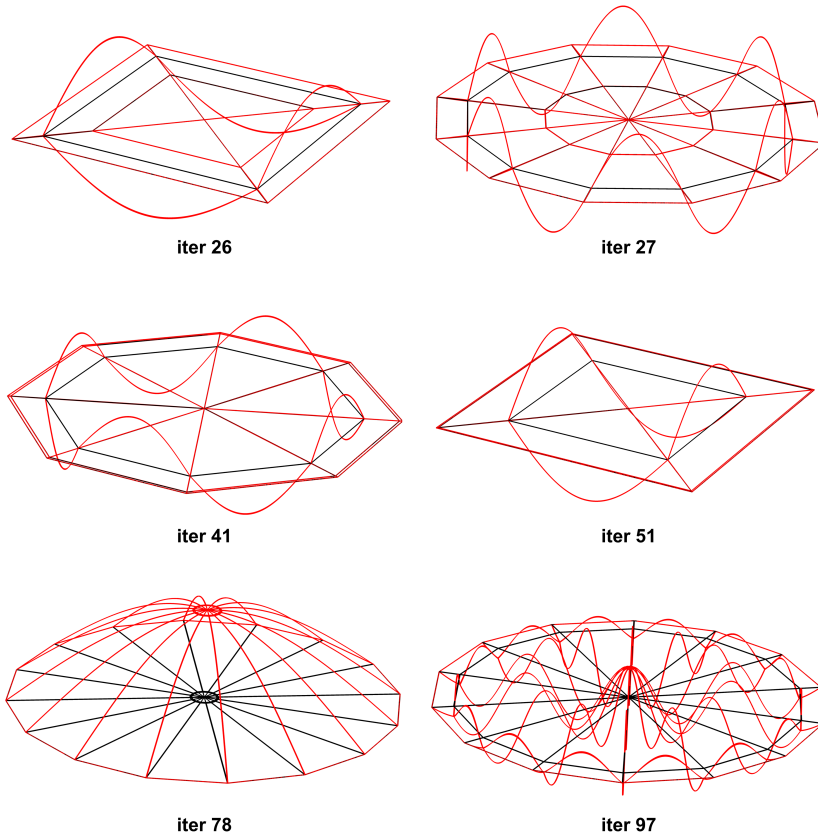
Fig. 3.S6 Design and simulated modes shapes at the iterations highlighted by circular markers in **Figure 3A** in the main text.

SEM from tilted view

The spiderweb nanomechanical resonator, fabricated in high stress silicon nitride, is suspended over the silicon substrate as shown in **Figure 3.S7**. The release step of the suspended nanomechanical resonator, highlighted in blue, is performed from the top, isotropically etching the silicon underneath. It follows that the fixed boundary is etched creating an overhang, as can be seen in the inset on the top right of **Figure 3.S7**.

3
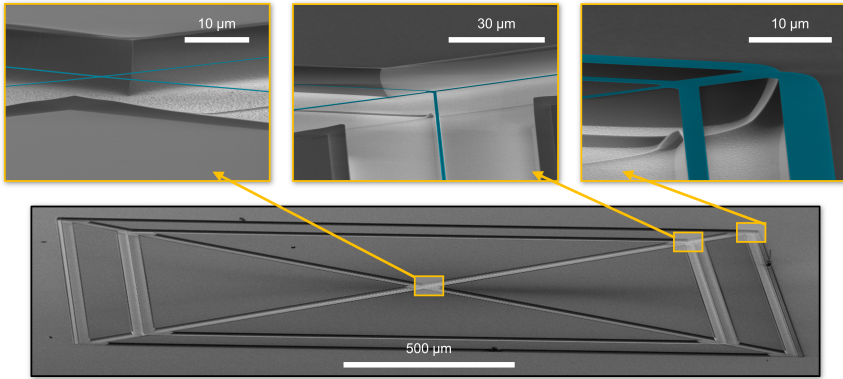
Fig. 3.S7 False colored scanning electron microscope images of the optimal design from tilted view. The 3 insets, from left to right, show a zoom at the center, at the joint, and at the clamping point.

Photothermal effect on Q factor
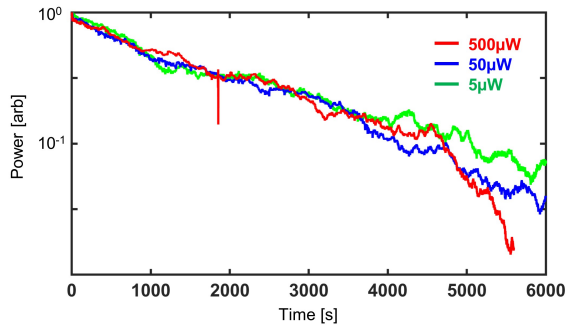
Fig. 3.S8 Ringdown measurement of the optimized 3 mm spiderweb nanomechanical resonator excited in its 133.6 kHz mode for three different laser powers. The y axis shows the power acquired from the spectrum analyzer in mW, normalized with respect to the power at time=0 for each curve.

The interaction between the nanomechanical resonator and the optical field can lead to photothermal effects, which in turn can mask the intrinsic damping rate of the oscillators. Those effects are proportional to the laser power. Therefore when measuring extreme high quality factors, it is important to ensure that the measured decay is not affected by the laser power. To verify it, we performed different ringdown measurements of the mechanical resonance at around 133.6 kHz of the spiderweb nanomechanical resonator shown in the main text in **Figure 6A**, by varying the laser power incident on the resonator from 500 μW to 5 μW. The result in **Figure 3.S8** shows a comparable decay rate for all the measurements, suggesting that photothermal effects are negligible. The plotted power on the y-axis is normalized with respect to the power at the beginning of the ringdown for each curve to provide a clear comparison. Note that the decaying envelope of the oscillation at carrier frequency is linear until the measured power equals the

nanomechanical resonator's thermal fluctuations level leading to large fluctuations of the measured signal. Moreover, strong fluctuations caused by unwanted temperature drifts and mechanical vibrations of the setup can bring the measured signal outside the linear region of the interference signal for a short interval of time, resulting in occasional spikes as visible in the curve acquired with a laser power equal to 500 μW at around 1800 seconds.

Finite element simulation model of the spiderweb design

Fig. 3.S9 COMSOL finite element simulation layout and mesh, corresponding to the iteration 27 model in the main text. **A** Top view of the finite element simulated structure showing the periodic condition along the blue l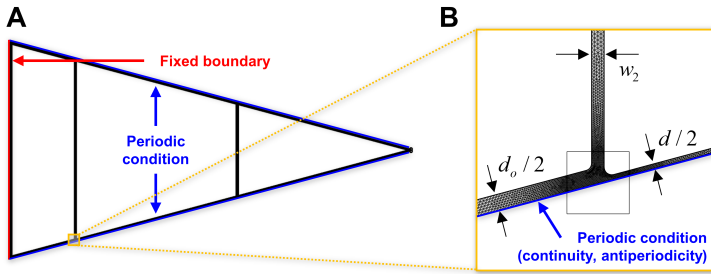ine with the fixed boundary condition along the red line. **B** Zoom-in of the yellow box region in **A**, showing the dense meshing of the spiderweb nanomechanical resonator with the denser mesh around the joint region.

As mentioned in the paper, the optimized result in this research was obtained from the finite element analysis performed by COMSOL[60]. We used plate elements for a two-dimensional structural mechanic simulation dealing with a pre-stressed eigenfrequency analysis, considering the thickness to the width ratio. The plate theory was based on the Mindlin theory with a linear elastic material model. To speed up the simulation, we simulated the partial part of the spiderweb resonator. **Figure 3.S9A** is an example of our iteration 27. The figure shows that it is modeling a portion of the resonator, which depends on N_r. The blue lines in the rotational directional edges considered continuity and antiperiodicity periodic conditions for the simulation, and the red line shows the fixed boundary condition. For each simulation, we considered initial in-plane forces ([N/m]) as 1.07 GPa · 50 nm, which is the product of the initial stress and the thickness. We performed the static analysis as the first step, including geometric nonlinearity because of the significant deformation happening from the static analysis[20]. Note that during the stationary analysis, it is always required to give the periodic condition for the periodic edges even if the antiperiodicity boundary condition is considered for the eigenvalue analysis. After performing the stationary analysis, we performed an eigenfrequency simulation, also including geometric nonlinearity. We have set up the maximum number of eigenfrequencies to be a hundred while setting the smallest real part as 100 Hz and the largest real part as 1 MHz. Concerning meshing, we divided the model with small squares around every joint to adjust a more fine mesh to consider the bending loss energy more precisely, as shown in **Figure 3.S9B** . To avoid numerical errors during the optimization, we meshed

the upper half of the structure and copied the mesh domain to the lower half of the structure. After the finite element simulation, we calculated the Q_m based on eq. 1 in the main text. After calculating Q_m of all the out-of-plane modes, we selected the maximized Q_m as the performance of the design.

3

References

1. Marquardt, F., Chen, J. P., Clerk, A. A. & Girvin, S. M. Quantum theory of cavity-assisted sideband cooling of mechanical motion. *Physical Review Letters* **99,** 93902 (2007) (cit. on p. 30).

2. Page, M. A., Goryachev, M., Miao, H., Chen, Y., Ma, Y., Mason, D., Rossi, M., Blair, C. D., Ju, L., Blair, D. G., Schliesser, A., Tobar, M. E. & Zhao, C. Gravitational wave detectors with broadband high frequency sensitivity. *Communications Physics* **4,** 1–8 (2021) (cit. on p. 30).

3. Metcalfe, M. Applications of cavity optomechanics. *Applied Physics Reviews* **1,** 31105 (2014) (cit. on p. 30).

4. Safavi-Naeini, A. H. & Painter, O. Proposal for an optomechanical traveling wave phonon-photon translator. *New Journal of Physics* **13,** 13017 (2011) (cit. on p. 30).

5. Hälg, D., Gisler, T., Tsaturyan, Y., Catalini, L., Grob, U., Krass, M. D., Héritier, M., Mattiat, H., Thamm, A. K., Schirhagl, R., Langman, E. C., Schliesser, A., Degen, C. L. & Eichler, A. Membrane-Based Scanning Force Microscopy. *Physical Review Applied* **15,** L021001 (2021) (cit. on pp. 30, 41).

6. Reinhardt, C., Müller, T., Bourassa, A. & Sankey, J. C. Ultralow-noise SiN trampoline resonators for sensing and optomechanics. *Physical Review X* **6,** 21001 (2016) (cit. on pp. 30, 32, 43).

7. Krause, A. G., Winger, M., Blasius, T. D., Lin, Q. & Painter, O. A high-resolution microchip optomechanical accelerometer. *Nature Photonics* **6,** 768–772 (2012) (cit. on pp. 30, 43).

8. Carney, D., Krnjaic, G., Moore, D. C., Regal, C. A., Afek, G., Bhave, S., Brubaker, B., Corbitt, T., Cripe, J., Crisosto, N., Geraci, A., Ghosh, S., Harris, J. G., Hook, A., Kolb, E. W., Kunjummen, J., Lang, R. F., Li, T., Lin, T., Liu, Z., Lykken, J., Magrini, L., Manley, J., Matsumoto, N., Monte, A., Monteiro, F., Purdy, T., Riedel, C. J., Singh, R., Singh, S., Sinha, K., Taylor, J. M., Qin, J., Wilson, D. J. & Zhao, Y. Mechanical quantum sensing in the search for dark matter. *Quantum Science and Technology* **6,** 24002 (2021) (cit. on p. 30).

9. Manley, J., Dey Chowdhury, M., Grin, D., Singh, S. & Wilson, D. Searching for Dark Matter with an Optomechanical Accelerometer. *2021 Conference on Lasers and Electro-Optics, CLEO 2021 - Proceedings* **126,** 61301 (2021) (cit. on p. 30).

10. Schmöle, J., Dragosits, M., Hepach, H. & Aspelmeyer, M. A micromechanical proof-of-principle experiment for measuring the gravitational force of milligram masses. *Classical and Quantum Gravity* **33,** 125031 (2016) (cit. on p. 30).

11. Miao, H., Martynov, D., Yang, H., Yang, H. & Datta, A. Quantum correlations of light mediated by gravity. *Physical Review A* **101,** 63804 (2020) (cit. on p. 30).

12. Chan, J., Alegre, T. P., Safavi-Naeini, A. H., Hill, J. T., Krause, A., Gröblacher, S., Aspelmeyer, M. & Painter, O. Laser cooling of a nanomechanical oscillator into its quantum ground state. *Nature* **478,** 89–92 (2011) (cit. on p. 30).

3

13. Delić, U., Reisenbauer, M., Dare, K., Grass, D., Vuletić, V., Kiesel, N. & Aspelmeyer, M. Cooling of a levitated nanoparticle to the motional quantum ground state. *Science* **367,** 892–895 (2020) (cit. on p. 30).

14. Ghadimi, A. H., Wilson, D. J. & Kippenberg, T. J. Radiation and Internal Loss Engineering of High-Stress Silicon Nitride Nanobeams. *Nano Letters* **17,** 3501–3505 (2017) (cit. on pp. 30, 38, 43, 45).

15. Engelsen, N. J., Ghadimi, A. H., Fedorov, S. A., Kippenberg, T. J., Bereyhi, M. J., Schilling, R. D. & Wilson, D. J. Elastic Strain Engineering for Ultralow Mechanical Dissipation. *International Conference on Optical MEMS and Nanophotonics* **2018-July,** 764–768 (2018) (cit. on pp. 30, 31, 38, 43, 45, 48).

16. Bereyhi, M. J., Beccari, A., Groth, R., Fedorov, S. A., Arabmoheghi, A., Kippenberg, T. J. & Engelsen, N. J. Hierarchical tensile structures with ultralow mechanical dissipation. *Nature Communications* **13,** 3097 (2022) (cit. on pp. 30, 32, 38, 40, 43, 45, 50).

17. Høj, D., Wang, F., Gao, W., Hoff, U. B., Sigmund, O. & Andersen, U. L. Ultra-coherent nanomechanical resonators based on inverse design. *Nature Communications* **12,** 5766 (2021) (cit. on pp. 30, 32, 40, 43).

18. Chakram, S., Patil, Y. S., Chang, L. & Vengalattore, M. Dissipation in ultrahigh quality factor SiN membrane resonators. *Physical Review Letters* **112,** 127201 (2013) (cit. on pp. 30, 43).

19. Guo, J., Norte, R. & Gröblacher, S. Feedback Cooling of a Room Temperature Mechanical Oscillator close to its Motional Ground State. *Physical Review Letters* **123,** 223602 (2019) (cit. on pp. 30, 31, 43).

20. Norte, R. A., Moura, J. P. & Gröblacher, S. Mechanical Resonators for Quantum Optomechanics Experiments at Room Temperature. *Physical Review Letters* **116.** 2016) (cit. on pp. 30–32, 40, 43, 49, 53).

21. Tsaturyan, Y., Barg, A., Polzik, E. S. & Schliesser, A. Ultracoherent nanomechanical resonators via soft clamping and dissipation dilution. *Nature Nanotechnology* **12,** 776–783 (2017) (cit. on pp. 30, 31, 43).

22. Fedorov, S. A., Beccari, A., Engelsen, N. J. & Kippenberg, T. J. Fractal-like Mechanical Resonators with a Soft-Clamped Fundamental Mode. *Physical Review Letters* **124,** 25502 (2020) (cit. on pp. 31, 32, 45, 50).

23. Schmid, S., Jensen, K. D., Nielsen, K. H. & Boisen, A. Damping mechanisms in high-Q micro and nanomechanical string resonators. *Physical Review B - Condensed Matter and Materials Physics* **84,** 165307 (2011) (cit. on pp. 30, 31, 38, 43, 44, 50).

24. Verbridge, S. S., Parpia, J. M., Reichenbach, R. B., Bellan, L. M. & Craighead, H. G. High quality factor resonance at room temperature with nanostrings under high tensile stress. *Journal of Applied Physics* **99,** 124304 (2006) (cit. on p. 31).

25. Schmid, S. & Hierold, C. Damping mechanisms of single-clamped and prestressed double-clamped resonant polymer microbeams. *Journal of Applied Physics* **104,** 93516 (2008) (cit. on pp. 31, 40).

26. Zwickl, B. M., Shanks, W. E., Jayich, A. M., Yang, C., Jayich, A. C., Thompson, J. D. & Harris, J. G. High quality mechanical and optical properties of commercial silicon nitride membranes. en. *Applied Physics Letters* **92,** 103125 (2008) (cit. on pp. 31, 37).

27. Fedorov, S. A., Engelsen, N. J., Ghadimi, A. H., Bereyhi, M. J., Schilling, R., Wilson, D. J. & Kippenberg, T. J. Generalized dissipation dilution in strained mechanical resonators. *Physical Review B* **99,** 54107 (2019) (cit. on pp. 31, 33, 38, 44).

28. Gao, W., Wang, F. & Sigmund, O. Systematic design of high-Q prestressed micro membrane resonators. *Computer Methods in Applied Mechanics and Engineering* **361,** 112692 (2020) (cit. on p. 32).

29. Cranford, S. W., Tarakanova, A., Pugno, N. M. & Buehler, M. J. Nonlinear material behaviour of spider silk yields robust webs. *Nature* **482,** 72–76 (2012) (cit. on pp. 32, 40).

30. Zaera, R., Soler, A. & Teus, J. Uncovering changes in spider orb-web topology owing to aerodynamic effects. *Journal of the Royal Society Interface* **11,** 20140484 (2014) (cit. on pp. 32, 40).

31. Jyoti, J., Kumar, A., Lakhani, P., Kumar, N. & Bhushan, B. Structural properties and their influence on the prey retention in the spider web. *Philosophical Transactions of the Royal Society A: Mathematical, Physical and Engineering Sciences* **377,** 20180271 (2019) (cit. on p. 32).

32. Fletcher, J. A. Spider webs and birds. *Emu* **23,** 284 (1923) (cit. on p. 32).

33. Gosline, J. M., Guerette, P. A., Ortlepp, C. S. & Savage, K. N. The mechanical design of spider silks: From fibroin sequence to mechanical function. *Journal of Experimental Biology* **202,** 3295–3303 (1999) (cit. on p. 32).

34. Boutry, C. & Blackledge, T. A. Biomechanical variation of silk links spinning plasticity to spider web function. *Zoology* **112,** 451–460 (2009) (cit. on p. 32).

35. Meyer, A., Pugno, N. M. & Cranford, S. W. Compliant threads maximize spider silk connection strength and toughness. *Journal of the Royal Society Interface* **11,** 20140561 (2014) (cit. on p. 32).

36. Masters, W. M. Vibrations in the orbwebs of Nuctenea sclopetaria (Araneidae) - I. Transmission through the web. *Behavioral Ecology and Sociobiology* **15,** 207–215 (1984) (cit. on p. 32).

37. Du, N., Yang, Z., Liu, X. Y., Li, Y. & Xu, H. Y. Structural origin of the strain-hardening of spider silk. *Advanced Functional Materials* **21,** 772–778 (2011) (cit. on p. 32).

38. BARROWS, W. M. the Reactions of an Orb-Weaving Spider, Epeira Sclopetaria Clerck, To Rhythmic Vibrations of Its Web. *The Biological Bulletin* **29,** 316–[332]–1 (1915) (cit. on p. 32).

39. Mortimer, B., Holland, C., Windmill, J. F. & Vollrath, F. Unpicking the signal thread of the sector web spider Zygiella x-notata. *Journal of the Royal Society Interface* **12,** 20150633 (2015) (cit. on p. 32).

40. Gao, H., Ji, B., Jäger, I. L., Arzt, E. & Fratzl, P. Materials become insensitive to flaws at nanoscale: Lessons from nature. *Proceedings of the National Academy of Sciences of the United States of America* **100,** 5597–5600 (2003) (cit. on p. 32).

3

41. Aizenberg, J., Weaver, J. C., Thanawala, M. S., Sundar, V. C., Morse, D. E. & Fratzl, P. Materials science: Skeleton of euplectella sp.: Structural hierarchy from the nanoscale to the macroscale. *Science* **309,** 275–278 (2005) (cit. on p. 32).

42. Kamat, S., Su, X., Ballarini, R. & Heuer, A. H. Structural basis for the fracture toughness of the shell of the conch Strombus gigas. *Nature* **405,** 1036–1040 (2000) (cit. on p. 32).

43. Miniaci, M., Krushynska, A., Movchan, A. B., Bosia, F. & Pugno, N. M. Spider web-inspired acoustic metamaterials. *Applied Physics Letters* **109,** 71905 (2016) (cit. on p. 32).

44. Krushynska, A. O., Bosia, F., Miniaci, M. & Pugno, N. M. Spider web-structured labyrinthine acoustic metamaterials for low-frequency sound control. *New Journal of Physics* **19,** 105001 (2017) (cit. on p. 32).

45. Liu, X., Liu, D., Lee, J. H., Zheng, Q., Du, X., Zhang, X., Xu, H., Wang, Z., Wu, Y., Shen, X., Cui, J., Mai, Y. W. & Kim, J. K. Spider-Web-Inspired Stretchable Graphene Woven Fabric for Highly Sensitive, Transparent, Wearable Strain Sensors. *ACS Applied Materials and Interfaces* **11,** 2282–2294 (2019) (cit. on p. 32).

46. Yu, P. L., Purdy, T. P. & Regal, C. A. Control of material damping in High-Q membrane microresonators. *Physical Review Letters* **108,** 83603 (2012) (cit. on pp. 33, 44, 45, 50).

47. Yasumura, K., Stowe, T., Chow, E., Pfafman, T., Kenny, T., Stipe, B. & Rugar, D. Quality Factors in Micron- and Submicron-Thick Cantilevers. *Journal of Microelectromechanical Systems* **9,** 117–125 (2000) (cit. on p. 34).

48. Villanueva, L. G. & Schmid, S. Evidence of surface loss as ubiquitous limiting damping mechanism in SiN micro- and nanomechanical resonators. *Physical Review Letters* **113,** 227201 (2014) (cit. on pp. 34, 44).

49. Gu, G. X., Chen, C. T., Richmond, D. J. & Buehler, M. J. Bioinspired hierarchical composite design using machine learning: Simulation, additive manufacturing, and experiment. *Materials Horizons* **5,** 939–945 (2018) (cit. on p. 34).

50. Carrasquilla, J. & Melko, R. G. Machine learning phases of matter. *Nature Physics* **13,** 431–434 (2017) (cit. on p. 34).

51. Jiao, P. & Alavi, A. H. Evolutionary computation for design and characterization of nanoscale metastructures. *Applied Materials Today* **21,** 100816 (2020) (cit. on p. 34).

52. Ding, Y., Kim, M., Kuindersma, S. & Walsh, C. J. Human-in-the-loop optimization of hip assistance with a soft exosuit during walking. *Science Robotics* **3,** eaar5438 (2018) (cit. on p. 34).

53. Shalloo, R. J., Dann, S. J., Gruse, J. N., Underwood, C. I., Antoine, A. F., Arran, C., Backhouse, M., Baird, C. D., Balcazar, M. D., Bourgeois, N., Cardarelli, J. A., Hatfield, P., Kang, J., Krushelnick, K., Mangles, S. P., Murphy, C. D., Lu, N., Osterhoff, J., Põder, K., Rajeev, P. P., Ridgers, C. P., Rozario, S., Selwood, M. P., Shahani, A. J., Symes, D. R., Thomas, A. G., Thornton, C., Najmudin, Z. & Streeter, M. J. Automation and control of laser wakefield accelerators using Bayesian optimization. *Nature Communications* **11,** 1–8 (2020) (cit. on p. 34).

54. Shields, B. J., Stevens, J., Li, J., Parasram, M., Damani, F., Alvarado, J. I., Janey, J. M., Adams, R. P. & Doyle, A. G. Bayesian reaction optimization as a tool for chemical synthesis. *Nature* **590,** 89–96 (2021) (cit. on p. 34).

55. Pelikan, M., Goldberg, D. E. & Cantú-Paz, E. BOA : The Bayesian Optimization Algorithm. *Proceedings of the genetic and evolutionary computation conference GECCO-99* **1,** 525–532 (1999) (cit. on pp. 34, 46).

56. Bessa, M. A., Glowacki, P. & Houlder, M. Bayesian Machine Learning in Metamaterial Design: Fragile Becomes Supercompressible. *Advanced Materials* **31,** 1904845 (2019) (cit. on p. 34).

57. Frazier, P. I. & Wang, J. *Bayesian optimization for materials design*, 45–75 (Springer, 2015) (cit. on p. 34).

58. Shahriari, B., Swersky, K., Wang, Z., Adams, R. P. & De Freitas, N. Taking the human out of the loop: A review of Bayesian optimization. *Proceedings of the IEEE* **104,** 148–175 (2016) (cit. on pp. 34, 46, 47).

59. Gonzalez, J. & Paleyes, A. *GPyOpt: A Bayesian Optimization framework in python*. `http://github.com/SheffieldML/GPyOpt`. 2022 (cit. on pp. 35, 47).

60. Inc., C. *COMSOL*. 2018 (cit. on pp. 35, 53).

61. Kawano, A. & Morassi, A. Detecting a prey in a spider ORB web. *SIAM Journal on Applied Mathematics* **79,** 2506–2529 (2019) (cit. on p. 36).

62. Steinlechner, J., Krüger, C., Martin, I. W., Bell, A., Hough, J., Kaufer, H., Rowan, S., Schnabel, R. & Steinlechner, S. Optical absorption of silicon nitride membranes at 1064 nm and at 1550 nm. *Physical Review D* **96,** 22007 (2017) (cit. on p. 37).

63. Wilson, D. J., Regal, C. A., Papp, S. B. & Kimble, H. J. Cavity optomechanics with stoichiometric SiN films. en. *Physical Review Letters* **103,** 207204 (2009) (cit. on p. 43).

64. Serra, E., Morana, B., Borrielli, A., Marin, F., Pandraud, G., Pontin, A., Prodi, G. A., Sarro, P. M. & Bonaldi, M. Silicon nitride MOMS oscillator for room temperature quantum optomechanics. *Journal of Microelectromechanical Systems* **27,** 1193–1203 (2018) (cit. on p. 43).

65. Naesby, A., Usami, K., Bagci, T., Melholt Nielsen, B., Liu, J., Stobbe, S., Lodahl, P. & Polzik, E. S. Optoelectronic cooling of mechanical modes in a semiconductor nanomembrane. *2011 Conference on Lasers and Electro-Optics Europe and 12th European Quantum Electronics Conference* **1,** 1–1 (2011) (cit. on pp. 41, 43).

66. Cole, G. D., Yu, P. L., Siquans, K., Moghadas Nia, R., Schmöle, J., Hoelscher-Obermaier, J., Purdy, T. P., Wieczorek, W., Regal, C. A. & Aspelmeyer, M. Tensile-strained InxGa1-xP membranes for cavity optomechanics. *Applied Physics Letters* **104,** 201908 (2014) (cit. on pp. 41, 43).

67. Faust, T., Krenn, P., Manus, S., Kotthaus, J. P. & Weig, E. M. Microwave cavity-enhanced transduction for plug and play nanomechanics at room temperature. *Nature Communications* **3,** 1–6 (2012) (cit. on p. 43).

68. Reetz, C., Fischer, R., Assumpção, G. G., McNally, D. P., Burns, P. S., Sankey, J. C. & Regal, C. A. Analysis of Membrane Phononic Crystals with Wide Band Gaps and Low-Mass Defects. *Physical Review Applied* **12,** 44027 (2019) (cit. on p. 43).

3

69. Nakamura, Y., Sakagami, S., Amamoto, Y. & Watanabe, Y. Measurement of internal stresses in CVD diamond films. *Thin Solid Films* **308-309,** 249–253 (1997) (cit. on p. 41).

70. Liu, J., Usami, K., Naesby, A., Bagci, T., Polzik, E. S., Lodahl, P. & Stobbe, S. High-Q optomechanical GaAs nanomembranes. *Applied Physics Letters* **99,** 243102 (2011) (cit. on p. 41).

71. Kermany, A. R., Brawley, G., Mishra, N., Sheridan, E., Bowen, W. P. & Iacopi, F. Microresonators with Q -factors over a million from highly stressed epitaxial silicon carbide on silicon. *Applied Physics Letters* **104,** 81901 (2014) (cit. on p. 41).

72. Romero, E., Valenzuela, V. M., Kermany, A. R., Sementilli, L., Iacopi, F. & Bowen, W. P. Engineering the Dissipation of Crystalline Micromechanical Resonators. *Physical Review Applied* **13,** 44007 (2020) (cit. on p. 41).

73. Bückle, M., Hauber, V. C., Cole, G. D., Gärtner, C., Zeimer, U., Grenzer, J. & Weig, E. M. Stress control of tensile-strained In1-xGaxP nanomechanical string resonators. *Applied Physics Letters* **113,** 201903 (2018) (cit. on p. 41).

74. Cumming, A. V., Sorazu, B., Daw, E., Hammond, G. D., Hough, J., Jones, R., Martin, I. W., Rowan, S., Strain, K. A. & Williams, D. Lowest observed surface and weld losses in fused silica fibres for gravitational wave detectors. *Classical and Quantum Gravity* **37,** 195019 (2020) (cit. on p. 41).

75. Beccari, A., Visani, D. A., Fedorov, S. A., Bereyhi, M. J., Boureau, V., Engelsen, N. J. & Kippenberg, T. J. Strained crystalline nanomechanical resonators with quality factors above 10 billion. *Nature Physics* **18,** 436–441 (2022) (cit. on p. 41).

76. Tan, W. C., Cai, Y., Ng, R. J., Huang, L., Feng, X., Zhang, G., Zhang, Y. W., Nijhuis, C. A., Liu, X. & Ang, K. W. Few-Layer Black Phosphorus Carbide Field-Effect Transistor via Carbon Doping. *Advanced Materials* **29,** 1700503 (2017) (cit. on p. 41).

77. Kistanov, A. A., Nikitenko, V. R. & Prezhdo, O. V. Point defects in two-dimensional γ-phosphorus carbide. *Journal of Physical Chemistry Letters* **12,** 620–626 (2021) (cit. on p. 41).

78. Read, D. T., Cheng, Y. W., Keller, R. R. & McColskey, J. D. Tensile properties of free-standing aluminum thin films. *Scripta Materialia* **45,** 583–589 (2001) (cit. on p. 41).

79. Nahar, M., Rocklein, N., Andreas, M., Funston, G. & Goodner, D. Stress modulation of titanium nitride thin films deposited using atomic layer deposition. *Journal of Vacuum Science & Technology A: Vacuum, Surfaces, and Films* **35,** 01B144 (2017) (cit. on p. 41).

80. Pluchar, C. M., Agrawal, A. R., Schenk, E. & Wilson, D. J. Towards cavity-free ground-state cooling of an acoustic-frequency silicon nitride membrane. *Applied Optics* **59,** G107 (2020) (cit. on p. 41).

81. Rossi, M., Mason, D., Chen, J., Tsaturyan, Y. & Schliesser, A. Measurement-based quantum control of mechanical motion. *Nature* **563,** 53–58 (2018) (cit. on p. 41).

82. Norte, R. A., Forsch, M., Wallucks, A., Marinković, I. & Gröblacher, S. Platform for Measurements of the Casimir Force between Two Superconductors. en. *Physical Review Letters* **121,** 030405 (2018) (cit. on p. 42).

4

Centimeter-scale nanomechanical resonators with low dissipation

High-aspect-ratio mechanical resonators are pivotal in precision sensing, from macroscopic gravitational wave detectors to nanoscale acoustics. However, fabrication challenges and high computational costs have limited the length of these devices, leaving a largely unexplored regime in nano-engineering. We present nanomechanical resonators that extend centimeters in length yet retain nanometer thickness. We explore this new design space using an optimization approach that leverages fast millimeter-scale simulations to inform and guide the more computationally intensive centimeter-scale design optimization. Our method of nanofabrication, by relying on a dry etching release, ensures a high-yield realization that experimentally confirms room temperature quality factors close to the numerical prediction. Finally, quality factors around 6.6 billion at kilohertz mechanical frequencies has been measured with the guide of machine learning. The synergistic integration of nanofabrication and design optimization, guided by machine learning, opens a solid-state approach to centimeter-scale nanomechanical resonators, with quality factors comparable to performance of leading cryogenic resonators and levitated nanospheres, even under significantly less stringent temperature and vacuum conditions.

4.1. Introduction

$\mathbf{M}$echanical resonators are crucial in precision sensing, enabling gravitational-wave observations at the macroscale[1,2], probing weak forces in atomic force microscopy at the nanoscale[3−7] or playing a central role in recent quantum technologies[8−10]. Their performance largely hinges on having low mechanical dissipation, quantified by the mechanical quality factor (Q). The Q factor measures both radiated acoustic energy and infiltrating thermomechanical noise, with a high Q pivotal in preserving resonator coherence. This is crucial, particularly at room temperature, for observing quantum phenomena[11,12], advancing quantum technology[13], and maximizing sensitivity for detecting changes in mass[14−16], force[17,18], and displacement[1]. High Q is often achieved through "dissipation dilution", a phenomenon originating from the synergistic effects of large tensile stress and high-aspect-ratio, observed both in resonators with macroscopic dimensions[2,19] and applied to resonators with nanometers thicknesses[20−22].

At the macroscale, a notable example is the pendulum formed by the mirror-suspension pair in gravitation wave detectors[23,24], where kilogram mirrors are suspended by wires tens of centimeters long and a thickness on the order of micrometers (Fig. 4.1b). The high tensile stress is created by the mirror masses, which induce stress in the wires due to gravity. The resulting high quality factor of the pendulum modes of the order of 10^8 allows isolating the detector from thermomechanical noise, enabling it to reach its enhanced displacement sensitivity. The exceptional acoustic isolation of these resonators has enabled landmark demonstrations of quantum effects at an unprecedented kilogram scale[25] and contributed to the first observations of gravitational waves[26]. Similar configurations at smaller scales are employed on table-top experiments to investigate the limits of quantum mechanics[27] and its interplay with gravity[28]. To date, resonators in this category, which span lengths of several centimeters, have been limited to micrometers minimum thicknesses.

At the nanoscale, resonators possess significantly reduced thickness, in the range of nanometers, with a length limited to millimeters. They are generally fabricated on top of a supporting substrate by standard silicon technology and integrated onto a single chip (Fig. 4.1a). High tensile stress, generated through a thermal mismatch between the resonator and the substrate, offers both lower mechanical dissipation and structural stability for long-distance suspended nanostructures. This necessitates careful material selection, with silicon nitride (Si_3N_4) emerging as one of the most common and easily manufacturable materials at room temperature in view of its advantageous mechanical and optical properties. Leveraging standard silicon technology compatibility, these nanomechanical resonators provide scalability[34], and integration[8] not found in their macroscale counterparts. Techniques like mode-shape engineering[29−31,35,36] and phononic crystal (PnC) engineering[32,33] have further enhanced dissipation dilution, pushing quality factors above 10^9. This improved coherence of motion has propelled advances in quantum phenomena exploration at cryogenic temperatures[37,38] and fostered a new sensor class development[39,40]. Generally, the quality factor in this class of resonators (Fig. 4.1d) is proportional to the length, and the resonance frequency is inversely proportional to the length[21,31]. Consequently, achieving a high quality factor at a low resonance frequency is constrained by the challenge of increasing the resonator's length beyond its current limitations.
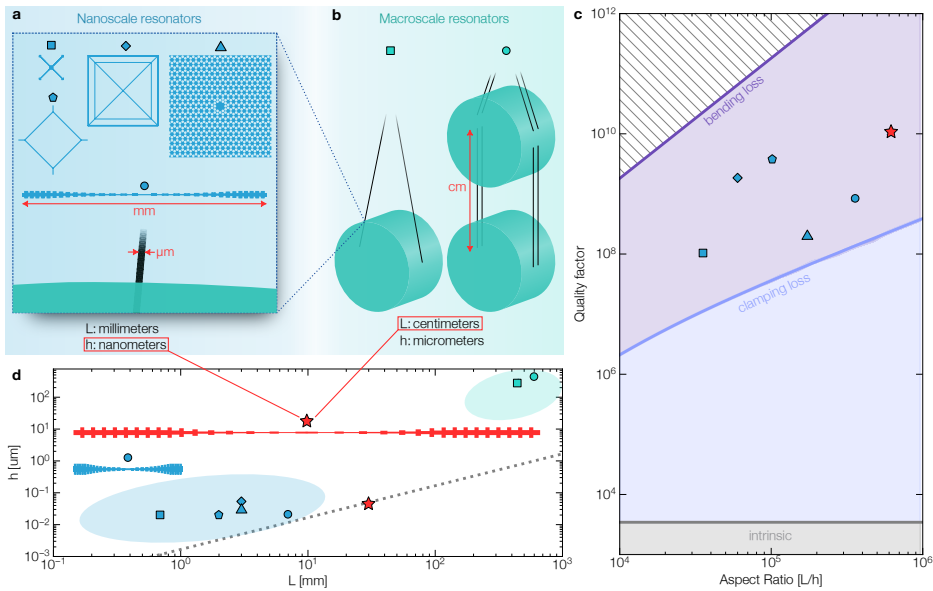
Fig. 4.1 High-aspect-ratio mechanical resonators. **a**, State-of-the-art Si_3N_4 nanomechanical resonators with nanometers thickness and length below 1 centimeter. On the left side: trampoline resonator[29] and perimeter resonator[30]. At the center: spiderweb resonator[31]. On the right side: soft-clamped membrane[32]. On the bottom: tapered string with phononic crystal[33] and a zoom-in of the LIGO suspension in **b**, scaled to match the dimension of all the nanomechanical resonators. **b**, Macromechanical resonators with micrometers thickness and extending into tens of centimeters. From left to right: LIGO suspension[24], advanced LIGO suspension[23]. **c**, Predicted quality factor as a function of the mechanical resonators aspect-ratio for a Si_3N_4 string. The blue points indicate the measured quality factor for the devices in **a**. The red stars show the predicted quality factor of the design demonstrated here. **d**, Thickness versus length of state-of-the-art mechanical resonators in **a** and **b**. The red star shows the design demonstrated here with its aspect-ratio indicated by the dotted black line.

Advancing these resonators to centimeter lengths while maintaining nanoscale thickness could both amplify dissipation dilution at room temperature and access an uncharted regime for on-chip nanomechanics, characterized by high quality factors, significant mass, and low resonance frequencies. The resulting resonators would feature the thicknesses and on-chip integration of nanomechanical devices, while extending in length above 1 cm, a dimension only archived in macroscopic devices, thereby giving rise to centimeter-scale nanomechanical resonators. This transition is not only of fundamental significance for investigating the dissipation limitations in nanomechanical resonators but also holds the potential for applications in ultrasensitive detection[41], including recently proposed searches for dark-matter[42]. By raising the Q factor to high values at low frequencies, on-chip mechanical ring-down times can be extended for hours or even days. This can be of importance for low-power time-keeping, allowing the mechanical resonator to operate for extended periods without an external power source. Moreover, the prospects of reaching quantum-limited motion regime at room temperature will extend the application range of quantum sensors[13], and offers prospects for quantum calibrated sensing[43]. Yet, pursuing such high-aspect-ratios at the envisioned centimeter scale faces considerable computational and fabrication barriers, including the need for a high fabrication yield to offset the limited number of devices per chip and cost implications, while mitigating the elevated computational cost of the design process. This challenge of cost-effective high-yield fabrication for centimeter-scale nanostructures introduces a unique dynamic between economics and design distinct from traditional high-volume nanotechnology.

We propose a novel approach that merges delicate fabrication techniques and multi-fidelity Bayesian optimization, enabling the creation of nanomechanical resonators with centimeter lengths and high-aspect-ratios exceeding 4.3×10^5; equivalent to reliably producing ceramic structures with a thickness of 1 millimeter, suspended over nearly half a kilometer. Our design strategy curtails optimization time while successfully circumventing common fabrication issues such as stiction, collapse and fracture. Applying our strategy to a 3 cm long silicon nitride string, we achieved a quality factor exceeding 6.5×10^9 at room temperature – surpassing the state-of-the art Q factor at room temperature by a factor of 2 for a mechanically clamped resonator. This solid-state platform performs on par with counterparts such as optically levitated nanospheres which require significantly more stringent vacuum conditions as low as 10^{-11} mbar[44] to reduce the collision rate between the particle and background gas molecules, typically the dominant source of dissipation. In contrast, our clamped centimeter-scale resonators are limited by intrinsic losses[20] and can approach comparable dissipation levels at pressures nearly two orders of magnitude higher. Notably, our room temperature resonators can also work at quality factors typically observed in cryogenic counterparts[45,46]. This enhanced capability to operate at higher temperatures and pressures unveils the potentials in centimeter-scale nanotechnology, expanding the boundaries of what is achievable with on-chip, room temperature resonators.

4.2. High-aspect-ratio advantage and multi-fidelity design

The quality factor of string resonators with a constant cross-section is given by[21]
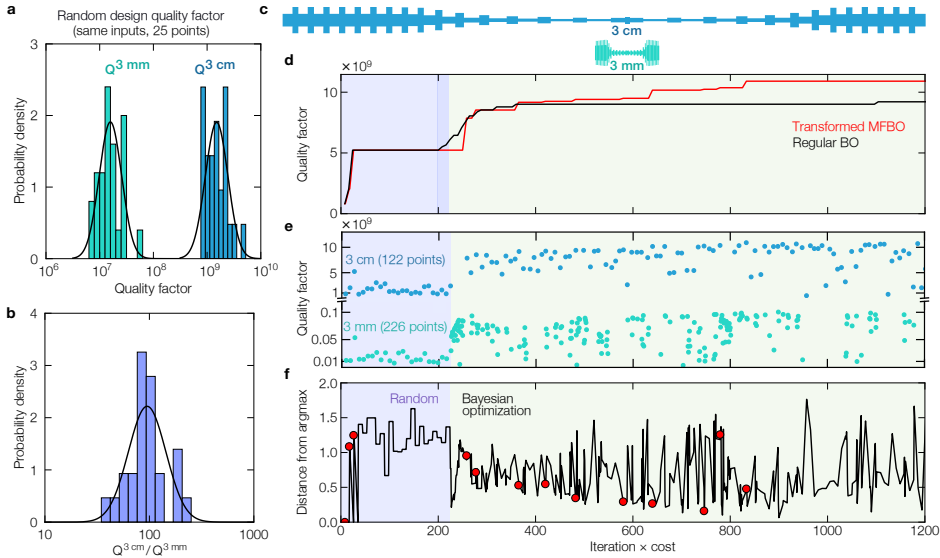
Fig. 4.2 Multi-fidelity Bayesian optimization a, Quality factor distribution for the two different lengths of PnC resonators (Blue: 3 cm, Green: 3 mm). 25 sets of design parameters were randomly selected, and both results followed a log-normal distribution. **b**, Probability distribution of the 3 cm and 3 mm resonator's quality factor ratio. The quality factor ratio follows a log-normal distribution. **c**, Shape of the optimized 3 cm (Blue) resonator and the corresponding 3 mm resonator (Green) indicating the length scale. **d**, Evolution of the optimized quality factor with two formulations. MFBO maximizing the log of the quality factor (Transformed MFBO) and single-fidelity Bayesian optimization maximizing the quality factor directly (Regular BO). Transformed MFBO outperformed regular BO. **e**, Iteration history of the transformed MFBO. After each of the 25 randomly selected high and low-fidelity simulations, the MFBO searches the following design parameters and the fidelity to simulate. Up to 1200 iteration costs, 122 high-fidelity points (cost 8), and 226 low-fidelity points (cost 1) were calculated. All the designs considered during the optimization can be found in the Supplementary Video[47]. **f**, The distance from a previous optimized point to the point considered in that iteration. The red markers indicate when the algorithm has found a higher quality factor until that iteration. **d** to **f** shares the same x-axis corresponding to the design iteration times the cost of each iteration as the optimization process evolves.

$$Q = Q_{int}\left[n^2\pi^2\frac{E}{12\sigma}\left(\frac{h}{L}\right)^2 + 2\sqrt{\frac{E}{12\sigma}}\left(\frac{h}{L}\right)\right]^{-1} \tag{4.1}$$

where Q_{int} is the intrinsic quality factor (surface loss) that varies linearly with the resonator's thickness, n is the mode order, E is the Young's modulus, σ is the initial stress, L and h are the resonator's length and thickness in the direction of motion, respectively. For given aspect-ratio h/L, the second term in the equation originates from the sharp curvature of the modeshape near the clamping points, where curvature is defined as the reciprocal of the radius of curvature (clamping loss), whereas the first term accounts for the curvature along the remainder of the resonator (bending loss) (Fig. 4.1c). The clamping loss occurs near the clamping region, defined as the part of the resonator at a distance of less than $L_c = \sqrt{E/6\sigma}h$ from the clamping points. We use the definitions for clamping and bending loss from[21].

In the high-aspect-ratio limit, the contribution of clamping loss is orders of magnitude larger, dominating the loss contribution. To this end, techniques known as soft clamping have been employed to reduce the sharp curvature at this L_c region[33] and improve the Q factor so that the Q factor scales quadratically with the aspect-ratio of the resonator. Those include phononic crystal-based string and membrane resonators, which employ a higher-order eigenmode confined in a central defect by the acoustic bandgap[32,33], spiderweb and perimeters resonators, which exploit low-order eigenmodes[30,31], or other methods considering the fundamental mode[29,35] (Fig. 4.1a). Note that Equation 4.1 is a straight beam formulation that does not directly apply to phononic crystal strings[48].

A high aspect-ratio is beneficial even if the Q factor is limited by the curvature at the clamping points (Equation 4.1). Hence, state-of-the-art high Q factor nanoresonators have advanced towards devices with increasing aspect-ratios, pushing the total length from micrometers[29,49] to millimeters[30–33] (Fig. 4.1c) alongside a thickness reduction below 50 nm. At the same time, the thickness dependent surface loss can offset the expected Q enhancement for thinner resonators and the Q factor can be increased primarily by increasing the total length while retaining the same aspect ratio.

Therefore, centimeter-long resonators maintaining a thickness within tens of nanometers can significantly raise the achievable quality factor. Meanwhile, nanomechanical resonators with higher aspect-ratios require advanced design strategies because high-fidelity simulation models capturing the resonator's behavior precisely require an increased computational cost. Unlike analytical derivations, where a higher aspect-ratio translates into a straightforward change of the numerical values for the calculation, numerical analyses necessitate additional degrees of freedom (DOFs) to describe the extreme aspect-ratio model, increasing the simulation time. For instance, finite element analysis of a centimeter-long string with phononic crystals takes roughly ten times more DOFs than the same geometry with one order lower aspect-ratio string when the thickness and width are the same. This challenges the centimeter-scale designs with limited computational cost, posing a boundary on the practical utility of numerical methods given the scarcity of high-fidelity data attainable. One optimization process took about 16 CPU-days for 150 iterations, which created a bottleneck in the design process. Here, multi-fidelity Bayesian optimization (MFBO)[50,51], alternates between employing both a quick, low-fidelity model for 3 mm resonators and a slower, high-fidelity model for 3 cm ones. The high-fidelity predictions

were eight times slower on average. To pursue a more generalized design approach for high-aspect-ratio resonators, here we consider numerical analysis by COMSOL[52] to maximize the quality factor instead of the specific analytical derivation for beam-like phononic crystals[48]. Note that analytical derivation for one-dimensional beams[48] has been studied, so that could be considered as the low-fidelity model for this specific case. However, we optimize with direct numerical simulations in this research to pursue a generalized approach for designing high-aspect-ratio resonators and to account for the localized effect from two-dimensional variations in the width direction without making specific assumptions. The geometry of both resonators[33] is parameterized (Supplementary Information Sec. I) to allow the presence of a PnC with a defect embedded in the center and chosen to practically allow the most number of on-chip resonators. The method then quickly explores the design space by fast evaluations of the smaller structures at higher frequencies (MHz), while establishing a correlation with the large devices at lower frequencies. This enables it to probe (slow) solutions for the high-aspect-ratio structures only on rare occasions when it expects the design to achieve a large quality factor.

The effectiveness of MFBO relies on the correlation between low and high-fidelity models and their respective evaluation times. If the low-fidelity model lacks correlation with the high-fidelity model, or if its evaluation time is comparable, the method loses effectiveness. By parameterizing the design space independently from resonator length (see Methods), we observed a reasonable correlation between the 3 mm (low-fidelity) and the 3 cm (high-fidelity) resonator designs (Fig. 4.2a). The results indicate that the Q factor of the 3 cm design was, on average, 100 times greater. This confirms the expected correlation between the two models according to the soft clamped Q factor in Equation 4.1. Nonetheless, the ratio has a fairly wide range of variation, indicating that the optimal design for a 3 mm resonator cannot be guaranteed to be the optimal design for the 3 cm case (Fig. 4.2b. Consequently, we applied MFBO to the log-normal Q factor, letting the algorithm selectively probe the design space via whichever fidelity it chooses. In essence, MFBO uses millimeter-scale simulations to guide centimeter-scale optimization.

The significant advantage of using multi-fidelity (transformed MFBO) Bayesian optimization, with respect to using single-fidelity (regular BO) Bayesian optimization is shown in Fig. 4.2d. Transformed MFBO outperforms regular BO by approximately 20% as it finds designs with Q exceeding 10 billion. Figure 4.2c depicts the optimized geometry. After determining the optimal design, we focused on fabricating this high-aspect-ratio device. The optimized geometry follows a tapering phononic crystal shape, which is similar to the result suggested by Ghadimi *et al.*[33] The optimal design maximized the width around the clamping region and narrowed down the width of the resonator coming near the center of the resonator. One distinguishing aspect of our approach was the consideration of the anti-symmetric mode rather than the symmetric mode. During the optimization under the design domain, the algorithm considered both symmetric and anti-symmetric modes, but the optimized mode was selected to be anti-symmetric. Because of this difference, the defect width was not minimized, unlike the early study[33], since the kinetic energy with significant movement is not maximized at the center. All the designs considered during the optimization can be found in the Supplementary Video[47]. Once the best design was found, we focused on addressing the challenges of fabricating a device with such an extreme-aspect-ratio.
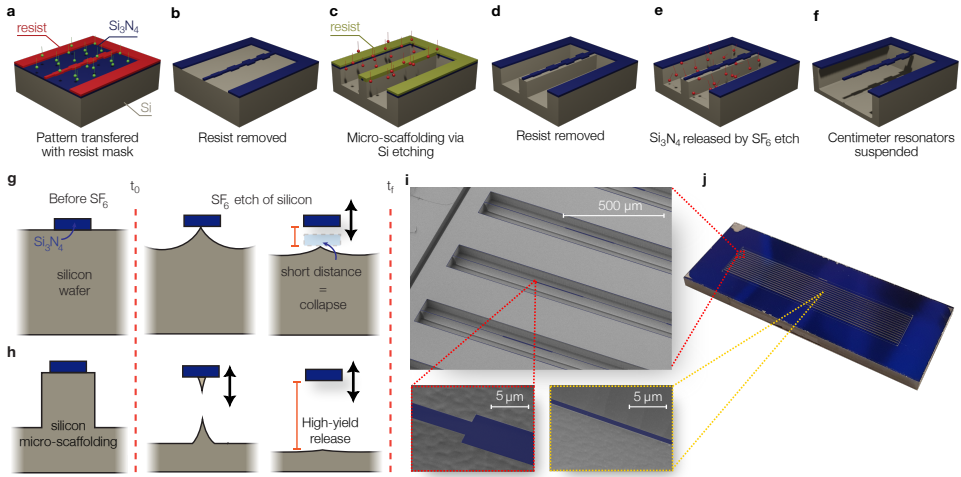
Fig. 4.3 Fabrication of centimeter-scale nanoresonators. **a-f** Schematic of the fabrication process composed of Si_3N_4 patterning via dry etching **a**, mask removal **b**, cryogenic DRIE silicon etching with photoresist mask **c**, mask removal **d**, Si_3N_4 undercut **e**, and Si_3N_4 suspended over a large gap **f**. **g**, SF_6 release step when the Si_3N_4 structure is suspended after being patterned, leading to collapse due to the short distance with the supporting silicon wafer. **h**, SF_6 release step with micro-scaffolding when the Si_3N_4 structure is suspended after a DRIE of the supporting silicon wafer, resulting in a large gap and high-yield release. **i**, False-colored scanning electron microscope pictures of the optimized 3 cm nanoresonators at the clamping area (top), at the boundary of the first unit cell (bottom-left), and at the center (bottom-right). The blue area indicates the area where Si_3N_4 is suspended, consisting of the string and the overhang. **j**, Photograph of a chip containing fourteen centimeter-scale nanoresonators, each 3 cm long.

4.3. Centimeter scale nanofabrication

Manufacturing centimeter-scale nanoresonators relies on fabrication intuition that shift from conventional nanotechnologies in design principles, fabrication methods, and cost considerations. In accordance with Moore's Law, conventional nanotechnology has focused on miniaturization across all three dimensions (x, y, z). However, centimeter-scale nanotechnology marks a transition that requires components expanding out to macroscopic lengths in x and/or y while retaining their nanoscale thickness. These nanostructures not only have high-aspect-ratios and centimeters length at the macroscale, but they are also patterned at the nanoscale with small feature sizes, providing them with enhanced functionalities (mechanical, optical, etc.). In particular, our nanostrings are not just elongated and thin; they also incorporate accurate patterned phononic bandgaps.

In contrast to conventional miniaturization, the size constraints of centimeter-scale nanoresonators permit far fewer devices per wafer, requiring high fabrication yields due to the resulting higher costs per device. Given their long geometries, any fracture of a centimeter-scale nanoresonator not only results in fewer successful devices but these broken devices can also collapse over several neighboring structures, escalating the implications of fabrication errors and low yield. Moreover, the fabrication of these high-aspect-

ratio structures requires them to be released with delicate nanofabrication techniques that do not exert any destructive forces during and after suspension. These processes must ensure that the high-aspect-ratio structures remain unfractured and undistorted, and are positioned safely away from nearby surfaces to prevent potential issues such as stiction due to attractive surface forces.

The schematic of the fabrication procedure is shown in Fig. 4.3a-f (see Methods). First, high-stress (1.07GPa) Si_3N_4 is deposited on a silicon wafer. A resist layer is spun on and lithographically patterned with an array of the 3 cm long optimized PnC resonators. This is achieved by employing multiple exposures with varying resolutions to reduce the exposure time without compromising the accuracy (Supporting Information Sec. C). This patterned resist is used as a mask to transfer the design into the Si_3N_4 film via directional plasma etch (Fig. 4.3a). Typically the most crucial step is the careful release of these fragile structures by removing the silicon beneath the Si_3N_4 resonator; with centimeter-scale nanostructures the requirements for successful suspension become much more stringent.

A critical aspect to realizing these nanostructures is the high stress within Si3N4 which not only contributes to achieving a high Q factor but also provides the required structural support and stability, allowing these taut strings to remain free-standing over remarkable distances without collapsing or sagging. In particular, we use dry SF_6 plasma etch to remove the silicon under the Si_3N_4 resonator (Fig. 4.3c-f) since it avoids the conventional stiction and collapse from surface tension present in liquid etchants[53] and it doesn't leave any residues. Once released, these 3 cm-long, 70 nm-thick structures can displace tens of micrometers due to handling and static charge build up, and potentially collapse onto nearby surface. In combination with the SF_6 plasma dry release, we first engineer a micro-scaffolding[33] (Fig. 4.3g,h) into the silicon underneath our Si_3N_4 that allows the free-standing structures to be suspended quickly, delicately, and far away from the substrate below, significantly increasing the yield and viability of this new type of nanotechnology (Supplementary Information Sec. E). The micro-scaffolding is lithographically defined by a second exposure and transferred into the silicon substrate via deep directional plasma etch (Fig. 4.3c). While our simulated strings are designed with a nominal thickness of 50 nm, the fabricated resonators have a larger final thickness from edge to center along their length. This is caused by the difficulty of dissipating heat during the etching step of the silicon substrate (Supplementary Information Sec. B).

Our choice to focus on 1D PnC nanostrings comes from a practical standpoint, which allows for packing numerous devices per chip (Fig 4.3i,j). By carefully engineering the delicate release of these structures, we achieved a fabrication yield as high as 93% on our best chip and 75% over all chips processed. While we only study 1D structures, the methodologies we developed are versatile and can be readily applied to more complex structures such as 2D phononic shields[32].

4.4. Low dissipation at room temperature

To assess the mechanical properties of the fabricated nanoresonators, we characterized the strings' out-of-plane displacements by a balanced homodyne optical interferometer (Fig. 4.4c) built to experimentally measure the 3 cm nanoresonators. The nanoresonator is placed inside an ultra-high vacuum (UHV) chamber at P < 10^{-9} mbar to avoid gas damping, increasingly dominant for high-aspect-ratio structures (see Supplementary Informa-
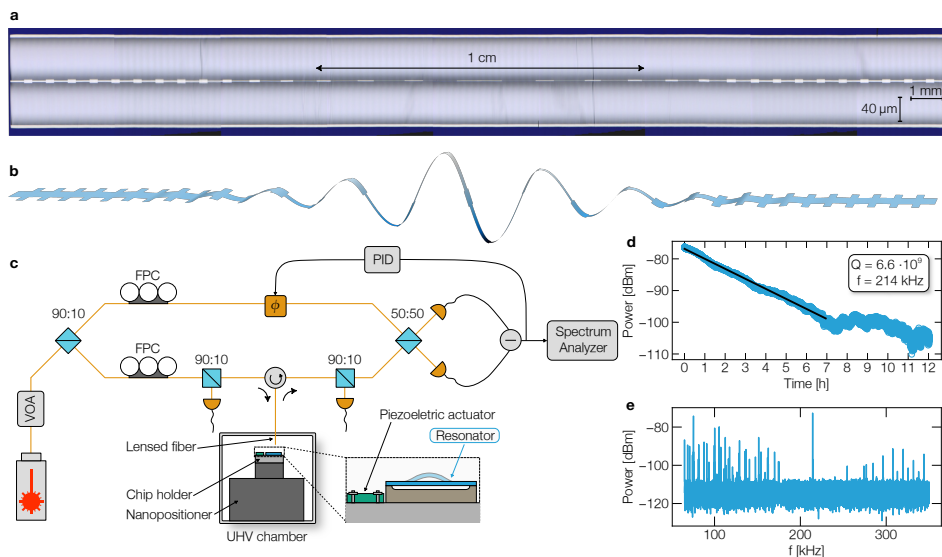
Fig. 4.4 Quality factor validation. **a**, Optical picture of the optimized 3 cm nanoresonators. For illustration purpose the picture is scaled along the vertical direction as indicated by the two scale bar. **b**, Mode shape of the eigenmode predicted to have high quality factor extracted from Finite Elements Analysis. **c**, Balanced homodyne optical interferometer built to experimentally measure the 3 cm nanoresonators. The nanoresonator is placed inside an ultra-high vacuum (UHV) chamber and mechanically excited by a piezoelectric actuator. Its motion is detected by an infrared laser via a lensed fiber. VOA, variable optical attenuator. FPC, fiber polarization controller. PID, proportional integral derivative controller. Φ, fiber stretcher. **d**, Ringdown trace of optimized nanoresonator excited at 214 kHz. The black solid line indicates the linear fitting corresponding to an extracted quality factor of 6.6 billion at room temperature. **e**, Thermomechanical noise spectrum.

tion Sec. A), and mechanically excited by a piezoelectric actuator. The resonator's motion is detected by an infrared laser via a lensed fiber. Figure 4.4e shows the displacement spectrum obtained from a location near the center of the string, under thermal excitation, for the device depicted in Fig. 4.4a. The spectrum shows a clear bandgap in frequency between 175 kHz and 255 kHz with one localized mode inside. The latter is observed at 214 kHz, in good agreement with simulation prediction. Figure 4.4b shows the predicted mode shapes obtained by finite element analysis for the eigenmode in the center of the bandgap. On the contrary, outside the 175 kHz - 255 kHz range, a plethora of modes are detected, whose displacement is distributed over the entire string length.

We experimentally evaluate the quality factor of the nanoresonators by applying a sinusoidal function to the piezoelectric actuator at a frequency near the eigenfrequency of the localized mode. Once the displacement at resonance reaches a plateau, the excitation is abruptly turned off to measure the ringdown of the mechanical mode. Figure 4.4d shows the envelope of the obtained signal for our best performing device, where the measured decay rate is proportional to the nanoresonator energy dissipation and thus its quality factor. As Fig. 4.4d shows, the localized mode at 214 kHz decays for over 7 hours. This corresponds to a Q factor of 6.6 billion at room temperature. To corroborate these findings, we tested additional lithographically identical devices, exhibiting the same frequency response in good agreement with the simulation, and quality factors within a 50 % range (Supplementary Information Sec. J).

While our simulations expect Qs of 10 billion, the fabricated centimeter scale nanomechanical structures have high-aspect-ratios that make it difficult to dissipate heat during the (exothermic) undercut process (Fig 4.3e), resulting in different Si_3N_4 etch rates. This gives the nanostructures slightly different thickness and dimension from edge to center along the beam, thus reducing the fidelity between design and experiment (Supplementary Information Sec. B).

4.5. Conclusion

We demonstrated centimetre-scale nanomechanical resonators with aspect-ratio above 4.3×10^5. Our approach combines two features. First, using MFBO we are able to reduce the simulation cost while maintaining the required accuracy to precisely capture the resonator's behaviour. The resulting data-driven design process allows to optimize PnC strings obtaining soft-clamped modes which eliminate clamping losses and radiation to the substrate. Second, a dry etching technique that overcomes limitations such as stiction and collapse enables to reliably realize the optimized designs on-chip. The fabricated PnC strings extend for 3 cm in length maintaining nanometers thickness and a minimum width of 500 nm. With a Q of 6.6 billion at a frequency of 214 kHz, we experimentally achieve the lowest dissipation yet measured for clamped resonators at room temperature.

The obtained aspect-ratio enables not only to achieve a two-fold improvement of the quality factor in room temperature environments, but it also leads to low resonance frequencies and large spacing between nearby mechanical modes. Those features translate into coherence time $t_{coh} = \hbar Q/(k_B T)$ approaching 1 ms and thermomechanical-limited force sensitivity of $\sqrt{4 k_B T \omega_m m / Q} \sim$ aN/$\sqrt{\text{Hz}}$.

A natural application is ground state cooling of the mechanical resonators in a room-

temperature environment. The high coherence time enables these resonators to undergo more than $Q\omega_m(\hbar/K_B T) \approx 200$ coherent oscillations in the ground state before a thermal phonon enters the system[54]. The small thermal decoherence rate $\Gamma_{th} = k_B T/(\hbar Q)$ of a few Hz allows to resolve the zero point fluctuations $x_{zp} = \sqrt{\hbar/(2m\omega_m)}$ with a displacement imprecision $S_{xx}^{imp} = 4x_{zp}^2/\Gamma_{th}$ below 1×10^{-15} m/$\sqrt{\text{Hz}}$, on pair with the imprecision limit due to shot noise achievable in conventional interferometer setup. This makes centimeter-scale nanoresonators particularly promising for the cavity-free cooling scheme[55]. The developed resonators are also ideal candidates for creating high-precision sensors, specifically force detectors[18], and hold promise for obtaining frequency stability on pair with state-of-the-art clocks[56–58]. Conservatively assuming sub-micrometers amplitude displacements in the linear regime, we can extrapolate a thermomechanical limited Allan deviation[57] $\sigma_y(\tau) \sim 3 \times 10^{-12}/\sqrt{\tau}$ for $m_{\text{eff}} = 4.96 \times 10^{-13}$ Kg.

Remarkably, the degree of acoustic isolation (quantified by the quality factor) we can achieve on a solid-state microchip is similar to values recently demonstrated for levitated nanoparticles operating at vacuum pressure levels more than two orders of magnitude lower than our resonators[44,59]. This is particularly striking if one considers that levitated particles do not have any physical connection with the environment except for the small coupling to any gas molecules still present at vacuums levels as low as 10^{-11} mbar. On the contrary, our solid-state resonators are physically clamped to a room temperature chip, surrounded by 100 times higher gas pressures and exhibit comparable acoustic dissipation.

The ability to combine macromechanics with nanomechanics offers unique possibilities to integrate the versatility of on-chip technology with the detection sensitivity of macroscale resonators. Notably, the only foreseeable limitation to producing even longer, higher-Q devices is that larger undercuts distance must be engineered, and practically going to longer, lower-frequency devices would require increasingly higher vacuum levels; this makes centimeter-scale nanotechnology particularly interesting for next-generation space applications[60,61] which inherently operate at pressures below 10^{-9} mbar. Pushing the boundaries of fabrication capabilities with higher selectivity materials[45,62,63] would extend our current approach to more extreme-aspect-ratios and investigate new physics. These include the exploration of weak forces such as ultralight dark matter[42] and the investigation of gravitational effects at the nanoscale[64,65]. By blurring the line between macroscopic and nanoscale objects, these centimeter-scale nanomechanical systems challenge our conventional intuitions about fabrication, costs, and computer design and promise to give us novel capabilities which have not been available at smaller scales.

4.6. Methods

Computational experiments and design. The design approach for high-aspect-ratio resonators was based on numerical analysis with COMSOL[52]. The quality factor was maximized via multi-fidelity Bayesian optimization without recurring to the analytical solution derived for beam-like Phononic Crystals (PnCs)[48]. In particular, we consider the trace-aware knowledge gradient (taKG) formulation of Bayesian optimization with two fidelities[66]. Detailed information about the formulation can be found in Supplementary Information Sec. G. The maximization based on the high-fidelity model becomes possible

by learning the trend (surrogate model) from multiple low-fidelity predictions instead of using fewer high-fidelity evaluations. The approach is especially beneficial for cases when the difference in time evaluation between fidelities is significant, i.e., the time it takes to perform one function evaluation (one design prediction via COMSOL) for the high fidelity is much longer than for the lower fidelity.

We considered a 3 cm resonator as the high-fidelity model and a 3 mm resonator as the low-fidelity model for the MFBO. As mentioned in the main text, we expected them to be correlated, given that $Q \propto L^2$ (Equation 4.1) for the string type resonators neglecting the sharp curvature change around the clamping region using the PnC. This correlation allows us to predict the response of the 3 cm computationally expensive model by the 3 mm relatively cheap model. For the centimeter-scale PnC resonator's quality factor maximization, we designed the resonator's geometry with a two-dimensional model. The model has nine design parameters, including five determining the resonator's overall shape, the unit cell's width and length ratio, and the defect's length and width. Design variables were set to be independent of the resonator length. Detailed parameter descriptions can be found in Supplementary Information Sec. I.

Figure 4.2a shows the quality factor distribution obtained from randomly selected 25 high-fidelity PnC resonator designs and the same number for low-fidelity ones. For both lengths, the same design parameters are considered. Both length scale's quality factor follows a log-normal distribution. More importantly, the ratio between the two fidelities also follows a log-normal distribution as depicted in the histogram in Fig. 4.2b. The result indicates that the Q factor of the 3 cm design is, on average a hundred times larger than that of the same design scaled down to 3 mm, which confirms the expected correlation between the two models. Nevertheless, the ratio shows significant variance, ensuring that the optimum design for the 3 mm resonator does not precisely correspond to the best design for the 3 cm case. These findings underscore that using MFBO with low- and high-fidelity simulation models leads to a balance between obtaining the required accuracy and minimizing the simulation cost.

Figures 4.2d-f show the optimization iteration history considering that the high-fidelity simulation costs eight times more than the low-fidelity simulation. This average time difference between fidelities is determined from the first designs obtained by random search. Figure 4.2d compares the results when the logarithm of the quality factor is considered for the maximization using multi-fidelity Bayesian optimization (transformed MFBO) and when single-fidelity Bayesian optimization is directly optimizing the quality factor (regular BO). After starting with 25 randomly selected initial calculations for the 3 cm and 3 mm model (or only the 3 cm model for the regular BO), the algorithm maximizes the quality factor for the 3 cm model by searching for the best possible design parameters. We note that the initial random design of experiments affects the optimization performance, but in most cases, MFBO outperformed single-fidelity Bayesian optimization. The results with different random initials comparing the transformed MFBO and regular BO are summarized in Supplementary Information Sec. H.

Detailed information on the transformed MFBO is shown in Figs. 4.2e and f. Figure 4.2e illustrates the quality factor calculated for each fidelity, and Fig. 4.2f illustrates the distance from a previous optimized point to the point considered in that iteration. Right after the random search, the algorithm runs predominantly low-fidelity simulations to

optimize the quality factor, taking advantage of the relatively cheap simulation cost. We note that the low-fidelity simulation has higher quality factor variance when compared to the high-fidelity simulations, given the larger number of designs being explored in the former vs. the latter. The high values in the distance from the argmax plot (Fig. 4.2f) further confirm this by showing that the optimization is found not only by exploitation but also by exploration. For example, the exploration phase improves the quality factor as observed at iteration × cost ~ 800.

Nanofabrication for centimeter-scale phononic crystal resonators. The 3 cm optimum design is fabricated on high stress silicon nitride (Si_3N_4), deposited by low-pressure chemical vapor deposition (LPCVD) on 2 mm silicon wafers. The fabrication starts by transferring the desired geometry on a thin positive tone resist (AR-P 6200) by a lithographic step. Typically, electron beam lithography or photolithography is used to pattern the masking layer. Electron beam lithography allows higher resolution and smaller features size compared to the optical counterpart, but it is prone to stitching errors for structures exceeding the writing field[67]. With each writing field extending for 100 μm - 1 mm, our centimeter-resonators require more than 30 fields, leading to noticeable stitching errors. We then implemented an overlap between adjacent writing fields of 100 nm and controlled the dose at specific locations (more details can be found in Supplementary Information Sec. C). This resulted in an accurate transfer of the desired geometry avoiding the presence of stitching errors. Despite the electron beam lithography superior resolution, photolithography is preferable for a fast and cost-effective manufacture at the large scale. With this in mind, we constrained the minimum feature size of the nanoresonators at 500 nm, compatible with ultraviolet photolithography.

Next, the pattern is transferred to the Si_3N_4 layer using an inductively coupled plasma (ICP) etching process (CHF_3 + O_2) at room temperature (Fig. 4.3a) before removing the masking layer (Fig. 4.3b).

The most critical part of the process is then suspending the high-aspect-ratio fragile structures over the substrate without causing any fracture, stiction or collapse. Typically this step is performed by liquid etchants such as KOH which selectively removes the silicon substrate. However, turbulences and surface-tension forces can lead to collapse destroying the suspended structures[53]. Those forces depend on the surface area of the nanoresonators and thus increase with the aspect-ratio, drastically reducing the fabrication yield for centimeter-scale nanoresonators. To overcome those limitations, stiction-free dry release can be employed[31,68,69], where the silicon substrate is isotropically removed by plasma etching. Fluorine based (SF_6) dry etching at cryogenic temperature is particularly suited in view of its high selectivity against Si_3N_4, for which it does not require any mask or additional cleaning steps. Nevertheless, geometries with extreme high-aspect-ratio require a large opening ($> 50 \mu m$) from the substrate to avoid attraction due to charging effects, not achievable by SF_6 plasma etching alone.

To this end, we first directionally etch the silicon substrate by employing a thick positive tone photoresist (S1813) as a proactive layer (Fig. 4.3c). The step is carried out with cryogenic deep reactive ion etching (DRIE) using SF_6 + O_2 plasma[70]. Cryogenic DRIE allows to control the opening size from the substrate without affecting the Si_3N_4 film quality. However, photoresist is vulnerable to cracking in cryogenic DRIE[71]. To circum-

vent this limitation, the centimeter scale nanoresonators are shielded by an outer ring, which stops the cracks and prevents them from reaching the nanoresonators (see Supplementary Information Sec. D for details). The photoresist is then stripped off (Fig. 4.3d) and a hot piranha solution consisting of sulfuric acid and hydrogen peroxide is employed to remove residual contaminants on the surface. After that, hydrofluoric acid solution allows to remove oxides from the surface, which would otherwise prevent an even release of nanoresonators. Finally, the centimeter scale nanoresonators are suspended by a short 32 seconds fluorine-based (SF6) dry etching step (Fig. 4.3e-f) performed at $-120\,°C$. The process isotropically etches the silicon substrate employing a pressure of 10 mbar, an ICP power of 2000 W and a gas flow of 500 sccm, while the RF power is set to 0 W.

The developed process enables to achieve a fabrication yield as high as 93 % for our best chip, while the average value among all the fabricated devices is 75 %. The main limiting factor is ensuring a particle-free surface prior to the SF_6.

UHV Lensed-fiber Optical Setup. To assess the mechanical properties of the fabricated nanoresonators, we characterized the strings' out-of-plane displacements by a laser interferometer (Fig. 4.4c). In it, 10% of the laser power of a 1550 nm infrared laser is focused on the nanoresonator. The reflected signal is collected by a lensed fiber to interfere with the local oscillator (LO) signal consisting of the remaining 90% of the infrared laser. The output signal, proportional to the resonator's displacement, is read out by an electronic spectrum analyzer after being converted by a balanced photodetector. The same output signal acts as an error function for the feedback loop employed to stabilize the phase of the setup against slow fluctuations caused by mechanical and thermal drift. The feedback loop is implemented with a PID controller, which adjusts the phase of the LO signal.

To avoid gas damping, increasingly dominant for high-aspect-ratio structures (see Supplementary Information Sec. A for details), the nanoresonator is placed inside an ultra high vacuum chamber capable of reaching $P < 1 \times 10^{-9}$ mbar. The vacuum chamber is equipped with a 3-axis nanopositioner which allows to align the device with respect to the lensed fiber.

The chip is placed near a piezoelectric actuator which can vibrate out-of-plane. The latter allows to mechanically excite specific resonance frequencies of the nanoresonators. We then experimentally evaluate the quality factor of the nanoresonators by applying a sinusoidal function to the piezoelectric actuator at a frequency near the eigenfrequency of the localized mode. Once the displacement at resonance reaches a plateau, the excitation is abruptly turned off to measure the ringdown of the mechanical mode.

The power of the infrared laser can be manually adjusted by a variable optical attenuator, enabling to vary the laser power incident on the nanoresonators inside the vacuum chamber. This feature allows to perform ringdown measurements at different laser powers, crucial to rule out any optothermal or optical effects of the incident laser signal on the measured Q factor (Supplementary Information Sec. F).

Supplementary information
Gas damping

Gas damping originates by the interaction between the moving surface of the resonators with the gas molecules around it and it is often dominating the extrinsic contributions at ambient condition. The nature of this loss mechanism depends on the amount of gas molecules surrounding the resonators, hence the pressure of the gas and the gas composition compared to the resonator's dimension. It can therefore be suppressed by reducing the pressure value at which the resonators operate.

To this end, we first need to evaluate the regime in which the resonator is operating and the consequent dominant gas damping mechanisms. This can be done by calculating the Knudsen number (K_n), describing the ratio of the gas mean free path length (λ_f) to the representative physical length scale of the resonator (L_r)[72]:

$$K_n = \frac{\lambda_f}{L_r} \tag{4.S1}$$

The gas mean free path length can then be calculated by the following equation:

$$\lambda_f = \frac{k_B T}{\sqrt{2}\pi d_{gas}^2} \frac{1}{p} \tag{4.S2}$$

where k_B is the Boltzmann constant, T is temperature, d_{gas} is the diameter of the gas particles, and p is the gas pressure. Atmospheric air possesses a mean free path of approximately 70 nm, several orders of magnitude lower than the representative physical lengths of the nanomechanical resonators hereby developed. It follows that at the ambient condition the resonators are dominated by viscous damping.

By decreasing the pressure, we enter the ballistic regime where the resonator dimensions become compared or smaller than the gas mean free path (Equation 4.S2), hence K_n becomes larger than unity. In this regime, the quality factor scales with the pressure until gas damping becomes negligible compared to other sources of losses. The quality factor in this regime can be calculated from an energy transfer model as[73]

$$Q_{free} = \frac{\rho t \omega}{p} \sqrt{\frac{\pi R T}{32M}} \tag{4.S3}$$

where ρ is density, t is the resonators thickness, ω is the resonance frequency, R is the molar gas constant, T is the temperature, and M is the molar mass of the gas (28.97 g mol^{-1} for air). If there is another surface in close proximity to the resonator, contributions from squeeze-film damping need to be considered and the quality factor can be calculated from

$$Q_{sq} = 16\pi \frac{d}{L} Q_{free} \tag{4.S4}$$

where d is the gap height between the resonator and nearby surface, and L is the resonator length. The total quality factor is then given by

$$Q_{tot}(p) = \left(\frac{1}{Q_{int}} + \frac{c_0}{Q_{sq}(p)} \right)^{-1} \tag{4.S5}$$
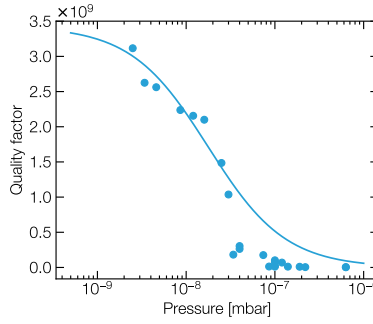
Fig. 4.S1 Measured quality factor as a function of pressure for a 3 cm optimized nanomechanical resonator. The blue line shows the fit, and the blue points indicate the experimental data.

4

where Q_{int} is the intrinsic quality factor when gas damping becomes negligible and c_0 is an experimental scaling factor[10]. It is important to notice that gas damping is not the only source of extrinsic loss. Specifically radiation loss, caused by the hard clamping of the resonator to the supporting substrate, has been reported to play a critical role. However, the nanomechanical resonators here developed employ a PnC to isolate the mechanical mode from environmental noise. This highly suppresses radiation loss as previously reported for similar designs[32]. We therefore consider the quality factor limited only by intrinsic contributions once gas damping becomes negligible. The intrinsic losses are addressed in the main text.

To quantify the effect of gas damping we performed ringdown measurements of the 3 cm nanomechanical resonator at different pressure levels and extracted the resulting quality factor from each dataset. The data points are then fitted using Equation 4.S5 with c_0 and Q_{int} as fitting parameters. The result in Fig. 4.S1 demonstrates that gas damping becomes negligible (less than 5%) for pressure levels approaching 1×10^{-9} mbar. The extracted quality factor equals the intrinsic value of 3.42 billion for this specific resonator. We therefore carried out all the measurements reported in the main text at this pressure level.

While the specific resonator employed for the pressure study hereby described is not the same device used for the results reported in Fig. 4.4 of the main text, the geometrical dimensions are equal. We can hence assume a similar gas damping behavior. Moreover Equation 4.S5 has been developed for a beam with a uniform width, while the width of our resonators varies along its entire length due to the applied tapering and the PnC. One then has to resort to numerical simulations for an accurate calculation of the quality factor at every pressure level. However, the purpose of this study is to simply find the vacuum requirements to extract the intrinsic quality factor of the fabricated resonators not limited by gas damping, rather than accurately capturing the gas damping behavior. For this purpose, Equation 4.S5 provides an accurate lower estimate.
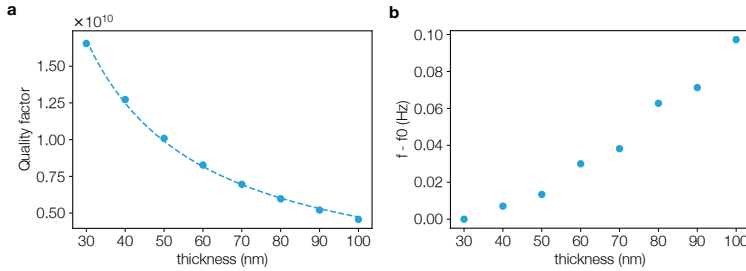
Fig. 4.S2 a, Quality factor as a function of the resonator thickness. **b**, Difference of the eigenfrequency value as a function of the resonator thickness. The data are obtained by finite element analysis by varying the thickness of the optimized design described in the main text. f_0 is the resonance frequency obtained for the 30 nm-thick resonator, corresponding to 213.323 kHz.

Variation of quality factor as function of thickness

The predicted Q factor of the optimized centimeter-scale nanomechanical resonators is 10 billion, while the fabricated structures show a Q factor of 6.6 billion. We believe the observed difference is caused by difficulties to dissipate heat during the undercut process caused by the high-aspect-ratios. This results in different thicknesses and dimensions from edge to center along the beam of the fabricated nanostructures, with a significant effect on the measured Q factor.

In this section, we investigate the case for which the thickness of the Si_3N_4 layer is uniformly 20 nm larger than the expected thickness, a value compatible with the etch settings employed during the undercut in view of the Si_3N_4 etch rate in SF_6 plasma etching and the temperature of the process.

This thickness variation results in a reduction of the quality factor from over 1 billion at 50 nm to 6.9×10^9 at 70 nm, as shown in Fig. 4.S2a. This value is in good agreement with the value experimentally measured (Fig. 4a of the main text) of 6.6×10^9. On the contrary, the thickness has a negligible effect on the resonance frequency value as displayed in Fig. 4.S2b, where f_0 is the resonance frequency obtained for the 30 nm-thick resonator, corresponding to 213.323 kHz. This value agrees with experiments to around 1%, further confirming the high-fidelity between simulations and experiments.

Stitching errors in electron beam lithography

A pattern in electron beam lithography is generated by deflecting the electron beam based on the desired shape. However, due to the finite sweep range of the deflector system, the writing field cannot exceed an area of typically 100 µm - 1 mm. The maximum writing field for the Raith EBPG 5200 machine at Kavli Nanolab in Delft is 1040 µm. Large patterns need therefore to be stitched together by moving the sample on a stage. Misalignment between multiple writing fields might then arise due to miscalibration and thermal drift among other reasons. The consequent stitching errors have significant effects on the obtained shape. This is particularly relevant for high stress Si_3N_4, where a misalignment of the order of nanometers can lead to stress concentration and rupture of the fragile suspended structure.
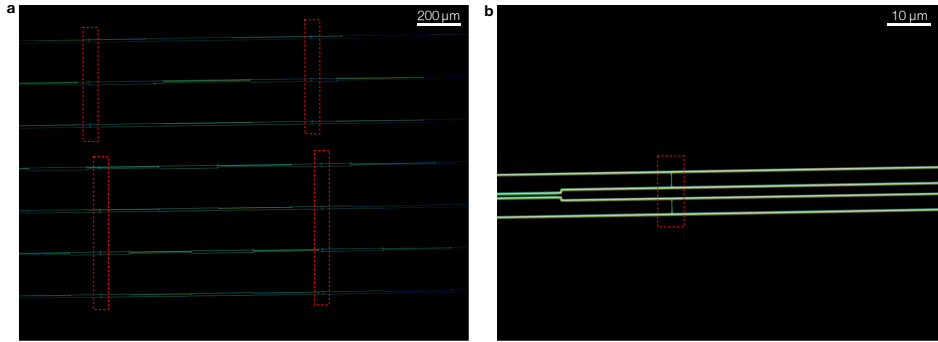
Fig. 4.S3 a, Dark-field microscope picture of a pattern with multiple structures exceeding the writing field of the electron beam lithography. **b**, Zoom-in dark-field microscope picture of a single structure at the boundary between two writing fields. The dotted red square highlights the misalignment observed between consecutive writing fields. The pictures are taken after developing the exposed e-beam resist.

The centimeter-scale nanomechanical resonators hereby developed require 30 writing fields to be correctly patterned by electron beam lithography. In order to accurately transfer the desired shape, we employed an electron beam with an estimated spot size equal to 18 nm and a spacing of 5 nm. The fine resolution results in a long writing time exceeding one hour, which increases the likelihood of misalignment and consequent stitching errors. For most of the exposed devices we in fact observed an incorrect patterning at the boundary of every writing field as shown in the dark-field microscope picture in Fig. 4.S3a. Figure 4.S3b provides a picture with higher magnification of the same structure which clearly shows a discontinuity of the written pattern.

In order to mitigate the observed stitching errors we focused first on reducing the long writing time. We did so by performing multiple exposures with different resolutions. The most critical features were exposed with a fine electron beam and high resolution, while a coarse electron beam with lower resolution was employed for the remaining areas of the pattern. As a result, the total writing time for a single 3 cm nanomechanical resonator was reduced down to 10 minutes without affecting the accuracy of the desired pattern. This was effective to eliminate the systematic misalignment previously present at every writing field boundary (Fig. 4.S3a), however, some stitching errors could still be observed in a random manner, varying from run to run.

To this end, we changed the dose at different positions to take into account possible underdose at the boundary between writing fields and overlapped each writing field with the nearby one for 100 nm. This resulted in a correct exposure of the desired pattern, without any noticeable stitching error, and an accurate transfer of the centimeter-scale nanoresonators geometry.

Photoresist cracking at cryogenic temperature

Cryogenic deep reactive ion etching (DRIE) is employed in the fabrication of the centimeter-scale nanoresonators to increase the gap separating the suspended Si_3N_4
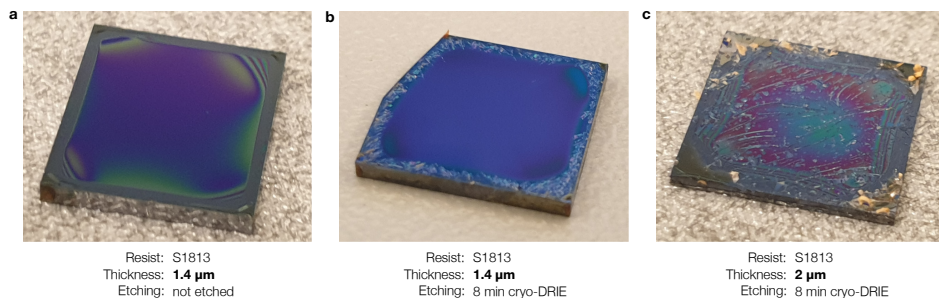
Resist: S1813	Resist: S1813	Resist: S1813
Thickness: **1.4 μm**	Thickness: **1.4 μm**	Thickness: **2 μm**
Etching: not etched	Etching: 8 min cryo-DRIE	Etching: 8 min cryo-DRIE

Fig. 4.S4 Photograph of silicon chip with photoresist spin coated on top before and after cryo-DRIE etching. **a**, Device before the cryo-DRIE step with uniform photoresist layer **b, c**, Devices with different photoresist layer after cryo-DRIE etching.

from the supporting Si substrate. Contrary to other deep silicon etching techniques as the Bosch process, cryo-DRIE is known to result in a smoother sidewall[74], and it does not leave carbon residues on the sidewall. In fact, the oxide passivation layer created to anisotropically etch Si dissolves at high temperatures. At the same time, its main drawback is the vulnerability of photoresists to cracking at low temperatures.

Previous studies found that cracking depends on the layer thickness and the specific photoresist material. The thin photoresist of less than 1.5 μm are in fact reported to be free from cracking. Moreover, materials with a high degree of cross-linking and high mechanical strength do not suffer from cracking even for larger thickness. We then studied the effect of cryo-DRIE on the photoresist SU1813, spin coated on Si_3N_4 chips with thickness varying from 1.4 μm to 2 μm, before being exposed to the fluorine-based cryo-DRIE. The thickness is varied within an interval which provides enough material to obtain the desired gap size due to the photoresist selectivity. The thicker photoresist (2 μm) shows cracks over the entire surface (Fig. 4.S4c), while in the thinner photoresist (1.4 μm) the cracks are localized at the outer area of the chip (Fig. 4.S4b), in good agreement with the expected behavior. The cracks for the outer area of the thin photoresists are most likely caused by the non-uniform thickness at the edge, as Fig. 4.S4a shows. We repeated the analysis for a second photoresist, AZ5214, without noticing any significant difference.

We therefore focused on a photoresist thickness of 1.4 μm (Fig. 4.S4b) in which the central area remains intact. Despite most of the surface being free from cracking, we observed that some cracks might propagate from the outer area towards the center with fatal consequences on the nanoresonators. Figure 4.S5a shows an example where the cracks propagate toward the nanomechanical resonators area. The cracked resist patterns can then transfer into the underneath Si_3N_4 during etching, destroying the devices. A post-baking step of 15 minutes at 120 °C prior to the etching was found to be effective to improve the photoresist plasma resistance and to further to reduce the cracks on the surface, but not to completely remove them. We also investigated the effect of the carrier wafer thickness and the Si substrate thickness. Previous studies found in fact that photoresist cracking is initiated by wafer deformation caused by the helium backside cooling system and can be mitigated by employing a thicker substrate[71]. However, in our case, the photoresist
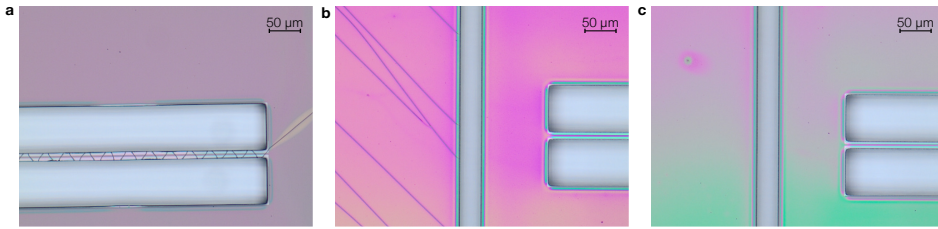
Fig. 4.S5 Optical microscope pictures of the photoresist layer after cryo-DRIE. **a**, Pattern without outer ring in which the cracks propagate toward the centimeter-scale nanoresonator. **b-c**, Pattern with the outer ring which protect the centimeter-scale nanoresonator from the cracks.
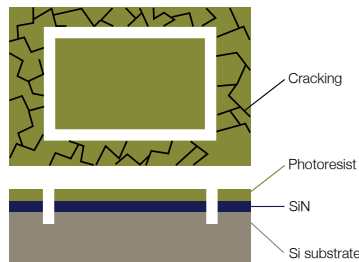

Fig. 4.S6 Schematic describing the protecting outer design.

cracking did not show any dependence on the substrate thickness.

We therefore surrounded the nanomechanical resonator's area of the device with a protecting outer ring (Fig. 4.S6). This ring is etched into both the Si_3N_4 layer and the upper part of Si substrate in order to create a physical barrier. The resulting pattern is shown in 4.S5b which clearly shows the effectiveness of the developed method to prevent any cracks from propagating toward the nanomechanical resonators. It is nevertheless important to notice that often photoresist cracking was confined to the outer area of the device without propagating toward the central area (4.S5c),

Beams collapsing

The centimeter-scale nanomechanical resonators are suspended by a fluorine based plasma etching performed at cryogenic temperature. The etching allows a quick and controllable release of the Si_3N_4 layer, without limitations from surface tension. However, plasma etching introduces charging effects due to the insulating nature of Si_3N_4. The charged Si_3N_4 can then be attracted by the Si substrate leading to the collapse of the nanoresonators.

Depending on the distance between the suspended resonator and the surrounding, we observed the Si_3N_4 being attracted toward or the side (Fig. 4.S7c) or the bottom (Fig. 4.S7b) of the opening around it. It follows that controlling the gap distance is an effective way to mitigate the collapse of the structures.
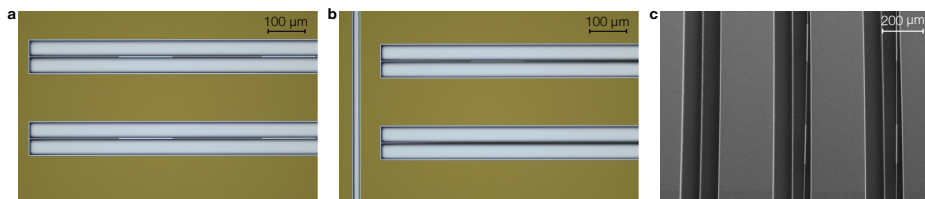
Fig. 4.S7 a, Optical microscope picture of 3 cm nanomechanical resonators correctly suspended. **b**, Optical microscope picture of 3 cm nanomechanical resonators collapsed. **c**, Scanning electron microscope picture of 3 cm nanomechanical resonators sticking to the walls.

The distance from the wall along the in-plane direction can easily be controlled lithographically during the electron beam exposure. We observed that an opening larger than 70 μm is needed to eliminate the probability of sticking to the wall. This affects the exposed area and thus the total writing time, which in turn can increase the probability of stitching errors. However as discussed in section 4.6, a multi exposure with different resolutions is an effective solution to reduce the total writing time and eliminate stitching errors.

On the other hand, the distance between the suspended resonator and the Si substrate along the out-of-plane direction needs to be controlled by an etching step. To this end, we performed a cryo-DRIE of the Si substrate prior to the release step. A gap under the suspended Si_3N_4 larger than 50 μm was observed to be needed to avoid the collapse of the structure. The final pattern used in the main text has then a distance between the resonator and the wall of around 80 μm, while the gap under the Si_3N_4 after the cryo-DRIE is of 70 μm (Fig. 4.S7a) .

Optothermal effects on the measured Q factor

The quality factor of the fabricated centimeter-scale resonators is experimentally measured with the ringdown method. The resonator is mechanically excited close to resonance with a sinusoidal function before turning off the excitation and measuring the decay time. A linear fit in the logarithmic scale of the observed decay allows us to extract the decay rate and thus the quality factor. It is however of paramount importance to avoid any unintentional excitation of the resonator during the measurement to extract the correct value of the quality factor.

One possible source of unintentional excitation is the laser employed to interferometrically probe the displacement of the resonator. The optical power impinging on the suspended resonator can in fact optothermally or optically drive it. To address this issue, we employed a laser operating at 1550 nm, the wavelength at which Si_3N_4 has negligible absorption. Moreover, we minimized the laser power coupling to the resonator down to 400 nW. This value is several orders of magnitude lower than the laser power conventionally used in previous studies (see for example[31]), where no effects correlated to optothermal or optical excitation were observed. To further dismiss any contributions we performed different ringdown measurements by varying the laser power incident on the resonator from 40 μW to 400 nW. The results in Fig. 4.S8 show a comparable decay rate
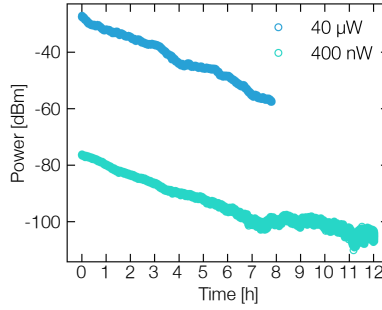
Fig. 4.S8 Ringdown traces of the optimized nanoresonator excited at 214 kHz. The motion is probed with different laser powers in consecutive measurements, plotted in the same graph for comparison.

for all the traces, suggesting that optothermal or optical effects are indeed negligible. The measurements are performed on the optimized design reported in the main text in Fig. 4.4.

Multi-fidelity Bayesian optimization

The pursuit of efficient optimization of data scarce and high-fidelity black-box functions has led to Bayesian optimization techniques. These are statistical methods that yield a belief model over the entire domain $\mathcal{X}$ which is sequentially updated through newly acquired data. The generic Bayesian optimization (BO) algorithm was originally introduced by Jones *et al.*[75], and is a proxy-optimization scheme: instead of optimizing f directly over $\mathcal{X}$, one first selects a regressor R to model the response surface $\hat{f}(\mathcal{X})$ based on a design of experiments $\mathcal{D} = \{(x_1, f(x_1)), \dots, (x_n, f(x_n))\} \subset \mathcal{X}$, which is simply a set of n known input-output pairs. Importantly, the response surface also includes a measure of uncertainty on top of the predicted outcome. This is why BO is often performed with Gaussian process regression (GPR)[76−78]. Based on this regression model $R(\mathcal{D})$, a so-called acquisition function is built and optimized over the same domain. The goal of this proxy optimization is to suggest a new point x_{n+1} in $\mathcal{X}$ to be sampled with f, and as such, the design of experiments is augmented with $(x_{n+1}, f(x_{n+1}))$. In an algorithmic format, this can be expressed as follows:

Algorithm 1 Bayesian optimization

Require: Search space $\mathcal{X}$, regressor R, design of experiments $\mathcal{D}$, acquisition function acq, threshold condition C

1: **while** C is False **do**
2:     $\hat{f} \leftarrow R(\mathcal{D})$
3:     $x \leftarrow \mathrm{argmax}_{x' \in \mathcal{X}}\, \mathrm{acq}(x'; \hat{f})$
4:     $y \leftarrow f(x)$
5:     $\mathcal{D} \leftarrow \mathcal{D} \cup \{(x, y)\}$
6: **end while**

Given the scarcity of high-fidelity data, a standard solution is to acquire higher-throughput data with lower fidelity, i.e., with larger uncertainty with lower cost. This context of simultaneous high- and low-fidelity data structures, combined with the ideas of GPR, gives rise to a multi-fidelity data driven modelling paradigm. The first multi-fidelity GPR (MFGPR) method was introduced by Kennedy & O'Hagan[79], under the term cokriging. Numerous other MFGPR methods have been constructed and researched since then[80–82], reviewed by Liu *et al.*[83].

There are several ways in which Bayesian optimization (Algorithm 1) can be extended to handle regressors R over data sets with multiple fidelities, as is the case with MFGPR. A straightforward way can be described as follows, when the m indicates the function's fidelity:

Algorithm 2 Multi-fidelity Bayesian optimization

Require: Search space $\mathcal{X}$, fidelity space $\mathcal{Z}$, regressor R, DoE $\mathcal{D}$, acquisition function acq, threshold condition C

1: **while** C is False **do**
2: $\quad \hat{f} \leftarrow R(\mathcal{D})$
3: $\quad x, m \leftarrow \mathrm{argmax}_{(x',m') \in \mathcal{X} \times \mathcal{Z}} \mathrm{acq}(x', m'; \hat{f})$
4: $\quad y \leftarrow f_m(x, m)$
5: $\quad \mathcal{D} \leftarrow \mathcal{D} \cup \{(x, y)\}$
6: **end while**

Note that this algorithm updates Algorithm 1, so that the acquisition function samples from both the fidelity function.

Interfacing MFGPR with BO has been discussed in practice by Forrester *et al.*[84] and Huang *et al.*[85] While the former simply applied expected improvement (EI) acquisition on the prediction of a single-fidelity, the latter devised an augmented version of EI. This acquisition function multiplies the EI function applied to the highest fidelity, with fidelity-dependent parameters such as the ratio of computational cost and correlation between the highest fidelity and the fidelity in question. This effectively separates the design space and fidelity space aspects of the multi-fidelity problem. More recently, Jiang et al.[86] have applied a similar multiplicative factor principle to create variable-fidelity upper confidence bound (VFUCB).

To demonstrate the process outlined by Algorithm 2, we use cokriging as the regressor (R) along with VFUCB as the 2-fidelity ($\mathcal{Z} = \{\text{low}, \text{high}\}$) acquisition function (acq). See Fig. 4.S9 for visualization in the case of multi-fidelity data $\mathcal{D}$ sampled from the high- and low-fidelity Forrester functions[84], a set of similar one-dimensional objective functions.

From Figure 4.S9, the following can be inferred:

- The maximum acquisition value of the low-fidelity branch is higher than that of the high-fidelity acquisition. Therefore, the fidelity selection $m = \text{high}$ is made in step 3 of Algorithm 2.
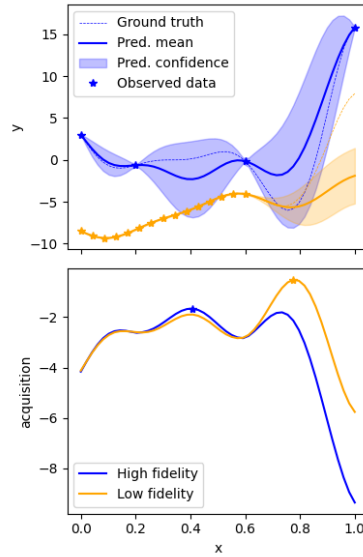
Fig. 4.S9 (top) The input-output space of the objective function. The blue solid line indicates the cokriging predictive mean for the high-fidelity data (blue stars) sampled from the high-fidelity objective function (blue dashed line). The blue shaded area corresponds to the confidence interval (two predictive standard deviations). The orange counterparts show similar results for the low-fidelity scenario. (bottom) The input-acquisition value space. The blue and orange solid lines indicate the high- and low-fidelity branches of the VFUCB acquisition function respectively. The blue and orange stars respectively show the locations at which the high- and low-fidelity acquisition branches are maximized.

- Compared to the maximizer of the high-fidelity acquisition branch, the maximizing x-value of the low-fidelity branch is closer to the minimizing x-value of the high-fidelity objective; the low-fidelity data is able to guide the optimization process.

Multi-fidelity Bayesian optimization initial random points dependency

Since our simulation-based design problem handles a stochastic optimization on the beam-like nanomechanical resonator, the initial design of experiments affects the convergence to the optimum solution. The resonator has a design space with nine design parameters, making the initial points (=25) affect the performance. Because we use multi-fidelity Bayesian optimization to reduce the total number of simulation evaluations, the curse of dimension is inevitable. **Figure 4.S10** shows the optimization history when we start from four different sets of random initial points. The change of initial points affects the convergence speed as expected, along with different behavior in selecting the fidelity. However, the optimized design obtained for all cases has converged on a similar design by taking advantage of the multi-fidelity optimization.
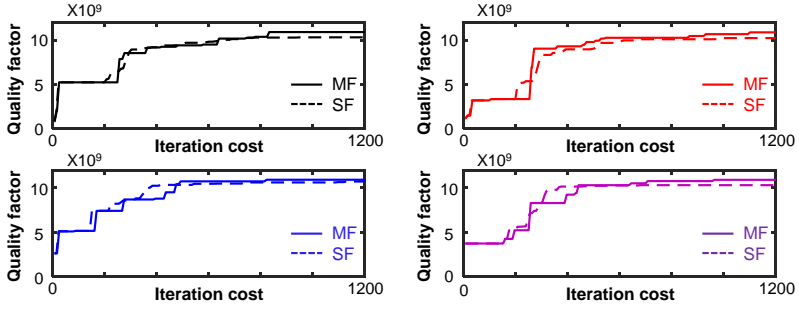
Fig. 4.S10 Iteration history of the PnC beam nanomechanical resonator for optimizing Q_m with four different randomly selected initial points. The top-left is the iteration history discussed in the main text.
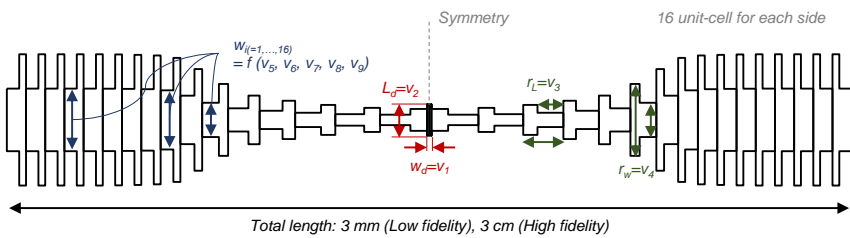

Fig. 4.S11 Nanomechanical resonator model with 16 unit cells for each side and 9 design parameters. The total length is 3 cm (high-fidelity) and 3 mm (low-fidelity).

PnC beam resonator's design parameters

The one dimensional PnC resonator has a total length of 3 cm (or 3 mm) length with a total of 32 unit cells. During the Bayesian optimization, the quality factor of the resonator is maximized by changing nine design parameters. Figure 4.S11 illustrates the design parameters of the optimized resonator discussed in the manuscript. Two parameters correspond to the defect's width (w_d) and length (L_d) in the bound of [0.5 μm, 3 μm], [150 μm, 1000 μm] ([15 μm, 100 μm]), respectively. Two parameters illustrate the width (r_w) and the length(r_L) ratio for each of the unit-cell in the bound of [1.5, 3], [0.25, 0.75], respectively. The width ratio is the ratio between the wide and thin parts of the unit cells, and the length ratio is the ratio between the length of the thin part of the unit cell versus the total length of the unit cells. The tapered shape was defined by five design parameters in the bound of [0.5 μm, 3 μm]. We performed Piecewise Cubic Hermite Interpolating Polynomial for the 16 unit-cell's width of the thin part on the shape-determinating design parameters. The simulation was performed to find the maximum quality factor in the range of 100 kHz to 400 kHz, considering the defect mode using the bandgap. The length of the unit cells was determined considering the bandgap frequency matching condition, once the set of each unit cell's width is defined[33]. During the optimization, the resonator's thickness was set to 50 nm.

Quality factors of additional devices

This section presents the measurements conducted on additional fabricated devices, which share the same optimized design and are lithographically identical to the device featured in Fig. 4 of the main text. Figure 4.S12 shows the ringdown traces of 5 devices, with the uppermost blue curve representing the measurement of the device in the main text. Linear fits for each trace are depicted as solid black lines, and the corresponding quality factors are noted above each curve. The power values on the y axis are adjusted relative to the maximum value of each curve before applying a 10 dBm offset between them. Strong fluctuations resulting from unwanted temperature drifts and mechanical vibrations of the setup can push the measured signal outside the linear region of the interference signal for a brief time interval. This, in turn, leads to occasional spikes as visible in the curve with a quality factor equal to 4.6×10^9 and 5.0×10^9.

The results show that the devices consistently exhibit a quality factor exceeding 3.7 billion at room temperature. Among all the devices fabricated and measured, we observed a variation of one order of magnitude, suggesting difference in surface quality among the devices, e.g., surface impurities and surface roughness[87], or different thicknesses. As further detailed in Sec. B, variation in the final thickness of each device might occur due to the difficulties in dissipating heat during the undercut process, significantly impacting the measured quality factor.

4

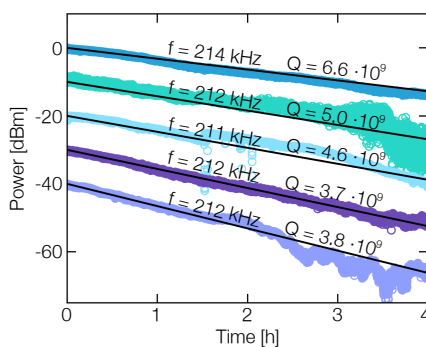**Fig. 4.S12** Ringdown traces of 5 fabricated nanoresonators with the optimized design and the design presented in the main text. To facilitate comparison, each trace has been vertically shifted relative to its respective maximum value, $(P(t) - P_{max})$. Subsequently, an incremental 10 dBm offset has been applied to each trace, starting with the top-most blue trace and concluding with the bottom-most light purple trace.

References

1. Abramovici, A., Althouse, W. E., Drever, R. W. P., Gürsel, Y., Kawamura, S., Raab, F. J., Shoemaker, D., Sievers, L., Spero, R. E., Thorne, K. S., Vogt, R. E., Weiss, R., Whitcomb, S. E. & Zucker, M. E. LIGO: The Laser Interferometer Gravitational-Wave Observatory. *Science* **256,** 325–333 (1992) (cit. on p. 62).

2. González, G. I. & Saulson, P. R. Brownian Motion of a Mass Suspended by an Anelastic Wire. *The Journal of the Acoustical Society of America* **96,** 207–212 (1994) (cit. on p. 62).

3. Sidles, J. A., Garbini, J. L., Bruland, K. J., Rugar, D., Züger, O., Hoen, S. & Yannoni, C. S. Magnetic Resonance Force Microscopy. *Reviews of Modern Physics* **67,** 249–265 (1995) (cit. on p. 62).

4. Binnig, G., Quate, C. F. & Gerber, C. Atomic Force Microscope. *Physical Review Letters* **56,** 930–933 (1986) (cit. on p. 62).

5. Rossi, N., Braakman, F. R., Cadeddu, D., Vasyukov, D., Tütüncüoglu, G., Fontcuberta i Morral, A. & Poggio, M. Vectorial Scanning Force Microscopy Using a Nanowire Sensor. *Nature Nanotechnology* **12,** 150–155 (2017) (cit. on p. 62).

6. Nichol, J. M., Hemesath, E. R., Lauhon, L. J. & Budakian, R. Nanomechanical Detection of Nuclear Magnetic Resonance Using a Silicon Nanowire Oscillator. *Physical Review B* **85,** 054414 (2012) (cit. on p. 62).

7. Harris, J., Rabl, P. & Schliesser, A. "Quantum" mechanical systems: Bridging foundations and applications. *Annalen der Physik* **527,** A13–A14 (2015) (cit. on p. 62).

8. Guo, J., Norte, R. & Gröblacher, S. Feedback Cooling of a Room Temperature Mechanical Oscillator Close to Its Motional Ground State. *Physical Review Letters* **123,** 223602 (2019) (cit. on p. 62).

9. Mason, D., Chen, J., Rossi, M., Tsaturyan, Y. & Schliesser, A. Continuous force and displacement measurement below the standard quantum limit. *Nature Physics* **15,** 745–749 (2019) (cit. on p. 62).

10. Saarinen, S. A., Kralj, N., Langman, E. C., Tsaturyan, Y. & Schliesser, A. Laser cooling a membrane-in-the-middle system close to the quantum ground state from room temperature. *Optica* **10,** 364 (2023) (cit. on pp. 62, 77).

11. Seis, Y., Capelle, T., Langman, E., Saarinen, S., Planz, E. & Schliesser, A. Ground State Cooling of an Ultracoherent Electromechanical System. *Nature Communications* **13,** 1507 (2022) (cit. on p. 62).

12. Midolo, L., Schliesser, A. & Fiore, A. Nano-Opto-Electro-Mechanical Systems. *Nature Nanotechnology* **13,** 11–18 (2018) (cit. on p. 62).

13. Magrini, L., Rosenzweig, P., Bach, C., Deutschmann-Olek, A., Hofer, S. G., Hong, S., Kiesel, N., Kugi, A. & Aspelmeyer, M. Real-time optimal quantum control of mechanical motion at room temperature. *Nature* **595,** 373–377 (2021) (cit. on pp. 62, 64).

14. Manzaneque, T., Steeneken, P. G., Alijani, F. & Ghatkesar, M. K. Method to Determine the Closed-Loop Precision of Resonant Sensors from Open-Loop Measurements. *IEEE Sensors Journal* **20,** 14262–14272 (2020) (cit. on p. 62).

4

15. Chen, X., Kothari, N., Keşkekler, A., Steeneken, P. G. & Alijani, F. Diamagnetically levitating resonant weighing scale. *Sensors and Actuators, A: Physical* **330,** 112842 (2021) (cit. on p. 62).

16. Hanay, M. S., Kelber, S. I., O'Connell, C. D., Mulvaney, P., Sader, J. E. & Roukes, M. L. Inertial imaging with nanomechanical systems. *Nature Nanotechnology* **10,** 339–344 (2015) (cit. on p. 62).

17. Reinhardt, C., Müller, T., Bourassa, A. & Sankey, J. C. Ultralow-noise SiN trampoline resonators for sensing and optomechanics. *Physical Review X* **6,** 21001 (2016) (cit. on p. 62).

18. Eichler, A. Ultra-High-Q Nanomechanical Resonators for Force Sensing. *Materials for Quantum Technology* **2,** 043001 (2022) (cit. on pp. 62, 72).

19. Cagnoli, G., Hough, J., DeBra, D., Fejer, M., Gustafson, E., Rowan, S. & Mitrofanov, V. Damping Dilution Factor for a Pendulum in an Interferometric Gravitational Waves Detector. *Physics Letters A* **272,** 39–45 (2000) (cit. on p. 62).

20. Unterreithmeier, Q. P., Faust, T. & Kotthaus, J. P. Damping of Nanomechanical Resonators. *Physical Review Letters* **105,** 027205 (2010) (cit. on pp. 62, 64).

21. Schmid, S., Jensen, K., Nielsen, K. & Boisen, A. Damping Mechanisms in High-Q Micro and Nanomechanical String Resonators. *Physical Review B* **84,** 1–6 (2011) (cit. on pp. 62, 64, 66).

22. Yu, P.-L., Purdy, T. P. & Regal, C. A. Control of Material Damping in High- Q Membrane Microresonators. *Physical Review Letters* **108,** 083603 (2012) (cit. on p. 62).

23. Cumming, A. V., Bell, A. S., Barsotti, L., Barton, M. A., Cagnoli, G., Cook, D., Cunningham, L., Evans, M., Hammond, G. D., Harry, G. M., Heptonstall, A., Hough, J., Jones, R., Kumar, R., Mittleman, R., Robertson, N. A., Rowan, S., Shapiro, B., Strain, K. A., Tokmakov, K., Torrie, C. & van Veggel, A. A. Design and Development of the Advanced LIGO Monolithic Fused Silica Suspension. *Classical and Quantum Gravity* **29,** 035003 (2012) (cit. on pp. 62, 63).

24. Dawid, D. J. & Kawamura, S. Investigation of violin mode Q for wires of various materials. *Review of Scientific Instruments* **68,** 4600–4603 (1997) (cit. on pp. 62, 63).

25. Whittle, C. *et al.* Approaching the Motional Ground State of a 10-Kg Object. *Science* **372,** 1333–1336 (2021) (cit. on p. 62).

26. Abbott, B. P. *et al.* Observation of gravitational waves from a binary black hole merger. *Physical Review Letters* **116,** 61102 (2016) (cit. on p. 62).

27. Corbitt, T., Wipf, C., Bodiya, T., Ottaway, D., Sigg, D., Smith, N., Whitcomb, S. & Mavalvala, N. Optical dilution and feedback cooling of a gram-scale oscillator to 6.9 mK. *Physical Review Letters* **99,** 160801 (2007) (cit. on p. 62).

28. Matsumoto, N., Cataño-Lopez, S. B., Sugawara, M., Suzuki, S., Abe, N., Komori, K., Michimura, Y., Aso, Y. & Edamatsu, K. Demonstration of Displacement Sensing of a mg-Scale Pendulum for mm- and mg-Scale Gravity Measurements. *Physical Review Letters* **122,** 071101 (2019) (cit. on p. 62).

29. Norte, R. A., Moura, J. P. & Gröblacher, S. Mechanical Resonators for Quantum Optomechanics Experiments at Room Temperature. *Phys. Rev. Lett.* **116,** 147202 (2016) (cit. on pp. 62, 63, 66).

30. Bereyhi, M. J., Arabmoheghi, A., Beccari, A., Fedorov, S. A., Huang, G., Kippenberg, T. J. & Engelsen, N. J. Perimeter Modes of Nanomechanical Resonators Exhibit Quality Factors Exceeding 109 at Room Temperature. *Physical Review X* **12,** 21036 (2022) (cit. on pp. 62, 63, 66).

31. Shin, D., Cupertino, A., de Jong, M. H. J., Steeneken, P. G., Bessa, M. A. & Norte, R. A. Spiderweb Nanomechanical Resonators via Bayesian Optimization: Inspired by Nature and Guided by Machine Learning. *Advanced Materials* **34,** 2106248 (2022) (cit. on pp. 62, 63, 66, 74, 82).

32. Tsaturyan, Y., Barg, A., Polzik, E. S. & Schliesser, A. Ultracoherent Nanomechanical Resonators via Soft Clamping and Dissipation Dilution. *Nature Nanotechnology* **12,** 776–783 (2017) (cit. on pp. 62, 63, 66, 69, 77).

33. Ghadimi, A. H., Fedorov, S. A., Engelsen, N. J., Bereyhi, M. J., Schilling, R., Wilson, D. J. & Kippenberg, T. J. Elastic Strain Engineering for Ultralow Mechanical Dissipation. *Science* **360,** 764–768 (2018) (cit. on pp. 62, 63, 66, 67, 69, 87).

34. Westerveld, W. J., Mahmud-Ul-Hasan, M., Shnaiderman, R., Ntziachristos, V., Rottenberg, X., Severi, S. & Rochus, V. Sensitive, small, broadband and scalable optomechanical ultrasound sensor in silicon photonics. *Nature Photonics* **15,** 341–345 (2021) (cit. on p. 62).

35. Bereyhi, M. J., Beccari, A., Groth, R., Fedorov, S. A., Arabmoheghi, A., Kippenberg, T. J. & Engelsen, N. J. Hierarchical Tensile Structures with Ultralow Mechanical Dissipation. *Nature Communications* **13,** 3097 (2022) (cit. on pp. 62, 66).

36. Pratt, J. R., Agrawal, A. R., Condos, C. A., Pluchar, C. M., Schlamminger, S. & Wilson, D. J. Nanoscale Torsional Dissipation Dilution for Quantum Experiments and Precision Measurement. *Physical Review X* **13,** 011018 (2023) (cit. on p. 62).

37. Rossi, M., Mason, D., Chen, J., Tsaturyan, Y. & Schliesser, A. Measurement-Based Quantum Control of Mechanical Motion. *Nature* **563,** 53–58 (2018) (cit. on p. 62).

38. Purdy, T. P., Peterson, R. W. & Regal, C. A. Observation of Radiation Pressure Shot Noise on a Macroscopic Object. *Science* **339,** 801–804 (2013) (cit. on p. 62).

39. Hälg, D., Gisler, T., Tsaturyan, Y., Catalini, L., Grob, U., Krass, M.-D., Héritier, M., Mattiat, H., Thamm, A.-K., Schirhagl, R., Langman, E. C., Schliesser, A., Degen, C. L. & Eichler, A. Membrane-Based Scanning Force Microscopy. *Physical Review Applied* **15,** L021001 (2021) (cit. on p. 62).

40. Chaste, J., Eichler, A., Moser, J., Ceballos, G., Rurali, R. & Bachtold, A. A Nanomechanical Mass Sensor with Yoctogram Resolution. *Nature Nanotechnology* **7,** 301–304 (2012) (cit. on p. 62).

41. Zhang, S.-D., Wang, J., Jiao, Y.-F., Zhang, H., Li, Y., Zuo, Y.-L., Özdemir, Ş. K., Qiu, C.-W., Nori, F. & Jing, H. Zeptonewton force sensing with squeezed quadratic optomechanics. *arXiv preprint,* arXiv.2202.08690 (2022) (cit. on p. 64).

4

42. Manley, J., Chowdhury, M. D., Grin, D., Singh, S. & Wilson, D. J. Searching for Vector Dark Matter with an Optomechanical Accelerometer. *Physical Review Letters* **126,** 61301 (2021) (cit. on pp. 64, 72).

43. Purdy, T. P., Grutter, K. E., Srinivasan, K. & Taylor, J. M. Quantum Correlations from a Room-Temperature Optomechanical Cavity. *Science* **356,** 1265–1268 (2017) (cit. on p. 64).

44. Dania, L., Bykov, D. S., Goschin, F., Teller, M. & Northup, T. E. Ultra-high quality factor of a levitated nanomechanical oscillator. *arXiv preprint,* arXiv:2304.02408 (2023) (cit. on pp. 64, 72).

45. Beccari, A., Visani, D. A., Fedorov, S. A., Bereyhi, M. J., Boureau, V., Engelsen, N. J. & Kippenberg, T. J. Strained crystalline nanomechanical resonators with quality factors above 10 billion. *Nature Physics* **18,** 436–441 (2022) (cit. on pp. 64, 72).

46. Ren, H., Matheny, M. H., MacCabe, G. S., Luo, J., Pfeifer, H., Mirhosseini, M. & Painter, O. Two-dimensional optomechanical crystal cavity with high quantum cooperativity. *Nature Communications* **11,** 3373 (2020) (cit. on p. 64).

47. Cupertino, A., Shin, D. & Richard, N. *Supplementary Video for Centimeter-scale Nanomechanical Resonators with Low Dissipation.* 2023 (cit. on pp. 65, 67).

48. Fedorov, S. A., Engelsen, N. J., Ghadimi, A. H., Bereyhi, M. J., Schilling, R., Wilson, D. J. & Kippenberg, T. J. Generalized dissipation dilution in strained mechanical resonators. *Physical Review B* **99,** 54107 (2019) (cit. on pp. 66, 67, 72).

49. Thompson, J. D., Zwickl, B. M., Jayich, A. M., Marquardt, F., Girvin, S. M. & Harris, J. G. Strong dispersive coupling of a high-finesse cavity to a micromechanical membrane (Nature (2008) 452, (72)). *Nature* **452,** 900 (2008) (cit. on p. 66).

50. Poloczek, M., Wang, J. & Frazier, P. I. Multi-information source optimization. *arXiv preprint,* arXiv:1603.00389 (2017) (cit. on p. 66).

51. Wu, J., Toscano-Palmerin, S., Frazier, P. I. & Wilson, A. G. Practical Multi-fidelity Bayesian Optimization for Hyperparameter Tuning. *Proceedings of Machine Learning Research* **115,** 788–798 (2019) (cit. on p. 66).

52. Inc., C. *COMSOL.* 2018 (cit. on pp. 67, 72).

53. Norte, R. A. *Nanofabrication for On-Chip Optical Levitation, Atom-Trapping, and Superconducting Quantum Circuits.* PhD thesis (California Institute of Technology, 2015) (cit. on pp. 69, 74).

54. Aspelmeyer, M., Kippenberg, T. J. & Marquardt, F. Cavity optomechanics. *Reviews of Modern Physics* **86,** 1391–1452 (2014) (cit. on p. 72).

55. Pluchar, C. M., Agrawal, A. R., Schenk, E., Wilson, D. J. & Wilson, D. J. Towards Cavity-Free Ground-State Cooling of an Acoustic-Frequency Silicon Nitride Membrane. *Applied Optics* **59,** G107–G111 (2020) (cit. on p. 72).

56. Sadeghi, P., Demir, A., Villanueva, L. G., Kahler, H. & Schmid, S. Frequency fluctuations in nanomechanical silicon nitride string resonators. *Physical Review B* **102,** 214106 (2020) (cit. on p. 72).

57. Manzaneque, T., Ghatkesar, M. K., Alijani, F., Xu, M., Norte, R. A. & Steeneken, P. G. Resolution Limits of Resonant Sensors. *Physical Review Applied* **19,** 54074 (2023) (cit. on p. 72).

58. Lewis, L. L. An Introduction to Frequency Standards. *Proceedings of the IEEE* **79,** 927–935 (1991) (cit. on p. 72).

59. Magrini, L., Rosenzweig, P., Bach, C., Deutschmann-Olek, A., Hofer, S. G., Hong, S., Kiesel, N., Kugi, A. & Aspelmeyer, M. Real-time optimal quantum control of mechanical motion at room temperature. *Nature* **595,** 373–377 (2021) (cit. on p. 72).

60. El-Sheimy, N. & Youssef, A. Inertial sensors technologies for navigation applications: state of the art and future trends. *Satellite Navigation* **1,** 1–21 (2020) (cit. on p. 72).

61. Amaro-Seoane, P., Aoudia, S., Babak, S., Binetruy, P., Berti, E., Bohe, A., Caprini, C., Colpi, M., Cornish, N. J., Danzmann, K., *et al.* Low-frequency gravitational-wave science with eLISA/NGO. *Classical and Quantum Gravity* **29,** 124016 (2012) (cit. on p. 72).

62. Xu, M., Shin, D., Sberna, P. M., van der Kolk, R., Cupertino, A., Bessa, M. A. & Norte, R. A. High-Strength Amorphous Silicon Carbide for Nanomechanics. *Advanced Materials* **n/a,** 2306513 (2023) (cit. on p. 72).

63. Manjeshwar, S. K., Ciers, A., Hellman, F., Bläsing, J., Strittmatter, A. & Wieczorek, W. High-Q Trampoline Resonators from Strained Crystalline InGaP for Integrated Free-Space Optomechanics. *Nano Letters* **23,** 5076–5082 (2023) (cit. on p. 72).

64. Pratt, J. R., Agrawal, A. R., Condos, C. A., Pluchar, C. M., Schlamminger, S. & Wilson, D. J. Nanoscale Torsional Dissipation Dilution for Quantum Experiments and Precision Measurement. *Physical Review X* **13,** 11018 (2023) (cit. on p. 72).

65. Matsumoto, N., Cataño-Lopez, S. B., Sugawara, M., Suzuki, S., Abe, N., Komori, K., Michimura, Y., Aso, Y. & Edamatsu, K. Demonstration of Displacement Sensing of a mg-Scale Pendulum for mm- and mg-Scale Gravity Measurements. *Physical Review Letters* **122,** 71101 (2019) (cit. on p. 72).

66. Balandat, M., Karrer, B., Jiang, D., Daulton, S., Letham, B., Wilson, A. G. & Bakshy, E. BoTorch: A framework for efficient Monte-Carlo Bayesian optimization. *Advances in neural information processing systems* **33,** 21524–21538 (2020) (cit. on p. 72).

67. Dougherty, D. J., Muller, R. E., Maker, P. D. & Forouhar, S. Stitching-Error Reduction in Gratings by Shot-Shifted Electron-Beam Lithography. *Journal of Lightwave Technology* **19,** 1527 (2001) (cit. on p. 74).

68. Moura, J. P., Norte, R. A., Guo, J., Schäfermeier, C. & Gröblacher, S. Centimeter-scale suspended photonic crystal mirrors. *Optics Express* **26,** 1895 (2018) (cit. on p. 74).

69. Norte, R. A., Forsch, M., Wallucks, A., Marinkovic, I. & Gröblacher, S. Platform for Measurements of the Casimir Force between Two Superconductors. *Physical Review Letters* **121,** 030405 (2018) (cit. on p. 74).

70. Maduro, L., de Boer, C., Zuiddam, M., Memisevic, E. & Conesa-Boj, S. Molybdenum nanopillar arrays: Fabrication and engineering. *Physica E: Low-Dimensional Systems and Nanostructures* **134,** 114903 (2021) (cit. on p. 74).

71. Sainiemi, L. & Franssila, S. Mask material effects in cryogenic deep reactive ion etching. *Journal of Vacuum Science & Technology B: Microelectronics and Nanometer Structures Processing, Measurement, and Phenomena* **25,** 801–807 (2007) (cit. on pp. 74, 80).

72. Schmid, S., Villanueva, L. G. & Roukes, M. L. *Fundamentals of Nanomechanical Resonators* (Springer International Publishing, Cham, 2023) (cit. on p. 76).

73. Verbridge, S. S., Ilic, R., Craighead, H. G. & Parpia, J. M. Size and Frequency Dependent Gas Damping of Nanomechanical Resonators. *Applied Physics Letters* **93,** 013101 (2008) (cit. on p. 76).

74. Henry, M. D., Welch, C. & Scherer, A. Techniques of Cryogenic Reactive Ion Etching in Silicon for Fabrication of Sensors. *Journal of Vacuum Science & Technology A* **27,** 1211–1216 (2009) (cit. on p. 80).

75. Jones, D. R., Schonlau, M. & Welch, W. J. Efficient Global Optimization of Expensive Black-Box Functions. *Journal of Global Optimization* **13,** 455–492 (1998) (cit. on p. 83).

76. Frazier, P. I. A Tutorial on Bayesian Optimization. *arXiv preprint,* arXiv:1807.02811 (2018) (cit. on p. 83).

77. Snoek, J., Larochelle, H. & Adams, R. P. Practical bayesian optimization of machine learning algorithms. *Advances in neural information processing systems* **25,** 2951–2959 (2012) (cit. on p. 83).

78. Shahriari, B., Swersky, K., Wang, Z., Adams, R. P. & De Freitas, N. Taking the human out of the loop: A review of Bayesian optimization. *Proceedings of the IEEE* **104,** 148–175 (2016) (cit. on p. 83).

79. Kennedy, M. C. & O'Hagan, A. Predicting the output from a complex computer code when fast approximations are available. *Biometrika* **87,** 1–13 (2000) (cit. on p. 84).

80. Han, Z. H. & Görtz, S. Hierarchical kriging model for variable-fidelity surrogate modeling. *AIAA Journal* **50,** 1885–1896 (2012) (cit. on p. 84).

81. Gratiet, L. L. & Garnier, J. Recursive co-kriging model for design of computer experiments with multiple levels of fidelity. *International Journal for Uncertainty Quantification* **4,** 365–386 (2014) (cit. on p. 84).

82. Bonilla, E. V., Chai, K. M. A. & Williams, C. K. Multi-task Gaussian Process prediction. *Advances in Neural Information Processing Systems 20 - Proceedings of the 2007 Conference,* 153–160 (2008) (cit. on p. 84).

83. Liu, H., Cai, J. & Ong, Y. S. Remarks on multi-output Gaussian process regression. *Knowledge-Based Systems* **144,** 102–121 (2018) (cit. on p. 84).

84. Forrester, A. I., Sóbester, A. & Keane, A. J. Multi-fidelity optimization via surrogate modelling. *Proceedings of the Royal Society A: Mathematical, Physical and Engineering Sciences* **463,** 3251–3269 (2007) (cit. on p. 84).

85. Huang, D., Allen, T. T., Notz, W. I. & Miller, R. A. Sequential kriging optimization using multiple-fidelity evaluations. *Structural and Multidisciplinary Optimization* **32,** 369–382 (2006) (cit. on p. 84).

86. Jiang, P., Cheng, J., Zhou, Q., Shu, L. & Hu, J. Variable-fidelity lower confidence bounding approach for engineering optimization problems with expensive simulations. *AIAA Journal* **57,** 5416–5430 (2019) (cit. on p. 84).

87. Villanueva, L. G. & Schmid, S. Evidence of Surface Loss as Ubiquitous Limiting Damping Mechanism in SiN Micro- and Nanomechanical Resonators. *Physical Review Letters* **113,** 227201 (2014) (cit. on p. 87).

4

5

Primary optical noise thermometry by nanomechanical resonators

Temperature is one of the most relevant physical quantities that affects almost all processes in nature. However, the realization of accurate temperature standards using current temperature references, like the triple point of water, is difficult due to the requirements on material purity and stability of the environment. In addition, in harsh environments, current temperature sensors with electrical readouts, like platinum resistors, are difficult to implement, urging the development of optical temperature sensors. In 2018, the European consortium Photoquant, consisting of metrological institutes and academic partners, started investigating new temperature standards for self-calibrated, embedded optomechanical sensor applications, as well as optimised high-resolution and high-reliability photonic sensors, to measure temperature at the nano and meso-scales and as a possible replacement for the standard platinum resistant thermometers.

This chapter presents an overview of the results obtained with sensor prototypes that exploit optomechanical techniques for sensing temperatures over a large temperature range (5 K to 300 K). Different concepts are demonstrated highlighting initial performance and challenges.

5.1. Introduction

The redefinition[1] of the kelvin in 2018 is based on a fixed value of the Boltzmann constant k_B. Consequently, the metrology community is encouraged to put strong efforts into the dissemination of the thermodynamic temperature for the mise-en-pratique of the kelvin. At the same time, there is a strong demand for sensor technology able to cover the range from cryogenic (below 1 K) up to room temperature (300 K), adapted to advanced manufacturing metrology like "lab on a chip", microelectronics, optoelectronics, or microfluidics. In addition, there is a growing demand for temperature sensors that can operate in harsh conditions, where electrical readout methods become impractical. New temperature sensors based on photonics or optomechanics are good candidates[2] to answer these metrology challenges as they offer nanoscale spatial resolution, large temperature range, and additionally can be self-calibrated with noise-thermometry and even provide a path towards primary temperature standards using quantum measurements[3].

Following NIST's first demonstration[3] of these techniques, a European consortium named "PhotoQuant: Photonic and optomechanical sensors for nanoscaled and quantum thermometry" was founded in 2017 in the framework of the Euramet network, for studying the potential and the limitations of these very new emerging technologies. This work summarizes the results and conclusions of the research efforts on the development of optomechanical temperature sensor technologies.

Our optomechanical sensors are based on a noise-thermometry technique with an optical readout in which the thermal noise of the mechanical oscillator is used to measure temperature using the equipartition theorem relation $\langle x^2 \rangle \propto k_B T$ between the displacement x of a mechanical resonance mode and temperature T. This technique is similar to Johnson noise-thermometry, which has been extensively studied for the determination of the Boltzmann constant[4]. Johnson noise-thermometry uses a correlation technique to reject non-thermal noise sources, whereas optomechanical noise-thermometry uses a high frequency resonator (MHz to GHz) to reject other noise sources. Therefore, optomechanical noise-thermometry operates at much higher frequencies that can be reached with high-speed photodetectors. Two complementary device concepts are studied: a medium frequency (MHz range) 2D membrane optomechanical resonator and a high frequency (GHz range) 1D ladder optomechanical resonator within the PhotoQuant project. We will focus only on the 2D membranes in this chapter. After the introduction of the measurement principle of optomechanical noise-thermometry, the optomechanical sensor prototypes are discussed together with the first temperature measurements using specific readout techniques dedicated to each set-up, while discussing systematic errors due to self-heating.

5.2. Measurement principle and measurement equations

Thermomechanical noise is the noise caused by the Brownian thermal motion of particles at a given temperature, associated with an average kinetic energy per degree of freedom equal to $E_k = k_B T/2$. For optomechanical resonators, it results in mechanical excitations which generate microscopic fluctuations within the resonator itself related to its temperature. As a consequence, the resonator is thermally excited with a broadband random force with a power spectral density function S_{FF} that is flat in frequency. At thermal equi-

librium, the stationary thermal force noise S_{FF} is related to the mechanical susceptibility $\chi(\omega)$ by the fluctuation-dissipation theorem[5]:

$$S_{FF} = -\frac{4k_{\mathrm{B}}T}{\omega} \, \mathrm{Im} \, \frac{1}{\chi(\omega)} = 4k_{\mathrm{B}}T\frac{m_{\mathrm{eff}}\omega_m}{Q_m}, \tag{5.1}$$

where k_{B} is the Boltzmann constant, T the temperature, m_{eff} the effective mass of the mechanical mode, ω_m the resonance frequency and Q_m the quality factor. The susceptibility is defined as[5]:

$$\chi(\omega) = \left[m_{\mathrm{eff}} \left(\omega_m^2 - \omega^2 - \frac{i\omega\omega_m}{Q_m} \right) \right]^{-1} \tag{5.2}$$

The one-sided power spectral density $S_{xx}(\omega)$ of displacements experienced by the resonator can then be inferred from the mechanical susceptibility and the thermal force noise S_{FF}[5,6]:

$$S_{xx}(\omega) \;=\; |\chi(\omega)|^2 S_{FF} \;=\; \frac{4k_{\mathrm{B}}T\omega_m}{m_{\mathrm{eff}}Q_m\left[\left(\omega_m^2 - \omega^2\right)^2 + \left(\frac{\omega\omega_m}{Q_m}\right)^2 \right]}. \tag{5.3}$$

In the case of high-Q oscillators near resonance, the power spectral density $S_{xx}(\omega)$ can be approximated by a Lorentzian (see Appendix C for details). Integrating $S_{xx}(\omega)$ over all positive frequencies gives the variance of the mechanical displacement $\langle x^2 \rangle$, which is equal to the area under the mechanical noise spectrum[6]:

$$\langle x^2 \rangle \;=\; \frac{1}{2\pi} \int_0^\infty S_{xx}(\omega)d\omega \;=\; \frac{k_{\mathrm{B}}T}{\omega_m^2 m_{\mathrm{eff}}} \tag{5.4}$$

Equation (5.4) shows that the thermodynamic temperature can be inferred from measurements of the area under the noise power produced by an optomechanical resonator of known effective mass (or stiffness), and might also be inferred from the peak in (5.3) using the measured Q and ω_m. The temperature depends purely on the Boltzmann constant as long as the resonance frequency can be measured and the effective mass calculated. Therefore, so long as the sensor displacement can be precisely measured and the resonance frequency and the effective mass are known, the resonator holds the potential to develop a primary optical noise thermometer[7], which does not require independent temperature calibration, similar to a Johnson noise thermometer[4]. An advantage of optical interrogation is its inherent resistance to electrical noise and interference, provided that ideal conditions are met.

If m_{eff} or $k_{\mathrm{eff}} = m_{\mathrm{eff}}\omega_m^2$ are not exactly known as in our case, they might be determined using (5.4) from a measurement at a single known reference temperature. Once calibrated at this reference temperature, the optomechanical thermometer will provide an accurate temperature reading at all other temperatures based on (5.4), provided that its effective mass is independent of temperature. In this case, the thermometer is not self-calibrated.
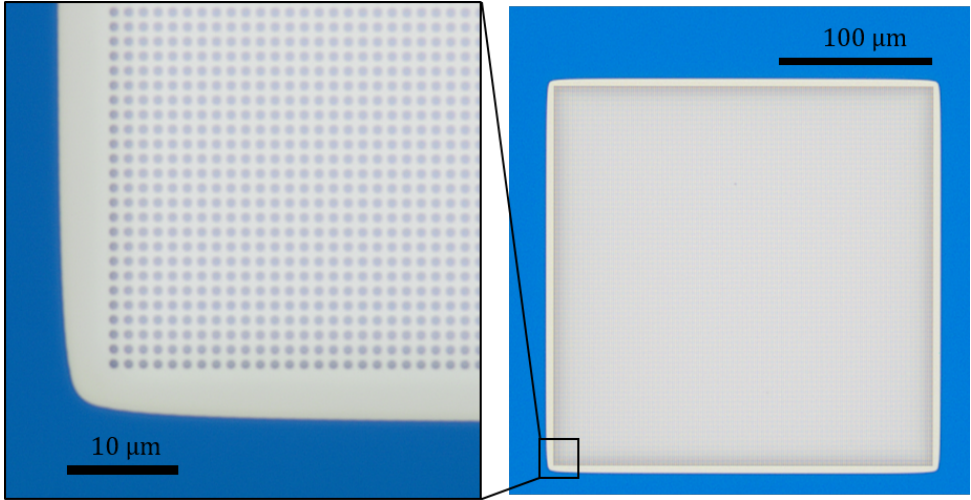
Fig. 5.1 Optical microscope image of the suspended square membrane. The blue color is from the thin-film interference effects of the nonsuspended silicon nitride on silicon substrate.

5.3. Fabrication and Characterization of the Resonators

To experimentally validate the proposed thermometry scheme, we fabricated optomechanical devices consisting of 2D square membranes (2DSM) with mechanical modes in the MHz domain.

The 2DSM are fabricated on high-stress silicon nitride, a material known for its ultralow mechanical dissipation and hence high quality factor. Due to the high tensile stress, silicon nitride thin films can exhibit quality factors as high as 10^6 [8]. Engineering the structure can then further reduce the losses and bring the quality factor over 10^8 [9–11].

A high quality factor for our optical noise thermometer is beneficial to increase the peak value of the power spectral density, which can be calculated from Equation (5.3):

$$S_{xx}(\omega_m) \ = \ \frac{4k_{\mathrm{B}}TQ_m}{\omega_m^3 m_{\mathrm{eff}}} \tag{5.5}$$

This allows for detecting the small fluctuations of the resonator caused by thermomechanical noise, otherwise hidden by the noise floor.

At the same time, a high quality factor results in a small linewidth $\Gamma_m(Q_m = \omega_m/\Gamma_m)$—typically down to a few mHz for silicon nitride resonators—which poses a challenge on the read-out protocol. In order to precisely extract the temperature from the mechanical displacement $\langle x^2 \rangle$, the read-out protocol needs to measure the mechanical spectrum with sufficient data points around the peak, requiring a measurement bandwidth smaller than the resonator's linewidth. To do so, one needs to acquire a long time trace and extract the mechanical properties from its Fourier transform, but this method exposes the measurement to artificial broadening mechanisms due to the shift of the resonance frequency during the measurement, limiting the minimum measurable linewidth. It follows that, for a reliable measurement of the temperature, the mechanical resonator needs to have a

linewidth Γ_m large enough to avoid shifting of the resonance frequency within the measurement time, while being small enough to have high enough Q and signal strength to detect the thermomechanical peak and precisely determine its resonance frequency.

To optimize this trade-off, we fabricated resonators with different devices and geometries which led to a wide range of quality factors up to 10^9 at room temperature[12]. Hence, we acquired the spectrum of each resonator and found that, above $Q_m = 10^7$, our read-out protocol cannot detect the change of the mechanical displacement $\langle x^2 \rangle$ as a function of temperature, due to the low linewidth Γ_m. All the measurements with 2DSM presented in this work are therefore performed on a square membrane of 80 nm thickness with an approximate quality factor $Q_m = 10^6$. As shown in Figure 5.1a, the membrane is patterned with holes of 450 nm radius and 1438 nm lattice constant, to allow the release of the structure from the silicon substrate underneath. Those holes affect the resonator's mass-per-area reducing the effective mass, increasing the resonance frequency, and keeping the effective stiffness k_{eff} ($\omega^2 m_{\text{eff}} = k_{\text{eff}}$) unchanged. The silicon nitride is deposited by low-pressure chemical vapor deposition on the silicon substrate. The pattern is first written by electron beam lithography into a resist and then transferred to the silicon nitride by a dry-etching step. Finally, the membrane is released with a dry etching step which isotropically etches the silicon substrate underneath. The fabricated membrane has an initial stress of 1.1 GPa, which leads to a resonance frequency of the fundamental flexural mode of 1.338 MHz for the square membrane with a side length of 250 μm shown in Figure 5.1.

5.4. Thermometry measurements

Figure 5.2b shows the measured power spectra $S_{VV}(\omega)$ on the photodiode that is proportional to $S_{xx}(\omega)$, acquired at four different temperatures from 260 K to 10 K by a spectrum analyzer with the measurement setup in Figure 5.2a. The mechanical displacement is probed using a Helium Neon (HeNe) laser (632.8 nm) and the mechanical resonator is mounted inside a cryogenic vacuum chamber, at a pressure of the order of 10^{-6} mbar. The sample holder is equipped with an ITS-90 calibrated commercial thin film resistance temperature sensor, which assures IT-90 traceability. The linearly polarised laser beam from the HeNe laser is sent first through a polarization beam splitter, transparent for vertically polarized light, and then through a $\frac{\lambda}{4}$ plate rotated at 45°, circularly polarizing the light. The light is then focused on the sample by a ×20 objective. The focused light is partially reflected by the suspended silicon nitride membrane, partially transmitted to the underneath silicon substrate, and reflected by it, creating a Fabry-Perot cavity. The interference between the different light paths results in a position dependent light intensity that is used to determine the membrane's motion. The reflected light passes again through the $\frac{\lambda}{4}$ plate and is focused on the photodiode, connected to a spectrum analyzer which allows for extracting the Brownian motion[13].

As expected from Equations (5.3) and (5.4), the measured power spectra $S_{VV}(\omega)$ and mechanical displacement $\langle x^2 \rangle$ exhibit a clear dependence on the temperature of the resonator. To determine $S_{xx}(\omega)$, the data are first pre-processed with a binning algorithm to reduce the noise. Then, a thermomechanical calibration of the measurement setup[5] is performed using the spectrum acquired at a temperature T=260 K determined using the

a

b

c
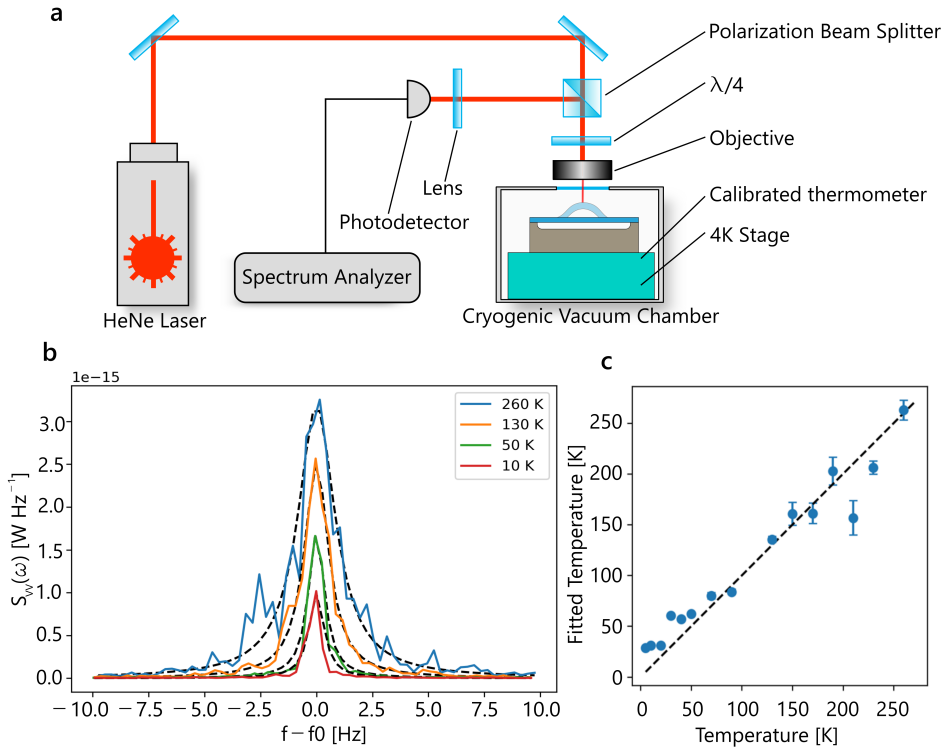
Fig. 5.2 (**a**) Schematic of the mechanical characterization setup. The mechanical resonator is placed inside a cryogenic vacuum chamber and the displacement is caused by Brownian motion. Interference between reflected laser light reflected from substrate and membrane causes a displacement dependent intensity on a photodiode that is detected using a spectrum analyzer; (**b**) thermomechanical noise spectra at different temperatures obtained using a spectrum analyzer. The x-axis is centered at the fundamental resonance frequency f_0 of each spectrum for comparison. Dashed lines represent fits using (5.3). (**c**) temperature extracted from the measurements in (**b**) by integrating the area under the peak. The error bars show the standard deviation.

Cernox sensor. This last step allows for obtaining the conversion factor from $S_{VV}(\omega)$ to $S_{xx}(\omega)$. Alternatively, the conversion factor can be obtained by replacing the Fabry-Perot interferomter with a Michelson interferometer in a balanced homodyne scheme equipped with a feedback loop, where the reference arm can cover more than the laser wavelength[14]. After that, the spectrum acquired at each temperature can be fitted by Equation (5.3), where m_{eff} is analytically calculated using the reference measurement at T=260K and the values of Q_m and ω_m obtained from the fits. Finally, the temperature of the resonator is calculated by integrating the fitted curve $S_{xx}(\omega)$ and obtaining the mechanical displacement $\langle x^2 \rangle$. At each temperature, the focus on the sample is adjusted to ensure a comparable sensitivity over the entire temperature range. We note that this procedure can introduce additional uncertainty in the conversion factor, which should be eliminated in the final implementation of the thermometry protocol, e.g., using a calibration tone. Figure 5.2c shows the fitted temperature for each measurement, compared to the temperature of the resonator obtained from the independent calibrated commercial sensor. The error bars indicate the standard deviation for each measurement. Measurements with a standard deviation larger than 20 K are discarded. All the data points, including the ones with a standard deviation larger than 20 K are included in the Supporting Information. This result shows reasonable agreement between the optical noise-thermometry method and the temperature obtained from the independent calibrated sensor over the range of 5 K to 260 K, providing evidence for the potential of the described thermometry technique. Due to the small linewidth and peak height at low temperatures, the error bars and uncertainty in the optomechanical noise-thermometry increase at low temperatures, causing deviations from the temperature obtained from the independent calibrated sensors. The positive deviation of the temperature at low might partly be attributed to a systematic overestimation of the peak area by the employed fitting routine.

5.5. Investigation of systematic errors coming from departure from thermal equilibrium

Let us now investigate the effect of systematic errors on the temperature measurement precision and accuracy. We focus mainly on the effect of optical heat absorption on the measured temperatures.

Employing a high laser power is beneficial for increasing the resonance signal level well above the measurement noise floor. However, high laser power can lead to photothermal effects due to the absorption of laser light, leading to an incorrect measurement of the temperature. To study this effect, we acquired thermomechanical noise spectra at a constant temperature of $T = 5$ K for different values of the laser power (Figure 5.3b), with the mechanical characterization setup depicted in Figure 5.2 and used a finite-element model of our resonator to numerically analyse the absorbed optical power and the resulting temperature distribution using Comsol. The material parameters are Young's modulus $E = 270$ GPa, mass density $\rho = 3200$ kg/m^3, and Poisson's ratio $\nu = 0.27$, while the assumed optical properties are thermal conductivity $k = 20$ W(mK)$^{-1}$, thermal expansion coefficient $\alpha = 2.3 \times 10^{-6}$ K^{-1} and heat capacity $C_p = 700$ J kg^{-1}K^{-1})[15]. The laser heating is simulated assuming a Gaussian beam profile at the center of the resonator and the outer boundaries of the resonator are set to 5 K. The result in Figure 5.3a shows a local-
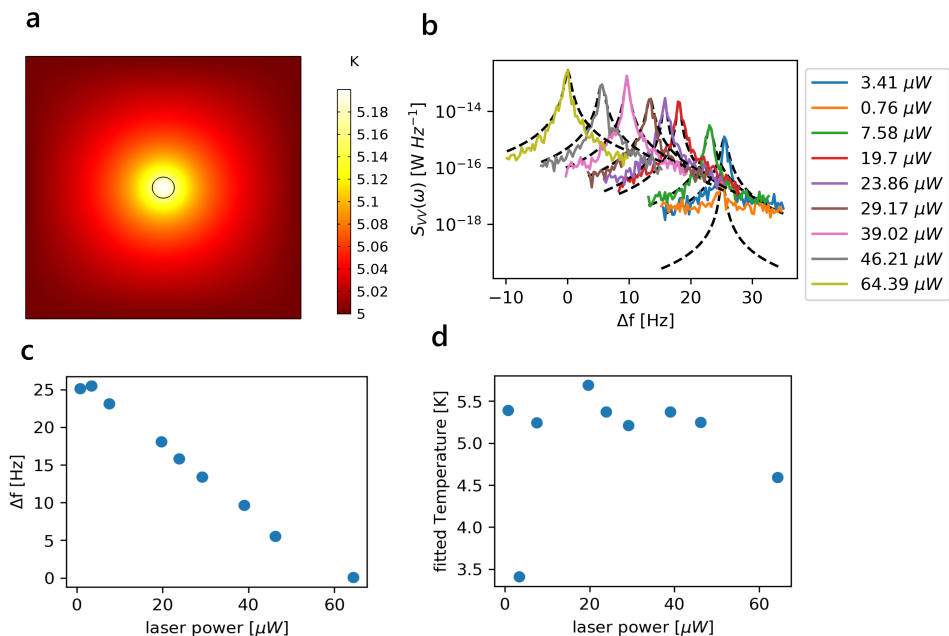
Fig. 5.3 a, Simulated temperature distribution plot with an incident power P = 64.39 μW. **b**, Thermomechanical noise spectra measured at a temperature of 5 K for different laser powers. The x-axis is the difference in frequency from the resonance frequency measured with a laser power of 64.39 μW, equal to 1.331 MHz. **c**, Measured resonance frequency difference versus laser power with respect to the resonance frequency acquired with a laser power of 64.39 μW. **d**, temperature extracted from the measurements in **b** by integrating the area under the peak versus laser power.

ized temperature increase in the center of the 2DSM of 0.18 K at an incident laser power of 64.39 μW, the highest value employed in the measurement. The laser power absorbed by the SiN membrane is 0.64 μW, 1.01% of the incident power[16]. The localized laser heating, and associated temperature increase, has a three-fold effect on the developed noise-thermometry scheme: the resonance frequency decreases as a result of the tension induced by thermal expansion, the area under the S_{xx} spectrum increases according to (5.3) and the signal on the photodiode increases due to the larger conversion factor at higher laser power. Figure 5.3c shows the change in resonance frequency as a function of incident laser power, where a linear relation can be observed as expected. From this relation, the average temperature change in the SiN membrane can be estimated using literature values of the thermal expansion coefficient $\alpha = 2.3 \times 10^{-6}\,\mathrm{K}^{-1}$ and Young's modulus $E = 270$ GPa, using $\Delta f = -\alpha E \Delta T f_0 / n_{\mathrm{pre}}$, using the prestress of $n_{\mathrm{pre}} = 1.1$ GPa in the membrane and its resonance frequency $f_0 = 1.33$ MHz. With this estimation formula, the frequency shift of $\Delta f = 60$ Hz in Figure 5.3c is estimated to correspond to an average temperature increase $\Delta T = 80$ mK, a value that is of the same order of magnitude as the simulated temperature increases in Figure 5.3a. This calculation also shows that the resonance frequency can be an accurate measure of temperature that might complement noise thermometry protocols for reaching higher precision temperature measurements, while using thermomechanical noise for accuracy and self-calibration. In Figure 5.3d, the temperature at every laser power was determined using noise thermometry, by integrating the fitted area under the peaks in Figure 5.3b with Equation (5.4). Prior to the fits shown in Figure 5.3b, an additional thermomechanical calibration step is performed for all the spectra, providing for each laser power a conversion factor from $S_{VV}(\omega)$ to $S_{xx}(\omega)$. However, the error in the temperature measurement using this procedure is larger than the laser-induced temperature changes of 80 mK, such that the effect of laser power on temperature cannot be as clearly resolved as by using the resonance frequency shift in Figure 5.3c.

5.6. Conclusions

The measurement of temperature using optomechanical on-chip thermometers is of growing interest to the scientific and industrial communities. This interest is driven by the potential to perform thermometry in harsh environments, with sensors that provide accurate readings while providing advantages in terms of linearity and calibration. In this study, we provide experimental studies on optomechanical thermometers demonstrating different sensing and calibration approaches. Photomechanical noise-thermometry on nanomechanical devices was applied to measure temperatures over the range from 5 K to 300 K. Due to the linearity provided by the equipartition theorem, a single calibration was sufficient to determine temperature over the whole temperature range.

Limitations in terms of optothermal self-heating of the sensors were assessed to provide optimal operation conditions. The resolution of the temperature measurement is limited by experimental factors like stability, self-heating, and the accuracy by which the thermomechanical noise peak can be characterized. In future studies and applications, the presented technologies might be merged with photonics devices, to combine the high-precision of photonic thermometry with the self-calibration potential of optomechanical thermometers.
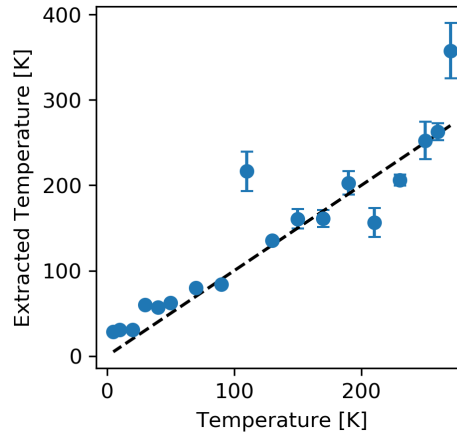
Fig. 5.S1 Temperature extracted from the measurements in Fig. 5.2b by integrating the area under the peak. The error bars show the standard deviation

Supplementary information

Figure 5.S1 shows all the temperature measurements extracted by integrating the area under the peak of the power spectral density. It is the same dataset shown in Fig. 5.2c, including also the measurements with a standard deviation larger than 20 K. The dashed line shows the linear fitting obtained by discarding the measurements with a standard deviation larger than 20 K, as detailed in the main text.

References

1. Fellmuth, B., Fischer, J., Machin, G., Picard, S., Steur, P. P. M., Tamura, O., White, D. R. & Yoon, H. The kelvin redefinition and its mise en pratique. *Phil. Trans. R. Soc. A.* **374.** 2016) (cit. on p. 98).

2. Klimov, N., Purdy, T. & Ahmed, Z. Towards replacing resistance thermometry with photonic thermometry. *Sensors and Actuators A: Physical* **269,** 308–312 (2018) (cit. on p. 98).

3. Purdy, T. P., Grutter, K. E., Srinivasan, K. & Taylor, J. M. Quantum correlations from a room-temperature optomechanical cavity. *Science* **356,** 1265–1268 (2017) (cit. on p. 98).

4. Qu, J. F., Benz, S. P., Rogalla, H., Tew, W. L., White, D. R. & Zhou, K. L. Johnson noise thermometry. *Measurement Science and Technology* **30,** 112001 (2019) (cit. on pp. 98, 99).

5. Hauer, B., Doolin, C., Beach, K. & Davis, J. A general procedure for thermomechanical calibration of nano/micro-mechanical resonators. *Annals of Physics* **339,** 181–207 (2013) (cit. on pp. 99, 101).

6. Aspelmeyer, M., Kippenberg, T. J. & Marquardt, F. Cavity optomechanics. *Rev. Mod. Phys.* **86,** 1391–1452 (2014) (cit. on p. 99).

7. Steeneken, P. G., Le Phan, K., Goossens, M. J., Koops, G. E. J., Brom, G. J. A. M., van der Avoort, C. & van Beek, J. T. M. Piezoresistive heat engine and refrigerator. *Nature Physics* **7,** 354–359 (2011) (cit. on p. 99).

8. Verbridge, S. S., Parpia, J. M., Reichenbach, R. B., Bellan, L. M. & Craighead, H. G. High quality factor resonance at room temperature with nanostrings under high tensile stress. *Journal of Applied Physics* **99,** 124304 (2006) (cit. on p. 100).

9. Norte, R. A., Moura, J. P. & Gröblacher, S. Mechanical Resonators for Quantum Optomechanics Experiments at Room Temperature. *Phys. Rev. Lett.* **116,** 147202 (2016) (cit. on p. 100).

10. Tsaturyan, Y., Barg, A., Polzik, E. S. & Schliesser, A. Ultracoherent nanomechanical resonators via soft clamping and dissipation dilution. *Nature Nanotechnology* **12,** 776–783 (2017) (cit. on p. 100).

11. Ghadimi, A. H., Fedorov, S. A., Engelsen, N. J., Bereyhi, M. J., Schilling, R., Wilson, D. J. & Kippenberg, T. J. Elastic strain engineering for ultralow mechanical dissipation. *Science* **360,** 764–768 (2018) (cit. on p. 100).

12. Shin, D., Cupertino, A., de Jong, M. H. J., Steeneken, P. G., Bessa, M. A. & Norte, R. A. Spiderweb Nanomechanical Resonators via Bayesian Optimization: Inspired by Nature and Guided by Machine Learning. *Advanced Materials* **34,** 2106248 (2022) (cit. on p. 101).

13. Davidovikj, D., Slim, J. J., Cartamil-Bueno, S. J., van der Zant, H. S. J., Steeneken, P. G. & Venstra, W. J. Visualizing the Motion of Graphene Nanodrums. *Nano Letters* **16,** 2768–2773 (2016) (cit. on p. 101).

5

14. Jaeger, D., Fogliano, F., Ruelle, T., Lafranca, A., Braakman, F. & Poggio, M. Mechanical Mode Imaging of a High-Q Hybrid hBN/Si3N4 Resonator. *Nano Letters* **23.** PMID: 36847481, 2016–2022 (2023) (cit. on p. 103).

15. Sadeghi, P., Tanzer, M., Luhmann, N., Piller, M., Chien, M.-H. & Schmid, S. Thermal Transport and Frequency Response of Localized Modes on Low-Stress Nanomechanical Silicon Nitride Drums Featuring a Phononic-Band-Gap Structure. *Phys. Rev. Applied* **14,** 024068 (2020) (cit. on p. 103).

16. Chien, M.-H., Brameshuber, M., Rossboth, B. K., Schütz, G. J. & Schmid, S. Single-molecule optical absorption imaging by nanomechanical photothermal sensing. *Proceedings of the National Academy of Sciences of the United States of America* **115,** 11150–11155 (2018) (cit. on p. 105).

5

6

Conclusion and Outlook

This thesis aimed to explore the limits of nanomechanical resonators with low dissipation at room temperature and their sensing capability. We saw that dry etching is a powerful technique to fabricate such resonators and avoid stiction and collapse, particularly advantageous for devices with increasingly high aspect ratios. The combination of a high fabrication yield and high fidelity achieved through this dry etching technique enables to use machine learning tools to design and optimize new types of resonators. We thereby demonstrated the ability of machine learning to work in tandem with human intuition to augment creative possibilities and uncover new design strategies. Lastly, we investigated the potential of nanomechanics to accurately measure temperature over a wide range.

In doing so, we addressed many fundamental and applied issues related to the field of low dissipation nanomechanical resonators but additional questions arose.

6.1. Stiction-free fabrication

In chapter 2 we investigated the etching characteristic of dry isotropic silicon etching by sulfur hexafluoride plasma at cryogenic temperature. Despite being an established way to etch silicon, its application for suspending nanomechanical resonators without any masking layer has not been studied thus far. We measured a silicon etch rate above 10 μm/min with a high degree of isotropy combined with high selectivity against silicon nitride. This allows preserving the silicon nitride film quality, making it an ideal alternative to wet release with the twofold advantage of reducing the fabrication steps and circumventing the issues inherent to wet processes. Additionally, the etching enables the creation of any shapes without limitations from the crystal planes of the substrate, crucial to realizing the structures in this thesis.

At the same time, we discovered an asymmetry between the etch rate along the vertical and the horizontal direction due to shadowing effects and the residual voltage. Optimization of the gas concentration and the applied ICP power could then be considered to further increase the degree of isotropy and the total etch rate. Although the measured selectivity exceeds one thousand, we observed a time-dependent decrease in the silicon nitride thickness which needs to be compensated with the deposition of a thicker film. More crucially, the surface roughness of silicon nitride increased during the process. Based on the excellent agreement shown in the following chapters of this thesis between simulations and experiments, we believe the change in surface roughness has negligible effects on the resonator's performance. Nevertheless, an additional polishing step after the etching is a promising approach for mitigating the increase in surface roughness.

Lastly, plasma etching is known to introduce charging effects in insulating materials which might result in the collapse of the suspended fragile structures. For millimeter-size resonators (chapters 3, 5) we did not observe any issues. However, the contrary is true once we scaled the aspect ratio reaching centimeter-scale resonators in chapter 4 due to the small gap under the structures. An additional step to the fabrication process was then developed to increase the gap size for realizing the structure. However, finding strategies to avoid charging effects as by optimizing the plasma power or by varying the substrate material is a valuable next step to improve the reliability of the etching.

As it pertains to the materials employed, we only targeted nanomechanical resonators made from stoichiometric silicon nitride over silicon substrates given their superior properties. Silicon nitride is in fact characterized by an intrinsic low mechanical dissipation combined with low absorption in the infrared wavelength, specifically advantageous for optomechanics applications. More recently, different materials have also been proposed for realizing high quality factor resonators as amorphous silicon carbide[1], crystalline silicon carbide[2], silicon[3], diamond[4] and indium gallium phosphide[5]. Various substrate materials have equally been investigated[6] mainly to increase the initial tensile stress in the resonators. We expect that dry etching techniques will play an important role in the development of future devices with other platforms more than only silicon nitride resonators.

6.2. Spiderweb nanomechanical resonators

In chapter 3 we used a simulation-based data-driven optimization approach to design nanomechanical resonators with quality exceeding 1 billion, among the highest yet mea-

sured at room temperature. Building on millions of years of evolution, the approach takes advantage of the remarkable properties of spiderwebs as a starting design. Our optimization guided by machine learning allows then to adapt the spiderweb design for high-precision sensors, discovering a new "soft-clamping" mechanism to achieve high quality at low order modes and compact size. The mechanism exploits the coupling between the torsional mode of the clamping area with the bending mode of the central beams to highly isolate the motion of the resonator.

Our experimental validation of the fabricated spiderweb resonators is in excellent agreement with the predicted values. The extracted quality factor value via ringdown measurements of the isolated mode is 1.8×10^9 at 133 kHz, more than one order of magnitude higher than the other mechanical modes in the spiderweb resonator. This further corroborates the presence of the novel soft-clamping mechanism that avoids radiation losses without using phononic crystals. Remarkably, the result is obtained with minimum feature sizes of 1 μm and a thickness of 50 nm, values higher than comparable devices, which allows a fast and cost-effective fabrication compatible with optical lithography.

The obtained high quality factor and low resonance frequency represents an important step toward high-precision sensing with applications ranging from quantum limited force microscopy[7], "cavity-free" cooling scheme[8] and quantum control of motion at room temperature[9,10]. Equally importantly, the design strategy combined with the accurate fabrication process is not restricted to the specific problem here described and can be applied to a wide range of objective functions targeting new applications. Optimization for force sensing would for example be a natural next step from an applications standpoint.

Another point worth discussing for further improvements is the quality factor limit in the spiderweb resonators. Our investigation showed that, despite the high value obtained, the quality factor is not at the ultimate limit yet. The ultimate limit will be achieved if all the curvature at the clamping point is suppressed, a regime called "perfect soft clamping assumption" in the chapter. Our spiderweb resonators exhibit however a non-negligible curvature in the form of torsion. We expect that further optimization of the edge area where the lateral beams coupled to the radial beam would have a significant impact on the resulting energy lost. Shape optimization or topology optimization might be considered for this goal. At the same time, a reduction of the minimum feature size and thickness is expected to improve the resonator's quality factor at the cost of making the fabrication less accessible for general use. Finally, the quality factor limitations can equally be overcome by scaling the resonator's lateral dimension as we demonstrated in chapter 3. However, it comes at the cost of operating at higher order modes and higher frequency, outside the scope of this chapter.

6.3. Centimeter-scale resonators

In Chapter 4, we aimed to explore the high-quality factor limits of nanomechanical resonators and venture into a previously unexplored regime using on-chip devices. We did so by successfully designing and fabricating centimeter-scale resonators. However, this required addressing challenges associated with designing and realizing structures at this length scale, namely significant simulation costs and fabrication constraints. Leveraging the insights gained from the previous chapter, we then employed a multi-fidelity optimization technique to effectively reduce the simulation cost while maintaining accuracy.

Starting from a tapered phononic crystal string, our optimization allows the discovery of a centimeter-scale resonator that exhibited a predicted quality factor exceeding 10 billion at room temperature. Interestingly, our newly discovered geometry differs from previous designs in that it did not aim to maximize the stress in the center of the resonator, suggesting the presence of a trade-off between bending loss and clamping loss.

We then proceeded to fabricate the optimized resonators using a combination of sulfur hexafluoride etching release and deep reactive ion etching. This fabrication approach offers the advantage of independent control over the size of the gap beneath the resonators, mitigating the risk of collapse due to the extreme aspect ratio and resulting in a fabrication yield approaching 100%. However, it is worth noting that the fabricated devices differ from the simulation predictions in terms of thickness. Instead of the anticipated 50 nm, the devices have a measured thickness of 70 nm, with a notable impact on the resulting aspect ratio. Despite this deviation, the experimental validation of the fabricated resonators demonstrates a high quality factor exceeding 6 billion at a frequency of 214 kHz, confirming the expected trend with the aspect ratio, further supporting our findings.

Overall, the findings discussed in this chapter present significant prospects for creating nanomechanical resonators with centimeter-scale length. Clearly, the optimized resonator is simply one example demonstrating the effectiveness of our approach and the resulting advantage of an extreme high aspect ratio. Owning to its versatility, a more extreme aspect ratio can be targeted with a wide range of potential applications. These include the exploration of weak forces such as ultralight dark matter[11], the development of highly sensitive sensors[12], and the investigation of gravitational effects at the nanoscale[13]. Furthermore, the approach we have developed holds promise beyond its application solely to nanomechanical resonators. It is also of interest for designing and fabricating large-scale thin suspended elements in general, expanding the potential impact of our work and opening up new avenues for research and innovation in related areas.

6.4. Noise thermometry

In chapter 5 we demonstrated the sensing capability of nanomechanical resonators for primary optical noise thermometry. The measurement principle is based on a noise-thermometry technique by which the temperature can be detected from the resonator displacement due to Brownian motion. The technique takes advantage of the high quality factor of the employed nanomechanical resonators to detect the Brownian motion, otherwise hidden by the noise floor. However, the high quality factor required addressing challenges associated with our read-out protocol given the small linewidth and long integration time.

Optomechanical noise-thermometry was then applied to the fabricated resonators to measure the temperature over a wide range from 5 K to 300 K. The obtained results show a linear behaviour, as predicted by the equipartition theorem, with a statistical uncertainty of 8 K. The latter is dominated by the accuracy by which we can characterize the thermo-mechanical noise peak, limited by the read-out protocol. Finite element analysis shows a negligible effect caused by self-heating due to the incident laser power used to interferometrically read out the resonator's displacement. This suggests that an improvement of the read-out scheme can significantly increase the uncertainty.

For future development, it will be interesting to complement noise thermometry pro-

tocols with other techniques with higher precision, like the shift in resonance frequency due to temperature. In this way, the sensor could benefit from noise thermometry for calibration while reaching higher precision temperature measurements with the additional technique. Another promising path, although more challenging from a fabrication point of view, is to merge it with photonic thermometry in a single chip in view of the superior precision.

6.5. Final considerations

Besides our approach, many works have recently been published proposing different strategies to obtain mechanical resonators with enhanced quality factors. Topology optimization has been used to optimize trampoline resonators[14], specifically the shape of the clamping area. By doing so, this approach does not rely on soft-clamping to enhance the quality factor but rather on reducing radiation loss toward the substrate. This poses limitations on the maximum achievable quality factor but opens new opportunities for resonators operating at the fundamental mode, specifically trampoline resonators. A similar optimization has been applied to a membrane to create pillar-shaped phononic crystals[15]. The working principle is similar to other phononic crystals previously reported, but with added flexibilities in terms of stress redistribution at the cost of a more complex fabrication. We believe the combination of different optimizations for different areas of the resonators might prove successful in discovering new strategies to enhance the quality factor.

Hierarchical and perimeter geometries have also been developed[16,17], resulting in quality factors comparable to our resonators discussed in chapters 4, 5. However both approaches require significantly smaller feature sizes (smaller than $1\,\mu m$) and smaller thickness, with an impact on the fabrication accessibility. Lastly, high quality factor has been measured in torsional modes of strained strings[13]. Although the obtained value is one order of magnitude lower than what can be achieved with bending modes, the resonators can be mass-loaded with advantages for acceleration sensing. The enlarged design space resulting from those new geometries is a promising starting point for new optimizations, with the potential to discover new strategies for low dissipation nanomechanical resonators.

Given the increasingly high surface-to-volume ratio, we anticipate that high aspect ratio resonators will exhibit increased sensitivity to surface defects. The quality factor is known to be limited by surface loss for resonators with a thickness below $100\,\text{nm}$[18]. However, the precise underlying cause of this loss mechanism, whether it is attributed to surface impurities or surface roughness, remains uncertain. Addressing this ambiguity represents an intriguing scientific inquiry for further investigations, with significant implications in both our understanding of the fundamental limits of energy loss and our ability to create resonators with better performances.

As it pertains to the applications of our nanomechanical resonators, the possibilities are numerous and yet to be explored. Besides thermometry measurements which we addressed in chapter 5, sensing in general is a natural fit for nanomechanical resonators in view of their ability to couple with the surrounding environment. The extremely low dissipation of our nanomechanical resonators hold the promise to achieve force sensitivity of $aN/\sqrt{Hz}$, paving the way to the development of nanoscale magnetic resonance instru-

6

ments and advanced scanning force microscopes[12]. The achievable acceleration sensitivity is on the order of $\mu g/\sqrt{Hz}$, envisioning the realization of instruments to detect fundamental weak forces, and gravitational fields and to realize next-generation on-chip accelerometers[19]. For all those applications, it will be important to investigate the frequency stability of nanomechanical resonators and their limiting factor[20,21]. High quality factor is predicted to improve the Allan deviation values below 10^{-10}, on par with state-of-the-art clocks[22]. However, the exact limiting factor for frequency stability in nanomechanical resonators remains unclear.

Lastly, the field of optomechanics and quantum technology more generally can surely benefit from the high quality factor of our nanomechanical resonators to release some of the demanding constraints needed to isolate the system from environmental noise. Our resonators are several orders of magnitude above the thermal decoherence limit already at room temperature, making them ideal candidates to observe quantum effects at room temperature[23,24]. To this end, it will be crucial to study the ability to control and measure the resonators in a fast, efficient, and precise manner to avoid thermal decoherence. This is usually achieved by coupling the resonators to an optical or electromechanical cavity. However, this requires an accurate alignment between the resonators and cavity, challenging for our resonators given their aspect ratio. An integrated approach, in which the cavity is fabricated on the same chip is a promising option[25]. Alternatively, a cavity-free approach can be pursued where the resonators are controlled and measured by interferometry[8]. Addressing those questions will have significant impacts on the widespread use of nanomechanical resonators for quantum technology and will contribute to advancing our understanding of quantum mechanics.

References

1. Xu, M., Shin, D., Sberna, P. M., van der Kolk, R., Cupertino, A., Bessa, M. A. & Norte, R. A. High-Strength Amorphous Silicon Carbide for Nanomechanics. *Advanced Materials* **n/a,** 2306513 (2023) (cit. on p. 110).

2. Romero, E., Valenzuela, V. M., Kermany, A. R., Sementilli, L., Iacopi, F. & Bowen, W. P. Engineering the Dissipation of Crystalline Micromechanical Resonators. *Physical Review Applied* **13,** 044007 (2020) (cit. on p. 110).

3. Beccari, A., Visani, D. A., Fedorov, S. A., Bereyhi, M. J., Boureau, V., Engelsen, N. J. & Kippenberg, T. J. Strained crystalline nanomechanical resonators with quality factors above 10 billion. *Nature Physics* **18,** 436–441 (2022) (cit. on p. 110).

4. Li, X., Lekavicius, I. & Wang, H. Diamond Nanomechanical Resonators Protected by a Phononic Band Gap. *Nano Letters* **22,** 10163–10166 (2022) (cit. on p. 110).

5. Manjeshwar, S. K., Ciers, A., Hellman, F., Bläsing, J., Strittmatter, A. & Wieczorek, W. High-Q Trampoline Resonators from Strained Crystalline InGaP for Integrated Free-Space Optomechanics. *Nano Letters* **23,** 5076–5082 (2023) (cit. on p. 110).

6. Bückle, M., Klaß, Y. S., Nägele, F. B., Braive, R. & Weig, E. M. Universal Length Dependence of Tensile Stress in Nanomechanical String Resonators. *Physical Review Applied* **15,** 034063 (2021) (cit. on p. 110).

7. Hälg, D., Gisler, T., Tsaturyan, Y., Catalini, L., Grob, U., Krass, M.-D., Héritier, M., Mattiat, H., Thamm, A.-K., Schirhagl, R., Langman, E. C., Schliesser, A., Degen, C. L. & Eichler, A. Membrane-Based Scanning Force Microscopy. *Physical Review Applied* **15,** L021001 (2021) (cit. on p. 111).

8. Pluchar, C. M., Agrawal, A. R., Schenk, E., Wilson, D. J. & Wilson, D. J. Towards Cavity-Free Ground-State Cooling of an Acoustic-Frequency Silicon Nitride Membrane. *Applied Optics* **59,** G107–G111 (2020) (cit. on pp. 111, 114).

9. Rossi, M., Mason, D., Chen, J., Tsaturyan, Y. & Schliesser, A. Measurement-Based Quantum Control of Mechanical Motion. *Nature* **563,** 53–58 (2018) (cit. on p. 111).

10. Wilson, D. J., Sudhir, V., Piro, N., Schilling, R., Ghadimi, A. & Kippenberg, T. J. Measurement-Based Control of a Mechanical Oscillator at Its Thermal Decoherence Rate. *Nature* **524,** 325–329 (2015) (cit. on p. 111).

11. Manley, J., Chowdhury, M. D., Grin, D., Singh, S. & Wilson, D. J. Searching for Vector Dark Matter with an Optomechanical Accelerometer. *Physical Review Letters* **126,** 61301 (2021) (cit. on p. 112).

12. Eichler, A. Ultra-High-Q Nanomechanical Resonators for Force Sensing. *Materials for Quantum Technology* **2,** 043001 (2022) (cit. on pp. 112, 114).

13. Pratt, J. R., Agrawal, A. R., Condos, C. A., Pluchar, C. M., Schlamminger, S. & Wilson, D. J. Nanoscale Torsional Dissipation Dilution for Quantum Experiments and Precision Measurement. *Physical Review X* **13,** 011018 (2023) (cit. on pp. 112, 113).

14. Høj, D., Wang, F., Gao, W., Hoff, U. B., Sigmund, O. & Andersen, U. L. Ultra-Coherent Nanomechanical Resonators Based on Inverse Design. *Nature Communications* **12,** 5766 (2021) (cit. on p. 113).

15. Høj, D., Hoff, U. B. & Andersen, U. L. Ultra-Coherent Nanomechanical Resonators Based on Density Phononic Crystal Engineering. *arXiv preprint,* arXiv:2207.06703 (2022) (cit. on p. 113).

16. Bereyhi, M. J., Beccari, A., Groth, R., Fedorov, S. A., Arabmoheghi, A., Kippenberg, T. J. & Engelsen, N. J. Hierarchical Tensile Structures with Ultralow Mechanical Dissipation. *Nature Communications* **13,** 3097 (2022) (cit. on p. 113).

17. Bereyhi, M. J., Arabmoheghi, A., Beccari, A., Fedorov, S. A., Huang, G., Kippenberg, T. J. & Engelsen, N. J. Perimeter Modes of Nanomechanical Resonators Exhibit Quality Factors Exceeding 109 at Room Temperature. *Physical Review X* **12,** 21036 (2022) (cit. on p. 113).

18. Villanueva, L. G. & Schmid, S. Evidence of Surface Loss as Ubiquitous Limiting Damping Mechanism in SiN Micro- and Nanomechanical Resonators. *Physical Review Letters* **113,** 227201 (2014) (cit. on p. 113).

19. Chowdhury, M. D., Agrawal, A. R. & Wilson, D. J. Membrane-Based Optomechanical Accelerometry. *Physical Review Applied* **19,** 24011 (2023) (cit. on p. 114).

20. Manzaneque, T., Ghatkesar, M. K., Alijani, F., Xu, M., Norte, R. A. & Steeneken, P. G. Resolution Limits of Resonant Sensors. *Physical Review Applied* **19,** 54074 (2023) (cit. on p. 114).

6

21. Sadeghi, P., Demir, A., Villanueva, L. G., Kahler, H. & Schmid, S. Frequency fluctuations in nanomechanical silicon nitride string resonators. *Physical Review B* **102,** 214106 (2020) (cit. on p. 114).

22. Lewis, L. L. An Introduction to Frequency Standards. *Proceedings of the IEEE* **79,** 927–935 (1991) (cit. on p. 114).

23. Saarinen, S. A., Kralj, N., Langman, E. C., Tsaturyan, Y. & Schliesser, A. Laser cooling a membrane-in-the-middle system close to the quantum ground state from room temperature. *Optica* **10,** 364 (2023) (cit. on p. 114).

24. Serra, E., Borrielli, A., Marin, F., Marino, F., Malossi, N., Morana, B., Piergentili, P., Prodi, G. A., Sarro, L., Vezio, P., Vitali, D. & Bonaldi, M. Silicon-Nitride Nanosensors toward Room Temperature Quantum Optomechanics. *Journal of Applied Physics* **130,** 064503 (2021) (cit. on p. 114).

25. Guo, J., Norte, R. & Gröblacher, S. Feedback Cooling of a Room Temperature Mechanical Oscillator Close to Its Motional Ground State. *Physical Review Letters* **123,** 223602 (2019) (cit. on p. 114).

A

Soft-clamped membranes

This appendix chapter gives an overview of additional 2D nanomechanical resonators developed and fabricated. Besides the nanomechanical resonators presented in the previous chapters, we investigated also 2D geometries for high quality factor applications. All the resonators are designed in Si_3N_4 and fabricated employing the process described in chapter 2.
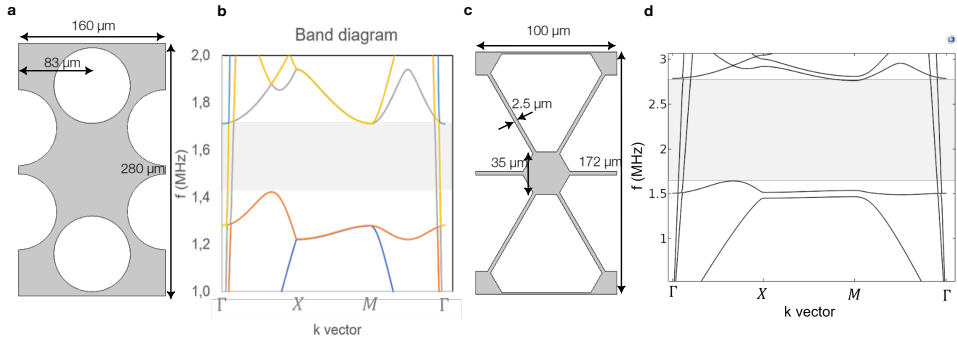
Fig. A.1 a, Unit cell design and **b**, dispersion relation obtained using FEM for 2D hexagonal phononic crystal. **c**, Unit cell design and **d**, dispersion relation obtained using FEM for 2D triangular phononic crystal.

Building on previous works, we designed two different membranes consisting of a phononic crystal with a defect in the center. The unit cell of the phononic crystal of the first design, shown in Fig. A.1a, exhibits a hexagonal periodicity with a pseudo bandgap between 1.4 MHz and 1.7 MHz in Fig. A.1b. The second design has a triangular periodicity, as it can be seen in Fig. A.1c, with a bandgap between 1.6 MHz and 2.7 MHz, shown in Fig. A.1d. The bandgap is computed via finite element analysis with two consecutive studies: a stationary study to extract the stress redistribution followed by a frequency analysis to compute the eigenmodes, both iterated for different values of the wavevector k to obtain the dispersion relation. Fig. A.2a,c shows the resulting stress redistribution.

The maximum feature size of the membrane with triangular phononic crystal is 35 µm. This value is small enough to be suspended by a single SF_6 plasma etching step of 1 minute. On the contrary, the membrane with hexagonal phononic crystal has a maximum feature size exceeding 80 µm. This value would require an SF_6 plasma etching step of more than 2 minutes to be completely suspended, with a significant effect on the Si_3N_4 layer. Moreover, the resulting uneven release of the membrane can lead to stress concentration, exceeding the yield strength of the material. The membrane is therefore patterned with holes of micrometer size to allow a uniform release following the process detailed in chapter 2. Fig. A.1b shows that the added release holes have a negligible effect on the stress redistribution of the unit cell and hence on the bandgap.

We then created the full membrane by periodically combining the unit cells and adding a local irregularity in the center, as can be seen in Fig. A.3a,b. The defect is designed to have an eigenfrequency inside the acoustic bandgap of the surrounding phononic crystal. By doing that, the eigenmode of the defect is spatially confined in the center of the membrane and the bending curvature near the clamping point is strongly suppressed, increasing the mechanical quality factor. The total dimensions of the membrane with a hexagonal periodicity are 3 mm by 3 mm, while the dimensions of the membrane with a triangular periodicity are 1 mm by 1 mm. The thickness for the two designs is respectively 200 nm and 100 nm.

After that, we fabricated the designed membranes on a thin Si_3N_4 layer deposited on
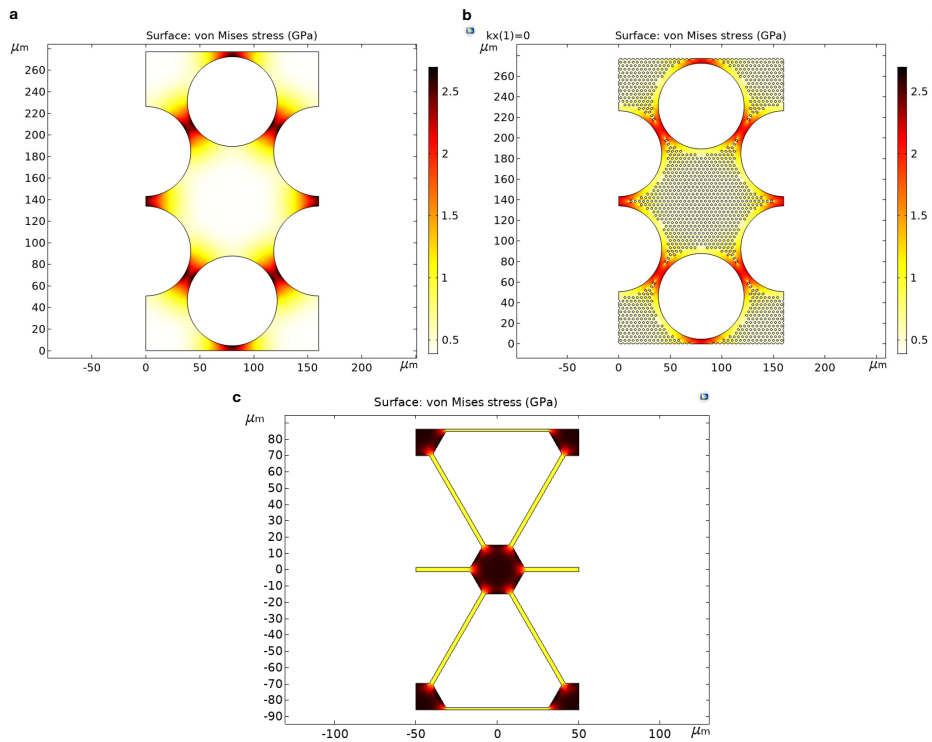
Fig. A.2 a, Stress redistribution of the membrane with the hexagonal phononic crystal before designing release holes and b, after patterning it with holes. c, Stress redistribution of the membrane with triangular phononic crystal.
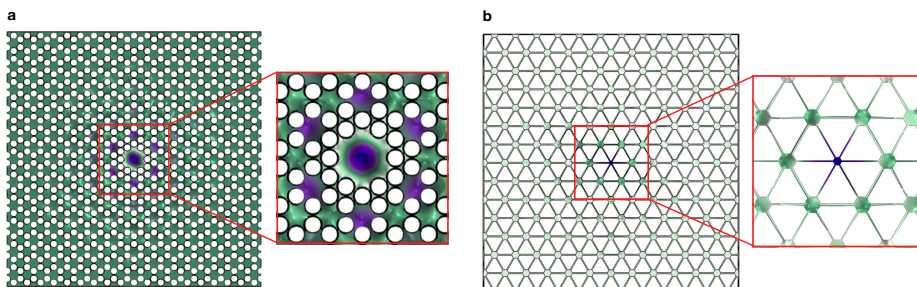

Fig. A.3 a, Mode shape of the first confined mode inside the bandgap at 1.46MHz for the membrane with the hexagonal periodicity and at b, 1.75 MHz for the membrane with triangular periodicity.
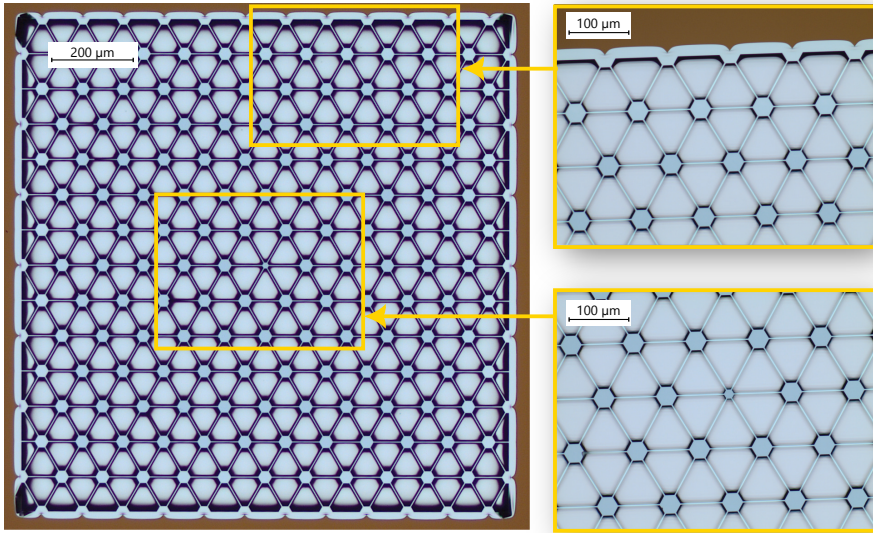
Fig. A.4 Optical microscope picture of the fabricated membrane with triangular periodicity

a silicon substrate. Fig. A.4 shows the suspended membrane with triangular phononic crystal. Here we can notice that sharp angles arise at the edges where the membrane is clamped to the substrate. The angles are created by the isotropic silicon etching and result in noticeable buckling or fracture at the edges. The effect can be prevented by adding holes near those areas to enable a uniform release.

Fig. A.4 shows the suspended membrane with hexagonal phononic crystal. A correct release of the membrane requires a careful design of the position of the release holes. Those need to be placed in an area with low stress to reduce their effect on the stress redistribution inside the unit cell. On the contrary, adding holes in an area with high stress leads to a concentration of the stress in it, highly affecting the overall stress redistribution. For this reason, the final design contains holes only in the pad where the uniform stress is less or equal to 1 GPa. The effect of stress concentration can be observed in Fig. A.6, showing a scanning electron microscope picture of a broken membrane. Here part of the membrane is anchored to the silicon substrate while the remaining is suspended. The anchoring point, shaped as a triangle, is caused by an uneven release of the membrane. A finite element analysis of this case allows to compute the resulting stress caused by the anchored part of the membrane (Fig. A.6), demonstrating that the stress exceeds 6 GPa, a value close to the yield strength of Si_3N_4. We therefore believe the high stress concentration is the main reason for the membrane failure observed.

Finally, we characterized the fabricated resonators with hexagonal phononic crystal with a laser Doppler vibrometer (MSA-400) from Polytec GmbH, by acquiring the velocity of the membrane at different points in a frequency range from 0 MHz to 2 MHz. The
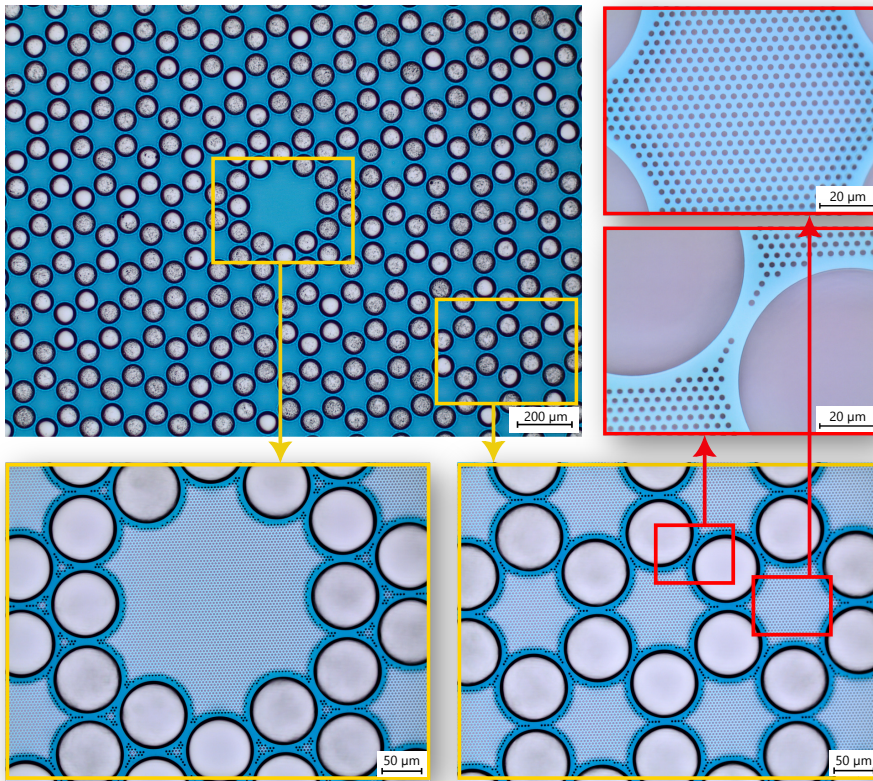
Fig. A.5 Optical microscope picture of the fabricated membrane with hexagonal periodicity
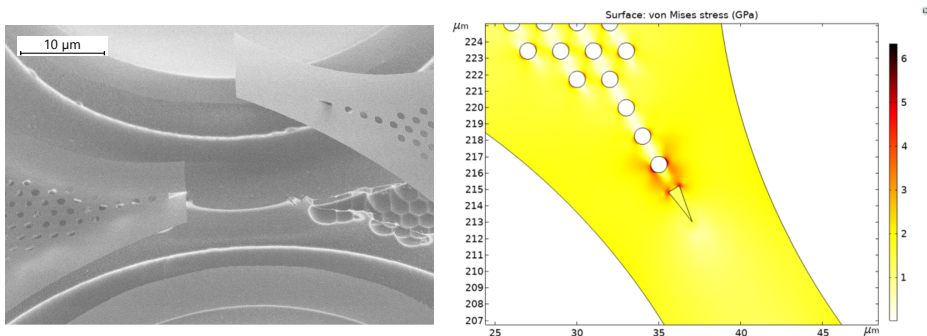

Fig. A.6 Left, Scanning electron microscope picture of a broken membrane. **Right**, Finite element analysis of the stress redistribution when a section of the membrane is anchored to the substrate.
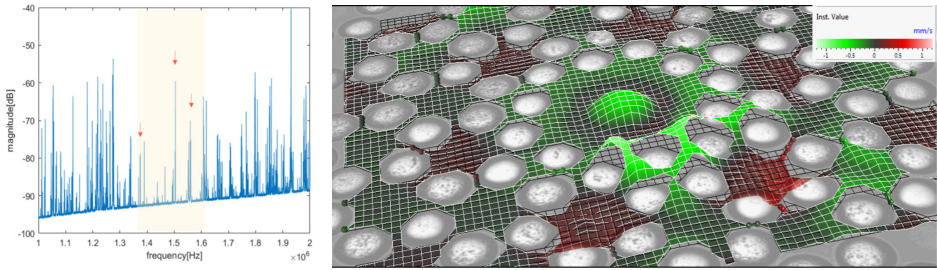
Fig. A.7 Left, Measured spectrum in the central part of the membrane with hexagonal phononic crystal. The yellow area highlights the bandgap and the red arrows the confined modes in it. **Right**, Measured out-of-plane displacement pattern of the first localized mode inside the bandgap.

measurement is performed in vacuum at a pressure of 1×10^{-3} mbar and the resonator is mechanically actuated with a piezoelectric stack. The acquired spectrum of the membrane, in Fig. A.7, shows an acoustic bandgap in good agreement with the simulation from 1.4 MHz to 1.6 MHz. In it 3 confined modes, highlighted with red arrows, are visible. The bandgap contains also additional resonance frequencies coming from the substrate or the measurement setup. Fig. A.7 shows also the extracted mode shape for the first confined mode at 1.38 MHz. The amplitude of it decays outside the defect following the periodic lattice symmetry, as expected due to the presence of the phononic crystal and the forbidden frequency range.

The high pressure level did not allow to correctly estimate the quality factor of the fabricated resonators since gas damping is expected to dominate. For this reason, following the set of data described in this chapter, we decided to build a new interferometer with high vacuum level capability and dedicated equipment for performing ringdown measurements. The latter is the measurement setup employed in chapter 3 and 4 of this dissertation.

To conclude, in this appendix, we developed and fabricated two membrane geometries with phononic crystals. The data presented demonstrate the ability of SF_6 plasma etching to fabricate 2D structures with complex geometries. Nevertheless, the design requires a careful analysis to avoid stress concentration.

B

Process recipes

This appendix chapter presents the process recipes employed to fabricate the resonators described in the main body of this dissertation.

Process recipes for spiderweb nanomechanical resonators of chapter 3.

1	**Wafer Cleaning**

(100) intrinsic Si wafer, thickness 1 mm

RCA1:   **$NH_4OH:H_2O_2:H_2O$ (1:1:5) at** 80 °C **for 10 min**
first pour H_2O into a beaker, then add NH_4OH and heat at 80 °C. Once the temperature is stable pour H_2O_2. After 10 min, rinse in two consecutive H_2O bath for 5 min each

RCA2:   **$HCl:H_2O_2:H_2O$ (1:1:5) at** 80 °C **for 10 min**
same procedure and rinse as RCA1

HF: **HF(0.4%) at RT for 4 min**
rinse with two consecutive H_2O bath of 5 min each

2	**Silicon Nitride deposition** *
LPCVD	**stochiometric Si_3N_4 at** 800 °C

high stress of 1.08 GPa, film thickness 58 nm

3	**Wafer dicing**

wafer coated with optical resist to protect during dicing

Resist coating   S1805 spincoated at 1000 RPM for 1 min. Baked at 90 °C for 5 min

Cleaving   Machine DAD 3220, standard blade, rotation speed 30000 RPM, feed speed 4, size 10 mm × 10 mm

4	**E-beam Lithography**

Rinsing with Acetone and IPA for 10 seconds each to remove the dicing resist, N2 gun

Resist coating   APR-6200-09 (CSAR) spincoated at 3500 RPM for 1 min. Baked at 155 °C for 3 min

Exposure   Machine Raith EBPG-5200, dose 300 $\mu C/m^2$, aperture 200 μm, beam current 2.36 nA, beam size 16 nm, beam step size 5 nm

Dev   Pentylacetate for 60 sec, MIBK:IPA (1:1) rinse for 60 sec, IPA rinse for 60 sec, N2 gun

Optical inspection

---

*Roald van der Kolk, Charles de Boer - Kavli Nanolab, TU Delft

5	Silicon Nitride etching
Etching	CHF_3 60 sccm O_2 6 sccm, ICP power 500 W, RF power 50 W, pressure 1×10^{-4} mbar, temperature 20 °C Etch rate: 80 nm/min, Selectivity to CSAR 1:1 sample clamped to carrier wafer by oil. Remove it afterward with ethanol.
Resist stripping	DMF rinse for 10 sec, DMF rinse for 2 min at RT, Acetone and IPA spray, N2 gun Optical inspection

6	Acid cleaning
Piranha:	**H_2SO_4:H_2O_2 (3:1) at** 80 °C **for 8min** first pour H_2SO_4 into a beaker and heat at 80 °C. Once the temperature is stable pour H_2O_2. After 8 min, rinse in two consecutive H_2O bath for 1 min each. Exothermic reaction, the temperature after pouring H_2O_2 will increase up to 130 °C
HF:	**HF(1%) at RT for 20 sec** rinse with two consecutive H_2O bath of 10 sec and 40 sec Optical inspection

7	Dry release
Etching	SF_6 500 sccm, ICP power 2000 W, RF power 0 W, pressure 10 mbar, temperature −120 °C Etch rate: 10 µm/min, Selectivity to SiN 1:1000 sample clamped to carrier wafer by oil. Remove it afterward with ethanol. Optical inspection

Process recipes for centimeter-scale nanomechanical resonators of chapter 4.

1	**Wafer Cleaning**
	(100) intrinsic Si wafer, thickness 2 mm

RCA1: **$NH_4OH:H_2O_2:H_2O$ (1:1:5) at** 80 °C **for 10 min**
first pour H_2O into a beaker, then add NH_4OH and heat at 80 °C. Once the temperature is stable pour H_2O_2. After 10 min, rinse in two consecutive H_2O bath for 5 min each

RCA2: **$HCl:H_2O_2:H_2O$ (1:1:5) at** 80 °C **for 10 min**
same procedure and rinse as RCA1

HF: **HF(0.4%) at RT for 4 min**
rinse with two consecutive H_2O bath of 5 min each

2	**Silicon Nitride deposition**
LPCVD	**stochiometric Si_3N_4 at** 800 °C high stress of 1.08 GPa, film thickness 100 nm

3	**Wafer dicing**
	wafer coated with optical resist to protect during dicing

Resist coating   S1805 spincoated at 1000 RPM for 1 min. Baked at 90 °C for 5 min

Cleaving   Machine DAD 3220, blade VT07 VC100, rotation speed 10000 RPM, feed speed 4, size 40 mm × 15 mm

4	**E-beam Lithography**
	Rinsing with Acetone and IPA for 10 seconds each to remove the dicing resist, N2 gun

Resist coating   APR-6200-09 (CSAR) spincoated at 3000 RPM for 1 min. Baked at 155 °C for 3 min

Fine exp   Machine Raith EBPG-5200, dose 300 $\mu C/m^2$, aperture 300 μm, beam current 3.99 nA, beam size 18 nm, beam step size 5 nm

Coarse exp   Machine Raith EBPG-5200, dose 300 $\mu C/m^2$, aperture 300 μm, beam current 111 nA, beam size 60 nm, beam step size 50 nm

Dev   Pentylacetate for 60 sec, MIBK:IPA (1:1) rinse for 60 sec, IPA rinse for 60 sec, N2 gun

Optical inspection

5	Silicon Nitride etching
Etching	CHF$_3$ 60 sccm O$_2$ 6 sccm, ICP power 500 W, RF power 50 W, pressure 1×10^{-4} mbar, temperature 20 °C Etch rate: 80 nm/min, Selectivity to CSAR 1:1 sample clamped to carrier wafer by oil. Remove it afterward with ethanol.
Resist stripping	DMF for 15 min at 80 °C in ultrasound bath, Acetone and IPA spray, N2 gun Pour DMF in a baker and heat up at 80 °C. Once the temperature is stable, place the sample inside the baker and transfer it to the ultrasound bath Optical inspection

6	Optical Litography
Resist coating	S1813 spincoated at 4000 RPM for 1 min. Baked at 115 °C for 1 min
Exposure	Laser writer Heidelberg Instruments, dose 220 µC/m^2, defocus -7, focus pneumatic
Dev	MF321 for 120 sec, H$_2$O rinse for 60 sec, N2 gun Optical inspection

7	Silicon deep etching
Etching	SF$_6$ 100 sccm, O$_2$ 21 sccm, ICP power 1000 W, RF power 10 W, pressure 11 mTorr, temperature -120 °C Etch rate: 7.5 um/min, Selectivity to S1813 1:50 sample clamped to carrier wafer by oil. Remove it afterward with ethanol.
Resist stripping	DMSO for 15 min at 80 °C in ultrasound bath, Acetone and IPA spray, N2 gun Pour DMSO in a baker and heat up at 80 °C. Once the temperature is stable, place the sample inside the baker and transfer it to the ultrasound bath Optical inspection

8	Acid cleaning
Piranha:	H_2SO_4:H_2O_2 (3:1) at $80\,°C$ for 8min
	first pour H_2SO_4 into a beaker and heat at $80\,°C$. Once the temperature is stable pour H_2O_2. After 8 min, rinse in two consecutive H_2O bath for 1 min each. Exothermic reaction, the temperature after pouring H_2O_2 will increase up to $130\,°C$
HF:	HF(1%) at RT for 20 sec
	rinse with two consecutive H_2O bath of 10 sec and 40 sec each
	Optical inspection

9	Dry release
Etching	SF_6 500 sccm, ICP power 2000 W, RF power 0 W, pressure 10 mbar, temperature $-120\,°C$
	Etch rate: $10\,\mu m/min$, Selectivity to SiN 1:1000
	sample clamped to carrier wafer by oil. Remove it afterward with ethanol.
	Optical inspection

C

Theoretical derivations

This appendix chapter contains theoretical details concerning how to evaluate and characterize the mechanical resonators developed in the thesis, and how to extract the mechanical dissipation for the structures relevant to this work.

Resonator motion

The one-dimensional displacement of a mechanical resonator is described by

$$z(x,t) = \sum a_n(t)u_n(x) \tag{C.1}$$

where $u_n(x)$ is the one-dimensional mode shape of the nth mode and $a_n(t)$ describes the time evolution of the resonator's motion. For a driven and damped harmonic oscillator, the function $a_n(t)$ is determined by

$$\ddot{a}_n + \Gamma_{m,n}\dot{a}_n + \omega_{m,n}^2 a_n = \frac{F(t)}{m_{\text{eff},n}} \tag{C.2}$$

where $\Gamma_{m,n}$, $\omega_{m,n}$, and $m_{\text{eff},n}$ are the decay rate, the angular frequency, and the effective mass of the resonator for the nth mode. $F(t)$ is the applied time-dependent force.

In a practical setting, we typically use an electronic spectrum analyzer to detect the resonator motion. This instrument does not directly measure the resonator's displacement but the power spectral density of a time-varying signal which has the resonator's motion encapsulated in it. The signal is transformed in the frequency domain, squared, and divided by the resolution bandwidth of the instrument to produce the one-side power spectral density $S_{xx}(\omega)$. In this section we derive the expression for the power spectral density and how this relates to the resonator's displacement.

Power spectral density

The mean-square amplitude $\langle a^2(t) \rangle$ of our signal obtained by averaging over independent experimental runs is given by

$$\langle a^2(t) \rangle = \frac{1}{T_0} \int_0^{T_0} [a(t)]^2 dt \tag{C.3}$$

Since we will focus on a single resonance, we have dropped the subscript n. This quantity is equal to the autocorrelation function R_{xx} at zero time shift, which describes how the signal $a(t')$ is related to itself at a later time $t' + t$

$$R_{xx}(t) = \lim_{T_0 \to \infty} \frac{1}{T_0} \int_0^{T_0} a(t)a(t' + t)dt' \tag{C.4}$$

The autocorrelation function can then be used to define the two-side power spectral density (PSD) $P_{xx}(\omega)$ as its Fourier transform function

$$P_{xx}(\omega) = \int_{-\infty}^{\infty} R_{xx}(t)e^{i\omega t} dt \tag{C.5}$$

Similarly, the autocorrelation function is given by

$$R_{xx}(\omega) = \frac{1}{2\pi} \int_{-\infty}^{\infty} P_{xx}(\omega)e^{i\omega t} d\omega \tag{C.6}$$

Using the expression in equation C.6 with the equality between mean-square amplitude (equation C.3) and autocorrelation function (equation C.4) we can then express $\langle a^2(t) \rangle$ as function of its PSD

$$\langle a^2(t) \rangle = \frac{1}{2\pi} \int_{-\infty}^{\infty} P_{xx}(\omega) e^{i\omega t} d\omega \tag{C.7}$$

This PSD is defined over the entire frequency range. However, in experiments, the measured signal extends only over positive frequencies. We can therefore introduce a one-side power spectral density S_{zz} which extends from 0 to ∞ such that $S_{zz} = 2P_{zz}$. Equation C.7 then takes the form

$$\langle a^2(t) \rangle = \frac{1}{2\pi} \int_{0}^{\infty} S_{xx}(\omega) e^{i\omega t} d\omega \tag{C.8}$$

This expression gives us the relationship between the PSD and the mean-square amplitude.

We can then proceed to calculate the equation of motion in the frequency domain. By Fourier transforming equation C.2 we can express it in the form $a_n(\omega) = \chi(\omega) F(\omega)$ where $F(\omega)$ is the applied force, while $\chi(\omega)$ is the susceptibility

$$\chi(\omega) = \frac{1}{m_{\text{eff}}} \frac{1}{\omega_m^2 - \omega^2 - i\omega\Gamma_m} \tag{C.9}$$

If we Fourier transform the mean-square amplitude (equation C.8) we consequently relate its PSD S_{xx} to the PSD of the applied force S_{FF}

$$S_{xx}(\omega) = |\chi(\omega)|^2 S_{FF}. \tag{C.10}$$

At thermal equilibrium, S_{FF} is related to the mechanical susceptibility $|\chi(\omega)|$ by the fluctuation-dissipation theorem

$$S_{FF} = -\frac{4k_B T}{\omega} \operatorname{Im} \frac{1}{\chi(\omega)} = 4k_B T \frac{m_{\text{eff}} \omega_m}{Q_m} \tag{C.11}$$

where Q_m is the quality factor of the resonator

If we then combine equations C.11 and C.9 with equation C.10 we obtain the one-side PSD

$$S_{xx}(\omega) = \frac{4k_B T \omega_m}{m_{\text{eff}} Q_m \left[\left(\omega_m^2 - \omega^2 \right)^2 + \left(\frac{\omega \omega_m}{Q_m} \right)^2 \right]} \tag{C.12}$$

In case of high-Q oscillators near resonance, the one-side PSD can be approximated by a Lorentzian:

$$\omega \approx \omega_m \quad \Rightarrow \quad \omega_m^2 - \omega^2 = (\omega_m - \omega)(\omega_m + \omega) \approx (\omega_m - \omega) 2\omega_m$$

$$S_{xx}(\omega) = \frac{4k_B T \frac{\omega_m}{Q}}{m_{\text{eff}} \omega_m^2 \left[\left(\omega_m - \omega \right)^2 + \left(\frac{\omega_m}{Q_m} \right)^2 \right]} \tag{C.13}$$

This gives us the theoretical displacement PSD in unit m^2/Hz due to thermomechanical noise. However the measured PSD by a spectrum analyzer $S_{vv}(\omega)$ contains additional sources of noise caused by our detection system and, generally, has a unit of V^2/Hz. If we assume that the additional sources of noise are white, the measured voltage PSD is related to the theoretical displacement PSD by the following relationship

$$S_{vv}(\omega) = \alpha S_{xx}(\omega) + S_{vv}^{\text{noise}}(\omega) \tag{C.14}$$

where α is a conversion factor from m^2/Hz to V^2/Hz and $S_{vv}^{\text{noise}}(\omega)$ is a constant offset to account for the detection noise.

Quality factor and ringdown

The quality factor of a resonator is defined as the ratio of the energy stored over the energy dissipated per each cycle

$$Q_m = 2\pi \frac{E_{\text{stored}}}{\Delta E_{\text{dissipated}}} \tag{C.15}$$

Likewise, it can be defined as the ratio between the angular frequency and the decay rate of the resonator

$$Q_m = \frac{\omega_m}{\Gamma_m} \tag{C.16}$$

To extract the quality factor one can then fit the measured spectrum with equation C.12. However, if the linewidth of the resonator becomes comparable to or smaller than the resolution bandwidth of the instrument, resolving the spectral peak with sufficient resolution becomes difficult. To correctly resolve the narrow peak one would have to average the signal for a long time or increase the acquisition time to obtain enough data points. However, both methods are prone to artificial broadening of the acquired peak due to the drift of the resonance frequency within the acquisition time.

In this situation measuring the energy dissipated per each cycle via a ringdown technique is a more straightforward method to estimate the quality factor. The resonator is driven at its resonance frequency by an external excitation until it reaches a steady state. The excitation is then turned off and the quality factor is extracted by measuring the time it takes for the resonator to naturally decay. To do so, we can express the time evolution of the energy of the oscillator during a ringdown measurement with the following

$$W(t) = W(t_0)e^{-\Gamma_m(t-t_0)} + W_0 \tag{C.17}$$

where $W(t_0)$ is the energy at time $t = t_0$ when the resonant driving force is stopped and W_0 is a constant offset to take into account the noise floor. Measuring the decay rate Γ_m and the angular frequency ω_m gives then access to the quality factor of the resonator by equation C.16.

In practice, when dealing with mechanical resonators with high quality factor (e.g. Q >10^8) is difficult to reach steady state while driving the resonator because the fluctuations of the resonance frequency are larger than its linewidth ($\Delta\omega_{RMS} > \Gamma_m$). As a result, we first acquire the spectrum of the resonator driven only by Brownian motions to estimate its resonance frequency. The spectrum is recorded by employing a small resolution bandwidth

on the spectrum analyzer (e.g. 1 Hz). Secondly, we sweep the drive frequency around the resonance frequency of the mechanical resonator with steps of mHz while recording the spectrum with a larger resolution bandwidth on the spectrum analyzer (e.g. 10 Hz) to decrease the acquisition time. We usually observe a beating effect due to the difference between the drive frequency and the resonance frequency of the mechanical resonator, which decreases when the two frequencies get closer. For a short amount of time, the drive frequency will be on-resonance with the mechanical resonator and the beating effect will disappear. At this moment we stop the excitation, and we record consecutive spectra during the free oscillation of the resonator.

For every spectrum, we extract the peak value corresponding to the value of the power spectral density at the resonance frequency

$$P_{dBm}(t)|_{\omega=\omega_m} = 10 \log_{10} \frac{P(t)|_{\omega=\omega_m}}{1mW} \tag{C.18}$$

where $P(t)$ is the measured power in Watt while $P_{dBm}(t)$ is the value in dBm. Following equation C.17, the measured power decays exponentially following $P(t) = P(0)e^{-\Gamma_m(t)} + P_0$. Note that we considered $t_0 = 0$. In log scale the decay becomes linear following $P_{dBm}(t) = At + P_0$.

If we acquire our signal in dBm, we can perform a linear fitting to obtain the value of A, then extract the decay rate Γ_m by applying the relationship in equation C.18:

$$-At = 10 \log_{10} e^{-\Gamma_m t} \tag{C.19}$$

$$10^{(-At/10)} = e^{-\Gamma_m t} \tag{C.20}$$

$$-\frac{At}{10} \ln(10) = -\Gamma_m t \tag{C.21}$$

The quality factor can then be calculated by dividing the resonance frequency with the obtained decay rate (equation C.16).

Note that equation C.17 is derived for the energy of the resonator which is proportional to $a(t)^2$. On the contrary, the amplitude of the resonator is proportional to $a(t)$. As a result, if one acquires the power spectral density measured in Voltage instead of Watt, the amplitude decays with a rate equal to $\Gamma_m/2$. This should be carefully taken into account during the fitting process to obtain the correct damping rate based on the acquired data.

D

Ultra High Vacuum Setup

To characterize the mechanical resonators presented in this thesis, we have built a dedicated characterization setup that optically reads out the devices' displacement. This working principle of this setup has been described in chapters 3 and 4. This chapter provides additional details, specifically concerning the vacuum requirements.
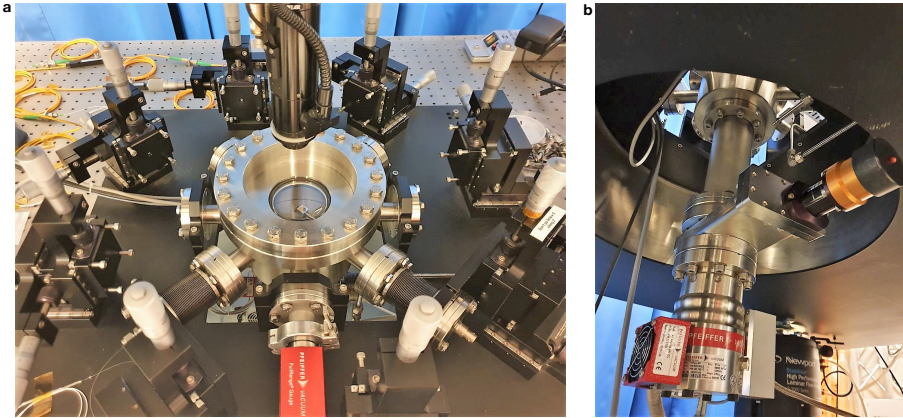
Fig. D.1 Vacuum chamber and turbo molecular pump. **a**, a photograph of the vacuum chamber with the objective lens of the optical microscope mounted above. **b**, a photograph of the turbo molecular pump connected to the bottom of the vacuum chamber in **a** via a valve.

Ultra high vacuum chamber

To suppress gas damping, the mechanical resonators need to operate at low pressure. For devices possessing high quality factor (e.g. $Q>10^8$), the pressure needs to be lower than 10^{-8} mbar, in the so-called "ultra-high vacuum (UHV)" regime. See also Supplementary Information of chapter 4 for additional details about gas damping. To this end, we designed and built a UHV setup able to operate at a pressure level equal to 10^{-9} mbar. The setup is equipped with optical access to detect the motion of the resonators, mechanical excitation to drive the devices, and a nanopositioner for alignment purposes.

The vacuum setup consists of a cylindrical chamber (Fig. D.1a) with 8 CF-40 flanges along the lateral surface and 2 CF-100 flanges on the top and the bottom. CF stands for ConFlat, a type of flange compatible with pressure down to 10^{-13} mbar which employs a ring-shaped metal gasket (usually copper). The top flange of the chamber is closed with a glass view-port to inspect the chips via an optical microscope mounted on top (Fig. D.1a), while the bottom flange is connected to a turbo molecular pump via a valve. The 8 CF-40 flanges are employed for electrical and optical connection and the vacuum gauge. The chamber is mounted on top of an optical table to suppress mechanical vibrations. The table has a hole in the center, such that the turbo molecular pump can be directly connected to the bottom of the chamber. This allows to reduce the volume and the surface of the overall vacuum system improving the pumping efficiency. (Fig. D.1b).

The chamber is equipped with a UHV compatible triaxial nanopositioner placed inside and connected to one of the 8 CF-40 flanges via an M12 feedthrough (Fig. D.2b). The mechanical resonators are then mounted on top of the nanopositioner using a custom-made * aluminum holder (Fig. D.2b). The chip holder is clamped to the nanopositioner by a curved thin strip of aluminum which acts as a spring. This clamping method enables us

---

*Gideon Emmaneel - Precision and Microsystems Engineering Department, TU Delft
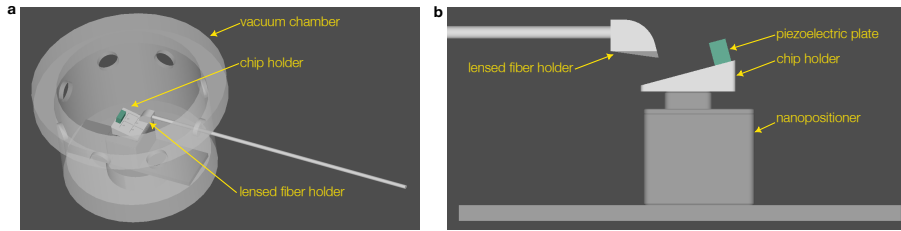
Fig. D.2 UHV compatible chip holder and lensed fiber holder. **a**, 3D rendering of the vacuum chamber with vacuum components inside. **b**, 3D rendering of the xyz nanopositioner with the custom-made chip holder mounted on top and the piezoelectric plate (the thickness of the piezoelectric plate in the rendering is increased compared to the real dimensions for visualization purposes). The lensed fiber is mounted on a holder placed at a 90 degree angle with respect to the device.

to easily change the holder based on the chip we are measuring.

A piezoelectric plate is connected through two screws to the upper face of the holder to actuate the devices mechanically. The material plate is PIC 255 from PI ceramic with dimensions $10 \times 10 \times 0.5$ mm, resulting in an expected resonance frequency of 4MHz. UHV compatible KAPTON wires are then soldered to the CuNi electrodes with lead-free solder wire [†]. The wires are connected to a BNC feedthrough mounted on one of the 8 CF-40 flanges on the chamber.

The displacement of the resonators is detected by an infrared interferometer. To this end, we placed a lensed fiber inside the vacuum chamber at a 90 degree angle with respect to the device. The lensed fiber is mounted on a rod connected to a 3-axis manual stage placed outside the chamber via a feedthrough (Fig. D.2a). The stage allows us to independently control the position of the fiber and align the devices to its focal plane. The signal coming out from the lensed fiber can then couple to the out-of-plane displacement of the resonators before being collected back. The lensed fiber is coupled in and out of the cavity using a costume-made Teflon piece which is sealed by a CF-compression fitting adapter. The employed lensed fiber has a spot size of 2.5 μm and a focal distance of 15 μm, compatible with the small dimensions of our resonators discussed in this thesis.

The lensed fiber and the chip holder are titled at the same angle with respect to the optical microscope mounted outside the chamber. This allows us to observe at the same time the lensed fiber and the device for alignment purposes.

Assembling and loading

Before assembly, we cleaned all the custom-made components in two consecutive ultrasonic baths of 5 minutes each with acetone and isopropanol, before being dried with a nitrogen gun. To avoid any organic contamination such as fingerprints, we always handled the components with clean nitrile gloves. At the same time, we used new copper gaskets every time a flange needed to be opened. The setup was equally checked with a helium leak tester every time a new component was placed inside the chamber.

[†]Spiridon van Veldhoven - Precision and Microsystems Engineering Department, TU Delft

The devices are loaded from the view-port on the top of the chamber. During the loading phase, the view-port is placed on top of a clean aluminum foil to avoid any contamination. The chip holder is then removed from the chamber and placed on top of an aluminum foil. Once the devices are mounted on top of it, the chip holder is placed back inside the vacuum chamber on top of the nanopositioner. The chamber is subsequently closed using a new copper gasket to seal the CH-100 view-port. The backing pump is then turned off, which usually allows to reduce the pressure down to 1 mbar. After that, we usually purge the chamber with nitrogen 3 consecutive times, for around 30 seconds each, before turning on the turbo molecular pump. The vacuum system can typically reach a pressure of 1×10^{-8} mbar after one day of pumping, while 1×10^{-9} mbar requires one full week after the turbo molecular pump is turned on.

Acknowledgment

Modern science is a collective effort. As such it feels odd that a PhD thesis needs to be individual, at least for a PhD student whose path in research just started. Defining the personal contributions to each study here presented has hence been a difficult task, especially for an everlasting hesitating person. I truly believe that the results presented in this thesis would not have been possible without the support of many people. Therefore, here comes the, for some most interesting and I suspect most read, part of this thesis.

The first person on the list is my co-promoter, Richard. I distinctly recall our initial encounter in Delft, nearly five years ago. Your enthusiasm and excitement for the project swiftly convinced me to embark on a PhD journey within your group. Being one of the first members of the group presented both unique challenges and opportunities, and I am thankful for the chance to learn directly from you during our countless discussions, cleanroom sessions, and shared moments in the lab. You have been a constant source of ideas to the extent that, at times, I even found myself inundated by them. You taught me the importance of communicating the results in accessible and clear terms and the importance of collaborations. Working alongside you has been a privilege, and I am grateful for your positivity and determination.

Next, my promotor. Peter, your passion for research, curiosity, and profound knowledge have left an indelible mark. Over the years, you have been an indispensable pillar of support, consistently available for stimulating scientific discussions and, more significantly, displaying a genuine concern for my well-being and the advancement of my PhD. Your mentorship has been crucial in refining my approach to projects, encouraging me to approach them from various angles and equipping me with the skills to achieve desired results. During our interactions, your insightful comments consistently challenged my understanding, pushing me to explore different perspectives. I am truly grateful for your guidance and support.

I wish to extend my gratitude to the experts who agreed to be the committee members of my PhD defense, offering their stimulating feedback. Miguel, thanks for all the extensive interactions we have had throughout these years. It has been a privilege to know you as both a supervisor and a teacher, and I continue to be amazed by your talents in both. Your logical thinking and experience have been invaluable resources to the successful completion of the collaborative project. Urs, your contributions and expertise in vacuum technology have greatly enriched my research journey over the years. Silvan, I am grateful for the guidance I have found in your publications and books, which have significantly enhanced my understanding of high Q resonators and nanomechanics, as well as your talks during the conferences. Alexander, your groundbreaking work on sensing using nanomechanical resonators has been truly inspiring. Ewold, I appreciate your stimulating research contributions, which have played a vital role in shaping my own academic journey. Finally, Gary, thanks for your sharp questions during the QN weekly meetings, which consistently pushed me to reevaluate my results and expand my knowledge.

Special thanks go to Minxing and Satadal who will be accompanying me as paranymphs during the PhD defense. Minxing, my cleanroom buddy and companion in the lab and the office, your presence in the group has made my journey much more fun. There is always something new to learn from you, whether it is about a new paper that just came out, the secrets of crypto or the future of AI. I truly enjoyed all our shared moments, from the countless hours in the cleanroom and lab to our coffee breaks, dinners, and padel matches. You have become a true guru of nanofabrication, and your dedication to research is evident in the exciting results you have achieved. I wish you the very best in wrapping up your PhD and look forward to the many more exciting results yet to come. Satadal, we both joined the DMN group simultaneously and have been office mates ever since. Your broad knowledge spanning from chemistry to physics, and from politics to geography, has consistently enlightened and enriched our discussions. Not to mention, your sense of humor and nerdy jokes always add a delightful touch. I also greatly enjoyed our time together as a team padel. Your willingness to share your postdoc perspective has been invaluable, and I wish you the best of luck in your future endeavors.

Being a part of NorteLab has truly been an enriching experience. My PhD journey would not have been the same without the support of everybody and I am grateful to all past and current members. Dongil, you have probably been the team member who, more than everybody else, had an impact on my research. Our fruitful collaboration started as a side project and swiftly evolved into the central focus of my research, whose results have shaped this PhD thesis. I deeply enjoyed your kindness and your motivation, especially when the results were far from being what we expected with little understanding of the reasons. Through our work together, I could truly appreciate the beauty of teamwork and its significance. Beyond being a team member, I found in you a good friend with whom I could enjoy walks and meaningful conversations, and discover Korean cuisine. You are a very talented and dedicated researcher with many more accomplishments ahead. Matthijs, thanks for always being available to answer my questions and for teaching me how to build and operate optical setups. More importantly, thanks for showing me how to be a methodic and organized experimentalist and being the social soul of the group. I greatly enjoyed our projects together as well as the time in the UK during the CMD conference. Your genuine kindness and readiness to assist fellow PhD candidates and students exemplify your character, and I am confident that you will achieve great success in your research pursuits. Stefanos, your arrival in the group coincided with my work on the optical setup, and your expertise in optics and extensive experience were invaluable in overcoming the myriad challenges I encountered. Your curiosity and depth of knowledge also helped me to think critically about my project. Thanks for it and for our never-obvious lunchtime discussions. Yufan, thanks for all your ideas and feedback during the group meeting. Witnessing your gradual progress in fabricating diamond nanobeams and a scanning magnetometer, along with the challenges you surmounted, has been nothing short of fascinating. Lucas, thanks for bringing to the group a fresh wave of enthusiasm, for engaging in stimulating discussions, and for always being up for beers. Ata, you were the first person I met during my first visit at TU Delft, while applying for the PhD position. You always have smart questions during the DMN meeting and your genuine passion for research has been a source of inspiration during the past years. Best of luck with your own defense. Megha, thanks for your kindness. Looking forward to exciting results on the

DBR. Paulina, I am delighted that you have joined the PhD Council, and I am confident you will both enjoy and make significant contributions to it. Thanks for your positive energy and your expansiveness. Finally, I would like to express my gratitude to all the students in the group for creating a nice and collaborative environment, especially to Tray and Fenghuan. Your curiosity and questions constantly challenged my knowledge, and your diligent work has not gone unnoticed.

Beyond the Nortelab group, many more people in the DMN group and the PME department had a major impact on the work presented in this thesis. Being immersed in such a collaborative and supportive environment has proven to be tremendously helpful for my research as well as made my PhD experience fun and memorable. Tomas, your brilliance as a researcher is only matched by your kindness and willingness to assist and support your colleagues within the group. Thanks for it and for all the Padel matches played together. I wish you all the success in your rising career in academia. Abilash, joining the PhD Council has been a delightful and enriching experience, and I'm grateful to you for introducing me and your invaluable suggestions as the senior PhD in the group. Xiangfeng, thanks for all the discussion about high Q resonators and vacuum setup, and for always being so positive. Irek, the entrepreneurial spirit of the department. You accomplished so much within your PhD, I wish you the best on your journey ahead. Curry, your tireless work ethic is truly admirable, and, despite it, you are always smiley and a source of optimism. Good luck with your future endeavors. Martin Robin, thanks for the enjoyable times spent together in the lab learning about your setup. Ruben, your enthusiasm for your research and constant flow of ideas have been a great source of inspiration. Frederike, thanks for your curiosity and the insightful discussion. Thanks to both of you for organizing the much-needed research coffee. I hope it continues to foster collaborations and mutual knowledge-sharing within our department. Pieter, thanks for all the laughs and the energy you put into the department. Inge, thanks for our insightful conversation and your kindness. Breno, your laugh, jokes, and boundless energy (despite the Dutch weather making you constantly sick) have been a welcome presence during your stay in the Netherlands. Zhichao, we began our PhD journeys around the same time, and our encounters in the corridor always led to unexpected and enjoyable conversations that left me with a smile. Roberto, thanks for your spontaneity and your cheerfulness. It was fascinating to hear about your projects and all the fabrication challenges you managed to solve whenever we crossed paths in the lab. Tufan, sharing the lab and witnessing your progress has been a great experience. Thank you for all the help and interest in my research. Ali, amidst the uncertainties of my PhD journey, one constant source of certainty was knowing that you would be present in the office every day, making our coffee breaks and discussions consistently enjoyable. Zichao, thanks for all the nice discussion about high Q resonators, piezos, and vacuum which helped improving my understanding. The second sure thing was that Sabiju would invariably interrupt the day with his questions while his simulation was in progress. Sabiju, I'm truly grateful for our discussions and for your willingness to share your expertise on phononic crystals, your presence has been dearly missed in the office since you left. Nils, your kindness and cheerfulness have been a bright spot in the office. To Saleh, Inge, Xiliang, Yuheng, Gúrhan, Simona thanks for creating a pleasant office environment and engaging in enriching discussions. To Francesco, Ali, Stijn, Malte, Dong Hoon, Pieter, Giuseppe, Hava, Giulio, Sifeng, Ad, Pierre, Ahmed,

Maarten, and many more, I am grateful for our shared lunch and the nice interactions. Finally, thanks to all the PIs in the department, especially Farbod, Gerard, Wouter, Sabina, Murali, Ivan, and Angelo, for your assistance, interest in my research, and the enlightening discussions.

I would also like to express my gratitude to everybody in QN, for all the inspiring talks during the weekly meetings, the acute and sharp questions, and the enjoyable moments we have shared. Martin, your scientific curiosity, and unwavering work ethic have set a remarkable example and served as a constant motivation throughout my PhD journey. Despite your countless projects, you always managed to find time to lend your expertise, particularly in the cleanroom. I owe a significant portion of my cleanroom knowledge to your guidance, and I am truly thankful. Makars, your deep understanding, and passion for research have equally amazed me. Thanks for your help in the lab, especially in the Montana lab. The bar you and Martin have set is incredibly high, making it a genuine challenge to uphold the research standards you have established within the group. Gabriele, thanks for brightening our interactions with your ever-present smile and your support. Maurits, thanks for the insightful discussions and all the energy you dedicate to the department. Niccoló, our conversations about relationships were truly enjoyable and enlightening. Thanks for your enthusiasm and for bringing joy to the department. Nina, it was a pleasure to share the experience of being paranymphs with you. Thanks for your tips in the cleanroom and all the nice conversation. Jingkun, your assistance in the cleanroom and your willingness to share your expertise with me have been invaluable. To Parsa, Bas, Rob, Sonakshi, Ulderico, Luigi, Brecht, thanks for all our interactions during the past years. Finally, I am grateful to the PIs within the department, especially Simon, for your support during my first year and for granting me access to your lab, and to Sonia, for your positivity and boundless energy.

I also don't want to forget all the members of the 3mE PhD Council. Their presence has been instrumental in shaping my PhD journey and it helped me to better understand what doing a PhD in our faculty implies, what are the challenges, and how to face them. Being surrounded by brilliant and motivated people was an enriching and fun experience. I felt really privileged to be part of this group and enjoyed all the lunch, the discussion sessions, and the activities organized over the past years. A heartfelt gratitude to each member: Alina, José, Ankur, Hugo, Vishal, Athina, Eline, Hongpeng, Abhilash, Bart, Padmaja, Robin, Yujie, Sietske, Suriya, Vasu, Martin, Jette, Kirsten, and Costanza. Mascha, thanks for the trust and the encouragement you put in the PhD Council, and for all the long and nice discussions. Paul, thanks for your honest and to-the-point opinions as well as your active involvement and commitment to the PhD community.

Special thanks must go to all the dedicated support staff in both PME and QN for making sure that everything works smoothly, allowing us to focus on our research endeavors. Patrick, Gideon, Alex, Spiridon, and Bradley, thanks for the countless discussions and constant support you have provided in the pursuit of building and enhancing the optical setup. Rob, thanks for keeping everything well organized and for your expert suggestions. Marli and Lisette, thanks for your invaluable assistance with orders and solving any issues that arose along the way. Maria, during the initial year of my PhD, your support on all matters related to QN was greatly appreciated. Your kindness and openness during our discussions significantly contributed to fostering an enjoyable departmental environment.

I would also like to acknowledge the entire staff at Kavli Nanolab for their meticulous organization of the cleanroom and their responsiveness to our requests and concerns. Roald, thanks for your genuine interest in research and for all the support with deposition and etching. Lodi, thanks for all your help, especially for training during the covid pandemic, and for always being open to listening. Charles, Marc, Bas, Anja, Hozanna, Eugene, and Arnold, thanks for all your suggestions and your assistance in refining my fabrication processes, which has been instrumental in advancing my research.

Besides all the people at the university, my journey in Delft would have been a completely different adventure without many more people who added excitement to my experience and helped alleviate stress. Thanks, Livio, for your precious perspective, generosity, and helpfulness, and the seemingly non-sense but impossible-to-stop-watching YouTube videos, Francesca, for being so joyful and full of energy, Abdu, for the engaging discussions, your infectious smile, and your delicious cuisine, Mariya and Thijs, for the nice moments we have shared, Asala, for your unwavering determination and kindness, "my friend" Teni, for your positive vibes and contagious laughter, Joe and Ruba, for showing me the beauty of Lebanon and Ghent and all the delicious food, Alejandra for your boundless energy and enthusiasm, Svenja, for our engaging discussion and your kindness, Cristian, for your cheerfulness, Puk, for your overexcitement every time we meet and for no longer barking at me. Thanks, Luis and Maria, for the memorable board game nights and the nice moments together, David, for the delicious dinners at your place and your cheerfulness, Juan, Thomas, Sonja, and Luisa, for the trip together and the lasting memories. José, Leila and Pablo, thanks for introducing me to the world of open source and your contagious energy. Matteo, Serena, and Lucy thanks for all the fun with Padel and for making me discover the best pizza place in Delft.

Throughout the years, my journey has led me to cross paths with many former colleagues and friends in Puglia, Belfort, Torino, Grenoble, Berlin, Lausanne, and California before moving to Delft. I would like to take a moment to acknowledge all of them, as these encounters have significantly enriched my life. With some have them we are good friends. To each of you, thanks for all the wonderful moments we've experienced together and for keeping my spirits high. Your friendship means a lot to me. Among them, a special thanks goes to Giancarlo for all the help with creating the cover page of this dissertation. With some of them, we may have lost contact, but our encounters have left an indelible mark and have played a crucial role in shaping the person and researcher I have become today. I am equally grateful to all of you for the impact you've had on my life.

Lastly, I want to express my deepest gratitude to my family, given and taken. Their belief in me and continuous and unconditional support have been a constant source of strength. Whenever things didn't go as planned, when seemingly insurmountable challenges appeared on the horizon, or when I simply needed someone to share good news with, I knew I could always count on them. Among them, a special acknowledgment to the person whose support has been the most valuable and significant, without whom I may not have embarked on this PhD journey in the first place. Thanks, Anna, for your patience, your unwavering encouragement, and your ever-present smile.

Curriculum Vitæ

Andrea CUPERTINO

08-06-1992   Born in Putignano, Italy.

Education

2019–2023   PhD in Precision and Microsystems Engineering
             Delft University of Technology, the Netherlands
             Thesis: Exploring the quality factor limits of room tempera-
                            ture nanomechanical resonators
             Promotor: Prof. dr. P. G. Steeneken
             Co-Promotor: Dr. R. A. Norte

2018   Visiting Student Researcher
             Stanford University, California

2016–2018   Joint Master of Science in Nanotechnologies for ICTs
             École Polytechnique Fédérale de Lausanne, Switzerland
             Grenoble INP - Phelma, France
             Politecnico di Torino, Italy

2011–2015   Bachelor of Science in Electronics Engineering
             Politecnico di Bari, Italy

List of Publications

- **Cupertino A.***, Shin D.*, Guo L., Steeneken P. G., Bessa M. A., Norte R. A., *Centimeter-scale nanomechanical resonators with low dissipation*, manuscript under review, preprint: arXiv:2308.00611 **(2023)** (*contributed equally to this study).

- Xu M., Shin D., Sberna P. M., van der Kolk R., **Cupertino A.**, Bessa M. A., Norte R. A., *High-Strength Amorphous Silicon Carbide for Nanomechanics*, Advanced Materials, 2306513 **(2023)**

- de Jong M. H. J., Ganesan A., **Cupertino A.**, Gröblacher S., Norte R. A., *Mechanical overtone frequency combs,* Nature Communications 14, 1458 **(2023)**

- de Jong M. H. J., **Cupertino A.**, Shin D., Gröblacher S., Farbod A., Steeneken P. G., Norte R. A., *Beating Ringdowns of Near-Degenerate Mechanical Resonances,* Phys. Rev. Applied 20, 024053 **(2023)**.

- Shin D.*, **Cupertino A.***, de Jong M. H. J., Steeneken P. G., Bessa M. A., Norte R. A., *Spider-web Nanomechanical Resonators via Bayesian Optimization: Inspired by Nature and Guided by Machine Learning*, Advanced Materials, 34(3), 2106248 **(2022)** (*contributed equally to this study).

- de Jong M. H. J., Wolde M. A., **Cupertino A.**, Gröblacher S., Steeneken P. G., Norte R. A., *Mechanical dissipation by substrate-mode coupling in SiN resonators,* Appl. Phys. Lett. 121, 032201 **(2022)**.

- Briant T., Krenek S., **Cupertino, A.**, Loubar F., Braive R., Weituchat L., Ramos D., Martin Hernandez M. J., Postigo P. A. , Casas A. , Eisermann R., Schmid D., Tabandeh S., Hahtela O., Pourjamal S., Kozlova O., Kroker S., Dickmann W., Zimmermann L., Winzer G., Martel T., Steeneken P. G., Norte R. A., and Briaudeau S., *Photonic and Optomechanical Thermometry*, Optics, 3(2), 159-176 **(2022)**